



SAPIENZA
UNIVERSITÀ DI ROMA

Investigating backgrounds to Dark Higgs searches at PADME

Facoltà di Scienze Matematiche, Fisiche e Naturali

Corso di Laurea Magistrale in Particle and Astroparticle Physics

Candidate

Gabriele Martelli

ID number 1647148

Thesis Advisor

Prof. Mauro Raggi

Co-Advisor

Dr. Gabriele Piperno

Academic Year 2018/2019

Thesis defended on 24/01/2020
in front of a Board of Examiners composed by:
Prof. Antonio Capone (chairman)
Prof. Valerio Parisi
Prof. Cesare Bini
Prof. Paola Leaci
Prof. Marco Nardecchia
Prof. Roberto Maoli
Prof. Fabio Anulli

Investigating backgrounds to Dark Higgs searches at PADME
Master thesis. Sapienza – University of Rome

© 2019 Gabriele Martelli. All rights reserved

This thesis has been typeset by L^AT_EX and the Sapthesis class.

Author's email: gabriele.martelli@lnf.infn.it

PADME



Acknowledgments

Firstly, I would like to express my sincere gratitude to my advisor Prof. Mauro Raggi for the continuous support of my thesis work, for his patience, and motivation. His guidance helped me in all the time of work and writing of this thesis. I could not have imagined having a better advisor and mentor for my university study.

Besides my advisor, I would like to thank my co-advisor Dr. Gabriele Piperno and Dr. Emanuele Leonardi from the PADME collaboration for their insightful comments and encouragement, but also for the hard question which stimulated me to extend my work from various perspectives.

Last but not the least, I would like to thank my family and my friends for supporting me spiritually throughout writing this thesis and my life in general.

Contents

Introduction	ix
1 The Dark Matter problem	1
1.1 Standard Cosmological Model	1
1.2 Experimental evidence for Dark Matter	3
1.2.1 Galaxy rotation curve	4
1.2.2 Gravitational lensing and Bullet Clusters	5
1.3 Composition of the Universe	9
1.4 Dark Matter candidates	11
1.4.1 Axions	12
1.4.2 Weakly Interacting Massive Particles	13
2 The Dark Sector and Dark Photon	17
2.1 Unexplained phenomena in the Standard Model	17
2.2 Dark Sectors and portals	18
2.3 Anomalous magnetic moment	19
2.4 Dark Photon kinetic mixing model	21
2.5 Dark Photon mass generation	21
2.6 Dark Photon production	22
2.7 Dark Photon decays	25
2.8 Dark Photon experimental searches	26
2.8.1 Visible decay search techniques	26
2.8.2 Invisible decay search techniques	28
2.9 Dark Higgs	30
2.10 Dark Higgs production	30
2.11 Dark Higgs decays	31
2.12 Dark Higgs experimental searches	32
3 The PADME experiment at the Laboratori Nazionali di Frascati	35
3.1 Frascati linac test facility	35
3.2 PADME experiment at LNF	38
3.3 Production of A' at PADME	39
3.4 PADME physics case and general layout	42
3.4.1 The active diamond target	43
3.4.2 The dipole magnet	45
3.4.3 The vacuum system	47

3.4.4	The charged particles Veto detectors	47
3.4.5	The electromagnetic calorimeter	49
3.4.6	Small Angle Calorimeter	51
3.5	PADME trigger and data acquisition system	51
3.5.1	L0 trigger	53
3.5.2	L1 trigger	53
3.6	GEANT4 simulation	54
3.6.1	Kinematics and beam simulation	55
3.6.2	Detector simulation	55
4	Positron momentum reconstruction	57
4.1	Analytical model for the momentum reconstruction	57
4.2	MonteCarlo simulation	60
4.2.1	Momentum reconstruction technique	61
4.2.2	Single Particle	64
4.2.3	Full Bunch Structure	69
5	Dark Higgs-like event selection	71
5.1	QED background processes	71
5.2	Event reconstruction	72
5.2.1	Photon collection simulation	74
5.2.2	Particle reconstruction	75
5.2.3	Particle time correction	75
5.3	Event selection and background estimates	77
6	Conclusions and future perspectives	83
	Bibliography	84

Introduction

The last decades of astronomical and cosmological observations have shown that our knowledge of the Universe covers a minimum part of it: the Standard Particle Physics Model describes only 5% of the total energy density components. The largest part, accounting for 68% of the total, seems to consist of the so-called Dark Energy, an unknown form of energy introduced to explain the accelerated rate of expansion of the Universe. The remaining 27% appears to be made of non-baryonic and non-luminous matter, which for this reason is called Dark Matter.

The extreme difficulty in Dark Matter detection could be explained speculating that Standard Model and Dark Matter particles live in two separate sectors connected by a portal. The simplest model for this theory adds a new gauge group having $U_D(1)$ symmetry which introduces a new boson A' , called Dark Photon. A' therefore represents the mediating particle of the electromagnetic interaction between Dark Matter particles. This new sector, and therefore the new boson introduced, is expected to couple with the electromagnetic field of the Standard Model with an intensity factor ϵ of the order of 10^{-3} or smaller. Many experiments in recent years have focused their attention on the production of this new vector boson, searching for it both in invisible and visible ways of decay.

Among these lies the PADME experiment, which aims to measure processes $e^+e^- \rightarrow A'\gamma$ in the interaction of a positrons beam with the electrons of a diamond target, using the beam extracted from the DAΦNE linac at the National Laboratories of Frascati, LNF. The used technique is that of the missing mass $M_{miss}^2 = (P_{e^-} + P_{beam} - P_\gamma)^2$ in which only known kinematic variables are used. The presence of a vector boson A' would manifest as a narrow peak in the spectrum of the variable M_{miss}^2 at the value of its mass.

Although PADME was designed to the search for the Dark Photon, other Dark Matter events can be observed with this experiment. One of these is the Dark Higgs'-strahlung process. The Dark Higgs, indicated with the symbol h' , is needed in models where the dark photon mass is generated through the spontaneous symmetry breaking mechanism. This particle can be produced in PADME via the reaction $e^+e^- \rightarrow A'h'$. If $m_{h'} \geq 2m_{A'}$ the Dark Higgs decays in a couple of Dark Photons, which in turn decay into a couple of leptons, and the final state of this reaction will result in six charged leptons, respectively three positrons and three electrons.

This experimental thesis, carried out within the PADME collaboration, is focused on the search of background events to the Dark Higgs decaying into six charged leptons, exploiting the PADME simulation, developed using the GEANT4 framework.

In chapter 1, evidences of the existence of Dark Matter are summarised, followed by a description of the two most common Dark Matter candidates.

In chapter 2 the theoretical models of the Dark Photon and its experimental research methods will be discussed followed by a presentation of the Dark Higgs, main topic of this thesis.

In chapter 3 a PADME introduction will be given, with its Dark Photon research approach and with a detailed description of the experimental apparatus and of its Monte Carlo simulation, with which this thesis has been carried out.

In chapter 4 the first part of the work of this thesis will be presented, where the reconstruction of the momentum of the charged particles revealed in the PADME experiment, will be illustrated.

In chapter 5 the main argument of this thesis work will be shown: the search for six charged leptons candidates as background events for the Dark Higgs study.

Subsequently, the conclusions and the future prospects of this work will follow.

Chapter 1

The Dark Matter problem

In this chapter, after a brief introduction to the Standard Cosmological Model, we will present some of the experimental evidences for the existence of Dark Matter. A short description of the components of the Universe and possible Dark Matter candidates will conclude the chapter.

1.1 Standard Cosmological Model

The current cosmological model is based on three fundamental ingredients [1]:

- *Einstein equations*, relating the geometry of the Universe with its matter and energy content;
- *metrics*, describing the symmetries of the problem;
- *equation of state*, specifying the physical properties of the matter and energy content.

The Einstein equations, also known as Einstein Field Equations (EFE) are 10 equations in Albert Einstein's general theory of relativity, which describe the fundamental interaction of gravitation as a result of spacetime being curved by mass and energy. The EFE may be written in the following form:

$$R_{\mu\nu} - \frac{1}{2}g_{\mu\nu}R = -\frac{8\pi G_N}{c^4}T_{\mu\nu} + \Lambda g_{\mu\nu} \quad (1.1)$$

where $R_{\mu\nu}$ and R are, respectively, the Ricci tensor and scalar, obtained by contraction of the Riemann curvature tensor, $g_{\mu\nu}$ is the metric tensor, G_N is Newton constant, $T_{\mu\nu}$ is the energy-momentum tensor, Λ is the cosmological constant and c is the speed of light.

The terms on the left-hand-side describe the geometry of the Universe, which is determined by its energy content, parameterised by the energy-momentum tensor on the right-hand-side. This relationship between the matter content and geometry of the Universe is the key concept of general relativity.

The cosmological constant term Λ was originally introduced by Einstein to allow a static universe, since his theory predicted a dynamic, contracting or expanding, universe. This effort was unsuccessful because:

- the universe described by this theory was unstable;
- observations by Edwin Hubble confirmed that our Universe is expanding.

After such new discoveries, the cosmological constant term Λ began to represent the vacuum energy, a source of gravitational field even in the absence of matter. The solutions of the EFE require prior knowledge of the symmetries of the problem. Statistical homogeneity and isotropy of the Universe, confirmed by many observations, greatly simplifies the mathematical analysis. Such properties imply a specific form of the metric, known as the Robertson-Walker metric:

$$ds^2 = dt^2 - a^2(t) \left(\frac{dr^2}{1 - kr^2} + r^2 d\theta^2 + r^2 \sin^2 \theta d\phi^2 \right) \quad (1.2)$$

where r , θ and ϕ are the fixed comoving coordinates of the observer, $a(t)$ is the cosmic scale factor as a function of time that describes the expansion or contraction of the Universe and k is the parameter that defines the Universe curvature. The energy content of the Universe is directly connected with k , which can assume three different values:

- $k = -1$, hyperbolic curvature for an open, infinite Universe;
- $k = 0$, no curvature for a flat infinite Universe;
- $k = 1$, spherical curvature for a closed and finite Universe.

The simplest case, $k = 0$, represents the flat Euclidean space. The EFE can be solved with this metric. One of its components leads to the Einstein-Friedmann equations, which determine the time evolution of the cosmic scale factor as a function of the cosmological constant Λ , the cosmic substrate density $\rho(t)$ and the pressure $p(t)$:

$$\left(\frac{\dot{a}(t)}{a(t)} \right)^2 = \frac{8\pi G_N}{3} \rho(t) - \frac{k}{a^2(t)} + \frac{\Lambda}{3}. \quad (1.3)$$

$$\frac{\ddot{a}(t)}{a(t)} = -\frac{4\pi G_N}{3} (\rho(t) + 3p(t)) + \frac{\Lambda}{3} \quad (1.4)$$

It is useful to introduce the Hubble parameter $H(t) = \frac{\dot{a}(t)}{a(t)}$, which describes the expansion rate of the Universe. A recent estimate of the present value of the Hubble parameter (also referred as the Hubble constant, H_0) is $H_0 = 67.66 \pm 0.42 \text{ kms}^{-1} \text{ Mpc}^{-1}$ [2].

From the Einstein-Friedmann equation, expressed in Eq. 1.3, the Universe become flat ($k = 0$), with a vanishing Λ model, when the energy density equals the critical density ρ_c :

$$\rho_c \equiv \frac{3H_0^2}{8\pi G_N} \quad (1.5)$$

Defining the density parameter Ω_x of a substance of species x and the density ρ_x as:

$$\Omega_x \equiv \frac{\rho_x}{\rho_c} = \frac{8\pi G_N \rho_x}{3H_0^2} \quad (1.6)$$

and the sum of all the parameters:

$$\Omega = \sum_x \Omega_x \quad (1.7)$$

it is possible to rewrite the Eq. 1.3, removing the explicit time dependency, as:

$$1 = \Omega_m + \Omega_k + \Omega_\Lambda \quad (1.8)$$

where Ω_m is the matter density parameter and Ω_k is the radiation one.

The obtained equation states that the present total energy density of the Universe is directly linked to its curvature. In a quantum field theory framework, the parameter Ω_Λ can be interpreted as the energy density of the vacuum and is estimated to be $\Omega_\Lambda = 0.6889 \pm 0.0056$ [2] in the best models describing the Universe. Its negative pressure accounts for a repulsive gravitational interaction in general relativity. As a consequence of that, models with a positive Ω_Λ present a slowed down expansion that can become an accelerated expansion in a later phase of the Universe. Therefore it is fundamental to determine the values of the three variables H_0 , Ω_m and Ω_Λ to understand the ultimate fate of all cosmological models with $\Omega_\Lambda \neq 0$.

1.2 Experimental evidence for Dark Matter

Hints of the existence of non-luminous matter came from a cluster of galaxies. In 1933, the astronomer Fritz Zwicky of the California Institute of Technology, with an 18-inch Schmidt telescope built by Caltech, began to study the Coma Cluster, a cluster of thousands of galaxies about 20 million light-years wide, around 350 million light years away from Earth in the direction of the constellation named Coma Berenices.

By measuring the total mass of the cluster, its total luminosity, the number of visible galaxies, their radial velocities and using the Doppler shift of the light emitted, Zwicky obtained the total energy of motion and the gravitational one of the cluster, respectively the kinetic and the potential energies of the system. According to the virial theorem, he expected in the cluster, which is a closed system, the kinetic energy to be half the potential one. This was not the case. The obtained results showed that the single galaxies moved too fast for the cluster to remain compact. With such velocities, the galaxies would not have been seen clustered, but escaping from each other.

To reconcile the observed velocities of the cluster members with the virial theorem, Zwicky postulated that the cluster could also contain some invisible matter, with a mass exercising a gravitational attraction but not emitting light, therefore not contributing to the galaxy luminosity [3]. He called this unseen mass *Dunkle Materie* (in English Dark Matter, DM), estimated to be at least 500 times the visible one.

After the birth of X-ray astronomy, it was discovered that much of this missing mass was in the form of hot gases, which are powerful X-ray emitters, that contribute to the total mass of the galaxies much more than the visible stars [4]. However, even

taking into account the gases, a significant contribution was still missing to the total mass balance, about six times the visible mass.

1.2.1 Galaxy rotation curve

The most convincing and direct evidence of DM, after Zwicky observation, came in the early 70s, when Vera Rubin and Kent Ford of the Carnegie Institution of Washington started to study the rotation curves of spiral galaxies, consisting of a central bright bulge surrounded by a rotating disk of younger stars. A rotation curve is a graph of the rotational velocities of stars and gas, in an astronomical system, as a function of their distance from the center of the galaxy.

According to the Newton law of gravitation, the rotational velocity around the center decreases as the square root of the distance from the center. Combining this law with the centripetal acceleration a of an object in circular motion:

$$F = ma = \frac{G_N m M(r)}{r^2}; a = \frac{v^2}{r} \quad (1.9)$$

where m is the mass of the considered object and r its distance from the rotation center, where all the mass $M(r)$ contained in the sphere of radius r can be considered as concentrated (using the Gauss theorem), we get that:

$$\frac{G_N m M(r)}{r^2} = \frac{mv^2(r)}{r} \rightarrow v(r) = \sqrt{\frac{G_N M(r)}{r}} \quad (1.10)$$

This behaviour was observed when the rotation curve of the Solar System was measured. Rubin and Kent expected to find this result for spiral galaxies too but, on the contrary, they found out that in galaxies the rotational velocity at high distance from the galaxy center was almost constant, as shown in Fig. 1.1.

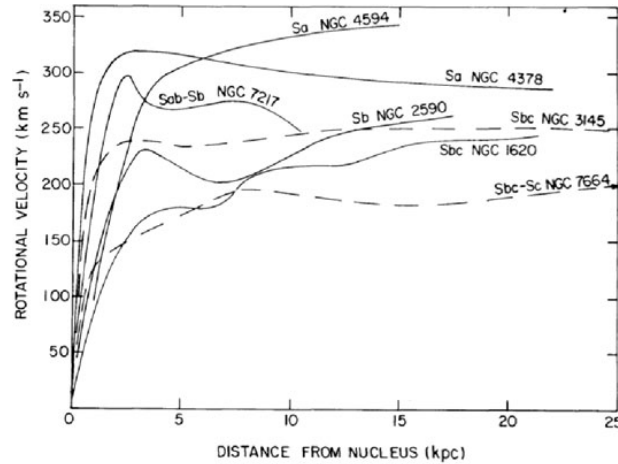


Figure 1.1. Picture from Rubin's 1978 paper shows rotational velocities for seven of the 10 galaxies the team studied. If visible matter were the only matter present, the curves would dive back down on the far right. Their flatness indicates that, assuming our understanding of gravity is correct, additional unseen matter exists in the galaxies. Figure from [5].

Using the Newtonian Mechanics and assuming that the gravitation model is correct, the straightforward implication is that the mass distribution in galaxies cannot be described only with the visible mass in the galactic bulge, where the largest part of the mass is seen.

In Eq. 1.10 $M(r) \equiv 4\pi \int \rho(r)r^2 dr$, where $\rho(r)$ is the mass density profile, that should be falling $\propto 1/\sqrt{r}$ beyond the optical disc. The fact that the velocity $v(r)$ is approximately constant implies that every galaxy is immersed in a wider dark component, a sort of spherical density halo with $M(r) \propto r$ and $\rho \propto 1/r^2$. An example of this behaviour is given in Fig. 1.2, where the rotation curve of NGC 6503 is shown.

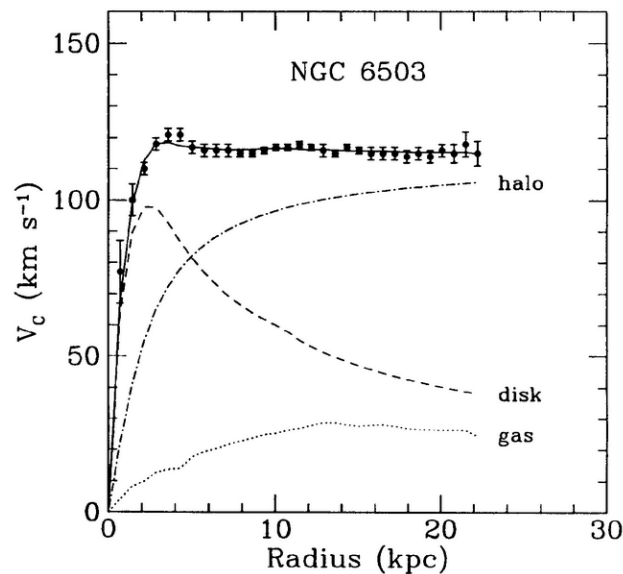


Figure 1.2. Rotation curve of NGC 6503 where circular velocities of stars and gas are shown as a function of their distance from the galactic centre. The dotted, dashed and dash-dotted lines are respectively the contributions of gas, disk and of the halo of non visible matter needed to explain the galaxy radial velocity distribution using the newtonian law, namely the DM. The rotation velocities of stars and gas first increase as the radius increases and then become constant or change very slowly. The DM mass increasingly contributes at large distances and maintains the flat part of the rotation curve over about ten dynamical scales. Figure from [6].

There are other compelling findings of this hypothesis: vertical velocity dispersion supports the fact that the DM can not be stored in the disk alone, as well as material rotating perpendicular to the regular disk, resulting in a gravitational potential that is almost spherical [7].

1.2.2 Gravitational lensing and Bullet Clusters

Gravitational lensing is an astronomical effect of Einstein's theory of general relativity in which mass is capable to bend light [8]. It works in a similar way as normal lenses, which bend light rays that pass through them by means of refraction, in order to focus the light somewhere else.

The gravitational field of a massive object, such as galaxies and clusters of galaxies, will extend far into space and cause light rays passing close to that object, thus through its gravitational field, to be bent and refocused somewhere else. Even smaller objects such as stars and planet can lens light. The more massive the object is, the stronger is its gravitational field and hence its ability to bend light rays. A schematic view of the gravitational lensing is shown in Fig. 1.3.

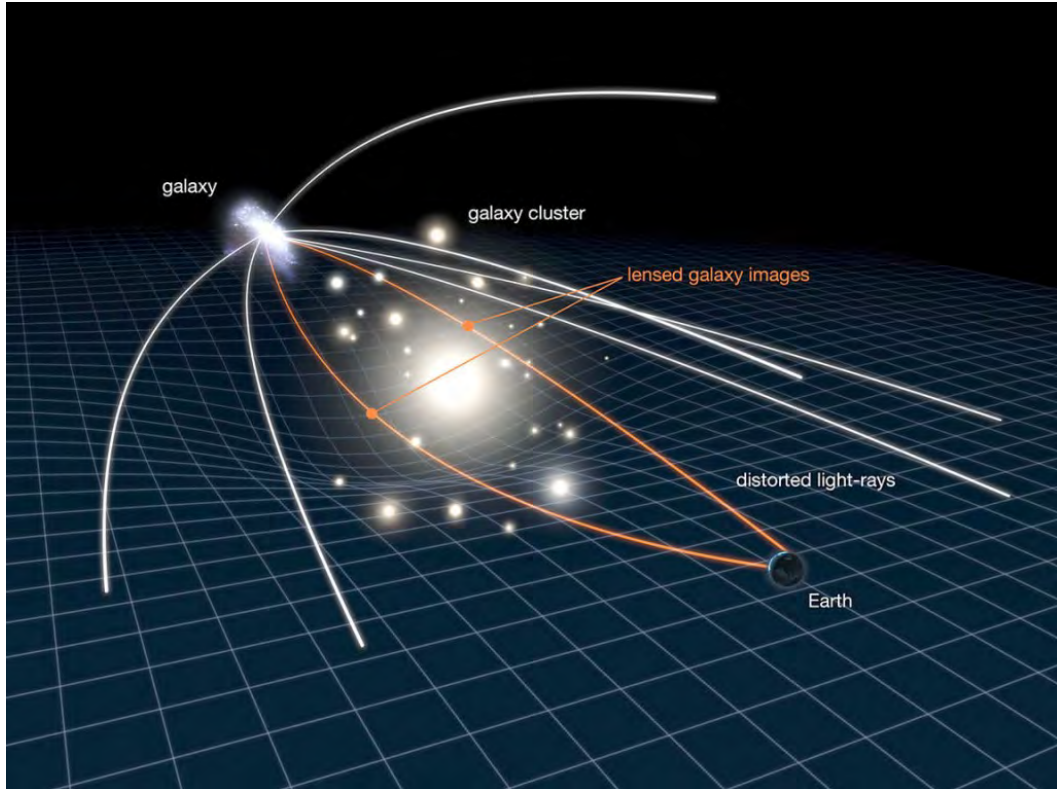


Figure 1.3. Gravitational lensing schematic. The light from a distant galaxy is distorted by the gravitational effects of a galaxy cluster, which acts like a lens. In this case the distorted light-rays are focused to the Earth.

Interesting results come from lensing on the largest scales, by looking at galaxies and clusters of galaxies. In fact, between the Earth and those galaxies there is a large quantity of DM. Light-rays coming from distant galaxies that passes close to a cluster may be distorted by its invisible mass. It is the gravitational field of DM in the cluster that does almost all of the lensing. An example on the effects of DM on lensing is illustrated in Fig. 1.4, where the Abell 2218 cluster is shown.

Due to gravitational lensing, multiple images of the same galaxy can be form. This occurs because light rays from a distant galaxy that would otherwise diverge may be focused together by lensing. From the point of view of an observer on Earth, it looks as if two very similar light rays have travelled along straight lines from different parts of the sky. To determine which images come from the same galaxy the atomic spectroscopy is used. An example of multiple images is shown in Fig. 1.5.

Like in Abell 2218 cluster, if the lensing effect is strong enough to be seen on

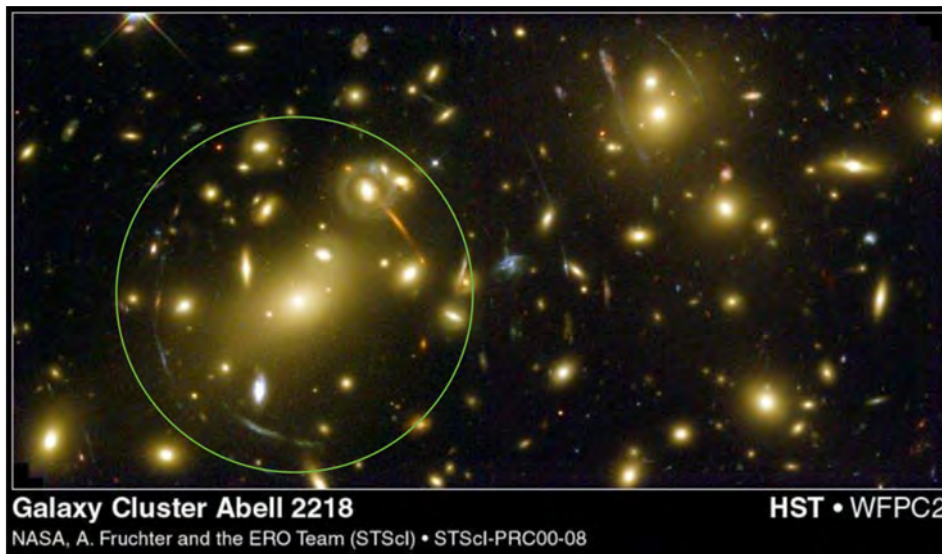


Figure 1.4. The Abell 2218 cluster. The images of the distant, lensed galaxies are stretched and pulled into arcs as the light passes close to the foreground cluster. However, because of lensing, these are not the real shapes of the galaxies. Usually, they are elliptical or spiral shaped. Image from Hubble Space Telescope [9].

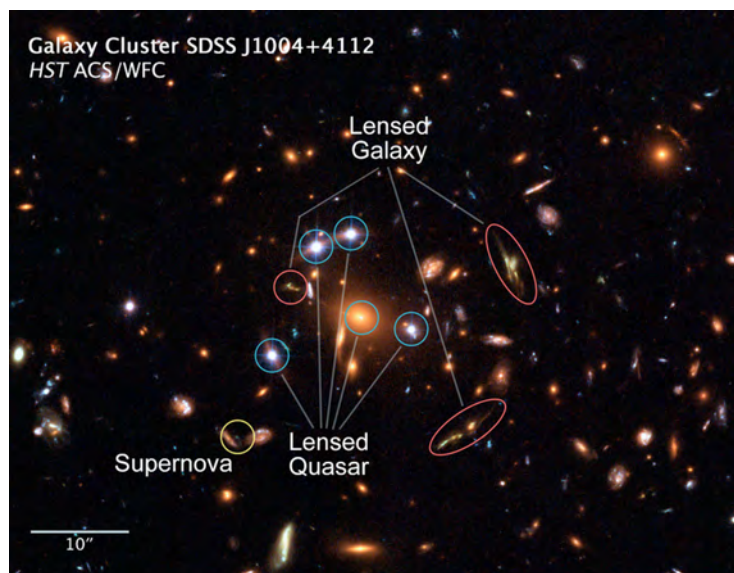


Figure 1.5. Multiple images from the gravitational lensing. Here, there are three images of the same galaxy (orange circles) and five images of the same quasar (blue circles) in different places. From the Hubble Space Telescope [9].

an astronomical image, it is called *strong lensing*. This happens when the bending cluster, between galaxies and the Earth, is really massive. However, since there are not so many big clusters in the sky, the strong lensing is a very rare effect. The most common gravitational lensing is called *weak lensing*. This effect is due to the DM presence between us and every distant galaxy: most galaxies are lensed by the DM's gravitational field such that their shapes are altered by only 1%. This particular lensing could explain how DM behaves across the whole sky.

To understand how strong the weak lensing effect is on a particular galaxy, it is essential to know the average lensing effect on a set of galaxies. To do so, there must be some assumptions: all galaxies must be roughly elliptical in overall shape and must be orientated randomly on the sky, as illustrated in Fig. 1.6.

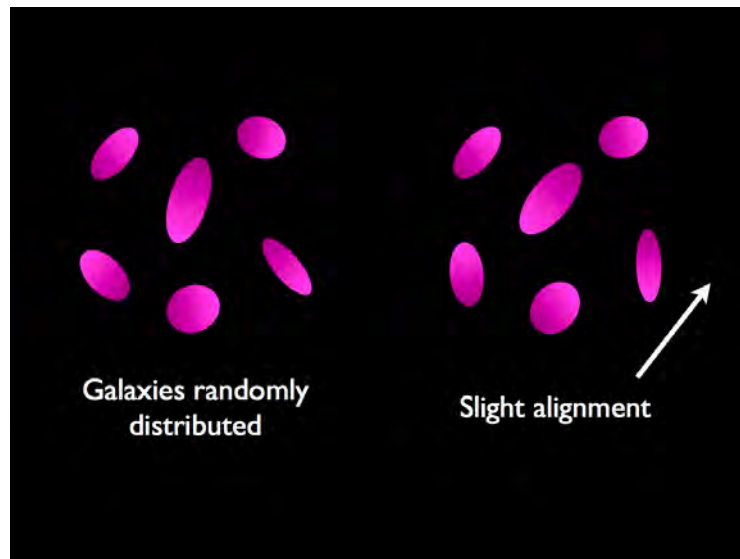


Figure 1.6. Weak lensing schematic. The galaxies have an elliptical shape and are orientated randomly in the sky. The presence of DM produces a weak lensing that distorts the images of the galaxies in a portion of the sky, aligning them slightly.

In presence of a weak lensing effect, the galaxies align themselves together slightly and their images are stretched in the same direction. In this way, any deviation from a random distribution of galaxy shape orientations is a direct measure of the lensing signal in that part of the sky. Weak lensing can thus be used to measure the gravitational lensing signal on any part of the sky.

Gravitational lensing has also been used to verify the existence of DM itself. The image shown in Fig. 1.7 is a picture of the *Bullet Cluster*, and it has been observed in both optical (visible) light and in X-ray. It consists of two colliding galaxy clusters. Using gravitational lensing and X-ray imaging, we can visualise the behaviour of different forms of matter after a galaxy cluster collision. The pink part of this image is reconstructed from data of the satellite Chandra, observing the intensity of X-rays emitted by the cluster. This corresponds to the luminous intra-material distribution, which shows the deformation, deceleration by friction and the coalescence which is expected after such a collision for ordinary matter. Interact with each other through both gravity and electrostatic forces, slowing and shocking one another. The blue

part, on the contrary, is the mass density reconstructed through gravitational lensing. The distribution shows that the majority of the mass of the two clusters passed through the collision without much interaction, being, therefore, in advance with respect to the luminous mass.

Based on all these evidences, DM accounts for about 85% of the mass of galaxies and their clusters. A recently discovered galaxy, named Dragonfly 44, is even suspected to contain 99.9% of DM [10].

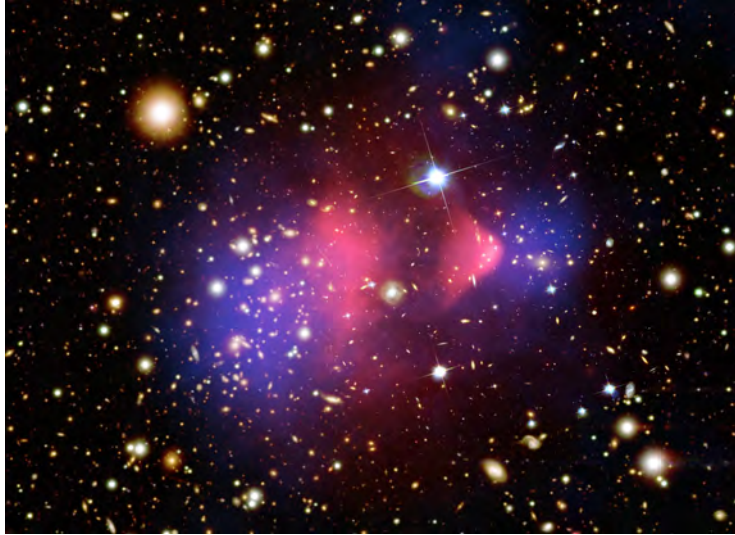


Figure 1.7. The galaxy cluster 1E0657-56, also known as the *Bullet Cluster*. Color code: X-rays from intra-cluster medium (accounts for the largest baryonic fraction) in Pink from Chandra telescope[11], Optical (galaxies) in White/Orange from Magellan[12] and Hubble telescopes[13] and Lensing Map in Blue. Since there are two different lens centres, one can conclude that DM is the predominant mass component of the cluster. Figure from [14].

1.3 Composition of the Universe

The simplest way to explain this apparent mass deficit is to postulate that the halo surrounding the galaxy is occupied by not yet observed elementary particles, which are electrically neutral, stable and massive. The fact that these particles are neutral explains why they are invisible, because they are unable to emit electromagnetic radiation. To justify their gravitational effects, they have to be massive. There are many good reasons supporting the particle hypothesis.

First of all, each physical phenomenon known is defined at a fundamental level by the combinations and interactions between the well-determined elementary particles, according to the laws that have been confirmed in the experiments. Therefore it is reasonable to think that this corpuscular pattern of regular matter is also replicated by a "dark world".

The second reason is based on experience. In Physics, historically, several issues were solved by introducing new ad-hoc particles. The most well-known example is

the neutrino. In the 30s, analysis of some phenomena of radioactive decay showed an alarming inexplicable violation of the law of conservation of energy, stating the total energy in every isolated system remains constant whichever physical process is subjected to. In the mentioned processes, instead, a significant part of the initial energy seemed to come to nothing. So, the Austrian physicist Wolfgang Pauli hypothesised this energy was taken away by a very light neutral particle, with such elusive characteristics it could not be observed. Enrico Fermi started from Pauli idea and elaborated a rigorous theory for this kind of processes (the so-called beta-decays), naming the new mysterious particle neutrino. Fermi theory was so elegant and described with such precision the dynamics of beta processes that the existence of neutrino was accepted even in the absence of any direct evidence. It took more than two decades before the American physicists Frederick Reines and Clyde Cowan finally managed to capture some neutrinos produced by a nuclear reactor.

But the most convincing evidence supporting the particle nature of DM is cosmological. Further evidence for DM comes from measurements on cosmological scales of anisotropies in the Cosmic Microwave Background (CMB) [15]. The CMB is the leftover radiation from the Universe's warm early times. The photons underwent oscillations that froze in at a redshift of 1100 shortly before decoupling from the baryonic matter. The angular scale and height of these oscillation's peaks (and troughs) are important probes of cosmological parameters, including total energy density, the baryonic fraction, and the component of DM [16], as shown in Fig. 1.8.

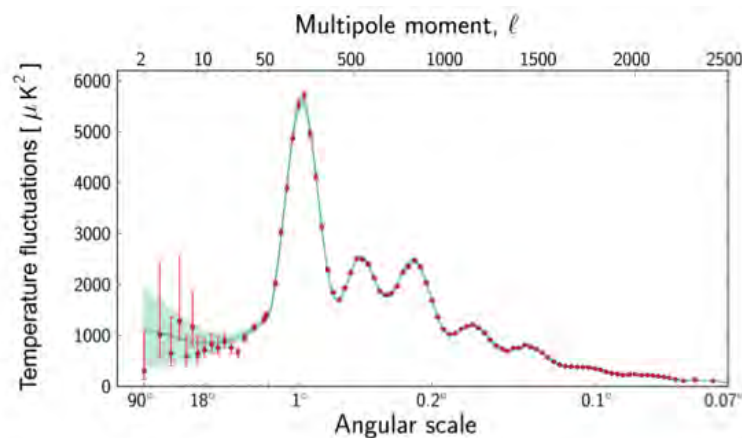


Figure 1.8. Planck power spectrum of temperature fluctuations in the cosmic microwave background. The fluctuations are shown at different angular scales on the sky. Red dots with error bars are the Planck data. The green curve represents the standard model of cosmology, Λ CDM. The peak at 1 degree is consistent with a flat geometry of the Universe, the height of the second peak tells that the 5% of the Universe energy density is made of ordinary matter, while the second and third peaks indicate that the 26% of the Universe energy density consists of DM. Figure adapted from the public version available at Wikimedia Commons, courtesy of the European Space Agency.

The sound horizon at last scattering provides a ruler stick for the geometry of the Universe: if the light travels in a straight line (as would be the case with a flat geometry), then it was expected that the angular scale of the first Doppler peak would be found at 1 degree, which is what happens. Thus the geometry is flat,

corresponding to an energy density of the Universe of $\sim 10^{-29} \text{g/cm}^3$. The second peak's height means that 5% of the total energy density is made of ordinary atoms, while matching all the peaks implies that 26% of the total energy density is DM.

The remaining quantity is called Dark Energy (DE). The first proof for the Universe's 70% DE came from distant supernovae findings [17][18][19]. The supernovae are dimmer than expected, as is most easily explained by an accelerating Universe. There are two different theoretical approaches currently pursued to explain the DE:

- a vacuum energy such as a cosmological constant or time-dependent vacuum may be responsible [20];
- it is possible that General Relativity is incomplete and that Einstein equations need to be modified [21][22].

However, this DE does not resolve or contribute to the question of DM in galaxies, which remains puzzling as eighty years ago.

We now have a Universe concordance model in which about a quarter of its content is DM. A summary of what we have just discussed is shown in Fig. 1.9.

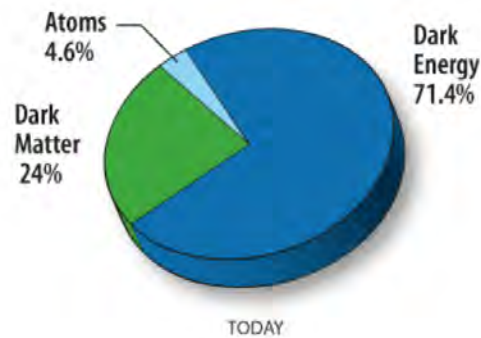


Figure 1.9. Relationship between dark energy, dark matter and baryonic matter content of the Universe derived from WMAP measurements (NASA 2013).

1.4 Dark Matter candidates

As seen in the previous section, several observations at all astrophysical scales support the existence of DM. In addition, it also results that galaxies contain a much larger fraction of DM than baryonic matter (about five times more). Given all this, the particle/s that make up the DM are very little understood. The constraints that arise from observations are:

- DM must be stable, or at least with a long life time compared to the present age of the Universe;
- DM is probably only gravitationally/faintly interacting, since, despite its large amount, it is hard to directly detect and because of upper limits on self-interactions from astrophysical observations;

- DM nature is non baryonic, due to big bang nucleosynthesis and CMB observations, in addition to the fact that it seems to not interact with light;
- DM is slow moving, since CDM models better reproduce the current Universe structure and content.

There are many candidates for DM particles, with masses ranging from 10^{-5} eV up to $10^4 M_\odot$, for black holes. There are some historical possibilities that don't respect one or more of the above criteria. For example, baryonic candidates are MAssive Compact Halo Objects (MACHOs) [23][24][25][26], such as brown dwarfs (H and He balls with masses below $0.08 M_\odot$), jupiters (masses near $0.001 M_\odot$), stellar black-hole remnants (masses near $100 M_\odot$) and neutron stars. Experiments such as EROS have discarded these hypotheses, putting a strict limit on tMACHOs fraction in the halo composition (in the case of EROS, less than 25% [27]).

A possible explanation of the behaviour found at different scales is to change the gravitational dependency on distance, decreasing it less rapidly than $1/r^2$. The possibility has been taken into account since the laws of Newton were never tested at very low accelerations, such as those at very large distances due to gravity. Milgrom [28] presented the theory for the first time in 1983 under the title MODified Newtonian Dynamics (MOND). The idea is to substitute $\vec{F} = m\vec{a}$ with:

$$\vec{F} = m\mu\left(\frac{a}{a_0}\right)\vec{a} \quad (1.11)$$

where $\mu(x) = 1$ for $x \gg 1$ or $\mu(x) = x$ for $x \ll 1$ and a_0 is the constant that marks the transition between the standard Newtonian regime and the MOND one. Nevertheless, through gravitational lensing of colliding galaxy clusters, the presence and superiority of DM on a large scale is confirmed, as explained before.

The two leading candidates for this DM are Axions and Weakly-Interacting Massive Particles (WIMPs). Such candidates will be discussed in the following subsections.

1.4.1 Axions

Axions are hypothetical particles that Peccei and Quinn introduced in 1977 in an attempt to solve the Strong CP problem (strong force was found not to violate CP as predicted by quantum chromodynamics [29]). In fact, from classical physics calculations, the neutron electric moment should be several orders of magnitude larger than the current experimental upper limit of $10^{-26} e \text{ cm}$ [30]. The theory presupposes the presence of a hidden global U(1) symmetry, called the Peccei-Quinn (PQ) symmetry, which spontaneously breaks, producing a new pseudo-Nambu-Goldstone boson. This particle, the Axion, relaxes to zero the CP violation term. The axion mass is connected to the PQ symmetry by the formula:

$$m_a \simeq 6 \mu\text{eV} \cdot \left(\frac{10^{12} \text{ GeV}}{f_a}\right) \quad (1.12)$$

where f_a is the axion decay constant and is proportional to the expected vacuum value which breaks the symmetry of PQ. Axion mass is unknown, but there are limits on f_a . The duration of the SN1987A neutrino burst provides the limit $f_a \geq 10^9 \text{ GeV}$

[31], whereas the size of the axion energy could not be too high, otherwise the early Universe would have collapsed, hence $f_a \leq 10^{12}$ GeV [32][33][34]. This binds the axion mass in the range that goes from μeV to meV [35]. The axion-photon coupling $g_{a\gamma\gamma}$ is proportional to the axion mass:

$$g_{a\gamma\gamma} = \frac{\alpha g_\gamma}{\pi f_a} \quad (1.13)$$

where α is a constant fine structure and g_γ is an order 1, model-dependent, dimensionless coupling parameter [36]. Axions can be created as a non-relativistic condensate in the early Universe [33]. The mean density of the axion relic can be calculated as:

$$\Omega_a h^2 \approx \left(\frac{f_a}{10^{12} \text{GeV}} \right)^{7/6} \quad (1.14)$$

Axion coupling to matter is extremely small, but a resonant cavity and a strong magnetic field will induce its decay into two phonons. All the techniques of axion detection are based on the use of this possibility.

Some ongoing studies, such as CAST [37] (Sun axions), ADMX [38] (DM halo axions) and PVLAS [39] (laboratory axions), are attempting to detect axions, without any positive results. Ongoing and future experiments are expected to test the axion couplings to different particles and set limits on the axion contribution to the Universe's DM content.

1.4.2 Weakly Interacting Massive Particles

A highly suitable DM candidate is represented by the Weakly Interacting Massive Particles (WIMPs), generally denoted by χ . A point in their favour is that in many particle models, such as Supersymmetry (SUSY), they arise naturally. These hypothetical massive particles interact only weakly and gravitationally, are non-relativistic (CDM) and can be produced with the desired density as a Big Bang relic. The particles χ were in thermal equilibrium in the very early Universe because the temperature was much higher than their mass: $T \gg M_\chi$. This resulted in a continuous creation and destruction process: $\chi\bar{\chi} \iff \bar{l}l$ where \bar{l} may be quark-antiquark, lepton-antilepton pairs, Higgs and/or boson pairs if the mass M_χ is larger than twice the masses of these particles. In an ideal gas, the number density of these relativistic particles is $n_\chi \propto T^3$. With temperature lowering, at the moment of falling below M_χ , the particle number density falls exponentially like $n_\chi \propto e^{-M_\chi/T}$ and the annihilation rate of the WIMPs $\Gamma_\chi = \langle\sigma v\rangle n_\chi$, where σ is the thermal averaged total annihilation cross section and v is the relative velocity, becomes smaller than the expansion rate of the Universe, that is $\Gamma_\chi < H$. The annihilation of the particles then becomes inefficient and a relic abundance remains (they freeze-out). Using Boltzmann equation it is possible to evaluate the WIMP matter contribution:

$$\Omega_\chi = \frac{8\pi G}{3H_0^2} M_\chi n_\chi \approx \left(\frac{3 \times 10^{-27} \text{ cm}^3 \text{ s}^{-1}}{\langle\sigma v\rangle} \right) \frac{1}{h^2} \quad (1.15)$$

which approximation is independent from M_χ , and dependent only from the total annihilation cross section. Numerical solutions for the Boltzmann equation are

shown in Fig. 1.10.

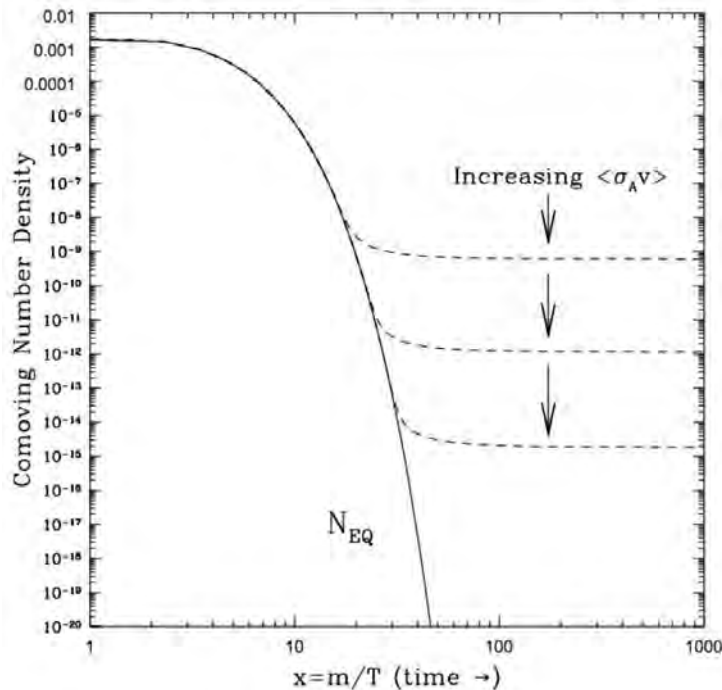


Figure 1.10. WIMP co-moving number density as a function of the inverse of the temperature (in units of M_χ). Solid line represents the equilibrium, while the dashed lines represent the current abundances for different values of $\langle\sigma v\rangle$ (velocity-weighted annihilation cross-section). The freeze-out occurs when the reaction rate drops below the expansion rate (for $T < M_\chi$). Figure from [40].

The abundances at equilibrium (solid line) and at present-day (broken lines) per co-moving volume are plotted as a function of m_χ/T , which increases with increasing time. As the cross section of annihilation increases, the WIMPs stay longer in balance and today's relic abundance is smaller.

The DM problem does not seem to be solved within the SM, so a new paradigm is required. Supersymmetry (SUSY) provides a possible solution. The SUSY theory was developed to solve the problems of particle physics mass hierarchy as well as to unify all non-gravitational forces towards a Great Unified Theory (GUT). Every particle in this model has a supersymmetric partner. The new symmetry connects elementary particles, with a certain spin, to another particle with spin varied by half of a unit, which is known as super-partners. Because none of these supersymmetric partners have been found, it is appropriate to break the symmetry to allow the super-partners to have a much higher mass to allow them not to be discovered yet. A new quantity, called R-parity, is introduced, defined as:

$$R = (-1)^{3(B-L)+2S} \quad (1.16)$$

with B, L and S baryon, lepton and spin operators, respectively, while it results $R = 1$ for ordinary particles and $R = -1$ for super-partners. When R-parity is broken, means that no selection rules are in place to avoid the decay of the supersymmetric

particles with masses of few GeV or larger. R-parity violation scale controls the intensity of baryon and lepton number violation processes, that have not been observed so far, putting severe constraints on violation of R-parity. If this R number is preserved, a lightest supersymmetric particle (LSP) must be stable.

The smallest SUSY extension to the SM is called Minimal Supersymmetric Standard Model (MSSM). In [41] it is presented an introduction to the SUSY model with motivation, Lagrangian construction, supersymmetric particles, MSSM and some his extensions.

Assuming supersymmetric models with the LSP being the lightest mass eigenstate of a positive spin superposition of 1/2 fermions, namely the photino (the photon super-partner), the zino (the Z^0 boson super-partner) and the higgsino (the neutral Higgs boson super-partner), the so-called neutralino turns out to be the perfect DM candidate. The cosmological abundance of the neutralino, if it were a DM particle, would be defined by the freeze-out from thermal equilibrium, while its annihilation and scattering cross sections, as well as its mass, depend on the parameters of the specific selected supersymmetric model.

No convincing experimental evidence for the existence of supersymmetric particles has been found so far, despite the strong theoretical motivation for supersymmetry. One of the prime goals of today's and next-generation accelerators is the search for supersymmetric particles, with masses claimed to be around the weak scale. In particular, the results of the Large Hadron Collider placed severe limits on the parameters of the SUSY and excluded many of the models [42]. The cosmological need for a suitable CDM candidate is the best scientific predictor of the existence of new physics before positive results from accelerators arrive.

There are other DM candidate particles beyond the mentioned neutralino, which seem almost impossible to detect at the moment. For example, the gravitino, the graviton's 3/2 spin super-partner, the gravity mediator particle from the "hidden field" and thought responsible for breaking the supersymmetry, can be a stable particle with masses in the TeV range. This would be the case if gravitino is the LSP for supersymmetric models that are R-parity-conserving. Other possibilities are the axino, the axion's spin-1/2 super-partner (discussed in the previous subsection) and the neutrino's super-partner. In addition to the ones presented, there are additional DM candidates such as Kaluza Klein particles, mirror matter, inelastic DM, self-interacting DM and various other possibilities of exotic matter.

Chapter 2

The Dark Sector and Dark Photon

The Standard Model is not a complete theory. Many of its problems, including a lack of explanation for the DM, require the existence of New Physics (NP) beyond the Standard Model. Many new physics theories exist, able to solve one or more of the SM flaws. Among this class we will consider a group of models that introduce hidden sectors to solve the DM problem. A possible solution to the DM puzzle can be given by the addition of a new $U(1)$ symmetry and its mediator called the Dark Photon (DP) and indicated with the symbol A' . This boson would be able to solve different problems including the anomalous muon magnetic momentum and, furthermore, this model can be tested with high precision in several ways by different experiments.

In this chapter, after a brief introduction to some of the problems of the Standard Model, the Dark Sector (DS) and the physics of its portals will be presented. A model including the Dark Photon and the Dark Higgs (DH) boson will be discussed, deepening their characteristics and the ways in which they can be produced in the experiments.

2.1 Unexplained phenomena in the Standard Model

The Standard Model (SM) has achieved its maximum success, as a theory able to describe the interactions between fundamental particles, with the discovery of the Higgs boson in 2012 [43][44]. Nevertheless, it is far from being a complete theory, since there are many problems and phenomena that it still cannot explain.

One of these is the DM, which is responsible for the missing mass of the Universe and is about five times more abundant than ordinary baryonic matter [45]. As it was conceived, it is not possible to incorporate the phenomenon of DM into the theory of SM. To this end, it is necessary to introduce new degrees of freedom, capable of weakly interacting with baryonic matter.

In recent years, studies on the spectrum of antiprotons and on the abundance of positron in cosmic rays, carried out by PAMELA [46], FERMI [47] and AMS [48][49], have led to postulate the existence of a possible annihilation of DM in SM particles. This process could lead to the existence of a new mediator for a possible

new interaction between DM and ordinary matter. The addition of the DM in the current fundamental particle theory could solve the big difference between the theoretical [50] and the experimental value [51] of the anomalous magnetic moment of the muon. The difference between the theory and the experimental results, which is greater than 3σ , could indicate the non-universality or the violation of the leptonic flavour. A possible solution to this problem could be the introduction, in the current theory, of a new and hypothetical light vector boson, with a mass between 10 and 100 MeV coupled with the ordinary matter [52] through a $U(1)$. All these problems highlighted so far can only be solved with NP beyond the SM. One of the most interesting extensions at low energies of the SM allows the introduction of states that are almost decoupled from the SM particles. These states are part of the DS, so named because of their extremely weak interaction with the visible one.

2.2 Dark Sectors and portals

In particle physics, the DS are the hypothetical collections of yet-unobserved quantum fields and their corresponding hypothetical particles. The interactions between DS particles and SM particles are weak, indirect, and typically mediated through gravity or other new forces, which have the quantum numbers of both the DS and the SM. Depending on the specific theory new mediators are introduced, and it is possible to have different Lagrangian terms and therefore mediators with unique characteristics. Each mediator defines a neutral portal, a way to obtain an interaction between DM and ordinary matter [53].

The possible neutral portals of the DS are listed below:

- Scalar portal: The mediator is a scalar particle, able to interact with the SM Higgs boson. This interaction adds to the SM Lagrangian the following term:

$$\mathcal{L} \sim \mu SH^+H + \lambda S^2 H^+H \quad (2.1)$$

Since the best way to look for such type of new particles is through the study of Higgs decay final states and Higgs properties, the most appropriate machines to address this scenario are the high energy colliders, like LHC;

- Pseudoscalar portal: The mediator is a particle with properties similar to the axion, which is the Goldstone boson associated to the Peccei-Quinn global symmetry breaking $U_{PQ}(1)$. This symmetry was introduced to explain the strong CP violation, not yet observed experimentally. The interaction between the axion and the SM fermions is given by the following term in the Lagrangian:

$$\mathcal{L} \sim \frac{\partial_u a}{f_a} \bar{\psi} \gamma^\mu \gamma_5 \psi_f \quad (2.2)$$

where the mass of the axion M_a and its coupling to the ordinary SM fields α_a are functions of the breaking scale f_a of the Peccei-Quinn symmetry. Other axion-like particles, also called ALPs, may as well exist and their parameters

are free. The couplings of the ALPs to photons and Standard Model fermions are also arbitrary;

- Neutrino portal: The mediator is a fermion with properties similar to a sterile neutrino. The problem of the neutrino mass origin makes this mediator a potential candidate for different models of the neutrino physics. The possible existence of a sterile neutrino adds to the Lagrangian the following term:

$$\mathcal{L} \sim Y_N L H N \quad (2.3)$$

where Y_N is the Yukawa term, L is the lepton, H is the Higgs boson and N is the sterile neutrino. Inside the SM, the sterile neutrino is a singlet and could be produced in the early Universe. If the relic abundance and interactions strength with the dark matter are sufficient, they will delay the DM kinetic decoupling and will allow the solution of the problem with the missing-small scale structures like satellite galaxies [54];

- Vector portal: The mediator is an electrically neutral vector particle, referred as the Dark Photon A' . Its interaction with the SM fermions can be written in the following form:

$$\mathcal{L} \sim g' q_f \bar{\psi}_f \gamma^\mu \psi_f A'_\mu \quad (2.4)$$

where g' is the universal coupling constant of the interaction and q_f are the corresponding charges of the interacting fermions. As can be seen, it has a non-vanishing coupling to the standard fermions.

All the interactions that require the use of a vector portal, therefore a neutral vector mediator, are grouped in the DP models. In some of this models a scalar mediator called Dark Higgs is also introduced. We will call this models Dark Higgs models.

2.3 Anomalous magnetic moment

The existence of any new vector particle including the DP, can contribute to the electron and muon magnetic moment. The magnetic moment \vec{M} of a particle of charge q with spin \vec{S} is given by the following relation:

$$\vec{M} = g \frac{q}{2m} \vec{S} \quad (2.5)$$

where m is the mass of the particle and g is the gyromagnetic factor. Given $s = 1/2$, the Dirac equation implies $g = 2$ while the SM predicts a small deviation of g for the leptons parameterised with the following quantity, called anomalous magnetic moment:

$$a = \frac{(g - 2)}{2} \quad (2.6)$$

The parameter a can be calculated with high precision considering the contributions deriving from QED, weak and hadronic interactions:

$$a^{SM} = a^{QED} + a^{EW} + a^{hadrons} \quad (2.7)$$

For the muon, this quantity was precisely calculated theoretically and measured experimentally, obtaining respectively the following values:

- $a_{\mu}^{SM} = 116591802(2)(42)(26) \times 10^{-11}$
- $a_{\mu}^{exp} = 116592091(54)(33) \times 10^{-11}$

with a difference from the theoretical value to the experimental one equal to:

$$\Delta a_{\mu} = a_{\mu}^{exp} - a_{\mu}^{SM} = 3 \cdot 10^{-9} \quad (2.8)$$

distant more than 3σ from zero.

If the DP exists, as predicted by the theory, it would contribute to the anomalous magnetic moment with an extra value, which resembles the QED lowest-order contribution, that can be determined by the following formula:

$$a_l^{A'} = \frac{\alpha_{EM}\epsilon^2}{2\pi} \cdot f(m_l, m_{A'}) \quad (2.9)$$

where α_{EM} is the fine structure constant, $\alpha_{EM}\epsilon^2 = \alpha'$ is the interaction strength between the DP and the leptons and $f = 1$ for $m_l \gg m_{A'}$ and $f = 2m_l^2/(3m_{A'}^2)$ for $m_l \ll m_{A'}$ [55]. The different contributions mentioned so far are visible in Fig. 2.1.

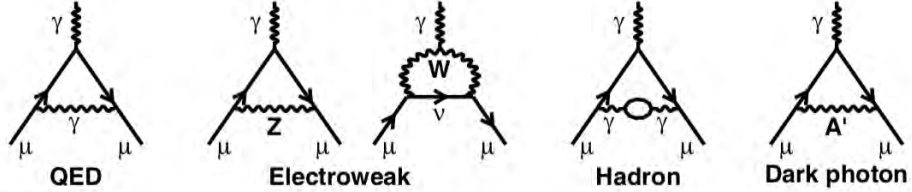


Figure 2.1. Different contributions to the anomalous magnetic moment.

With the addition of this new term, the difference between the measured value and the predicted one of the anomalous magnetic moment of the muon can be interpreted as due to the presence of the DP and used to determine the limit values for its parameters [56]. Such limits are visible in Fig. 2.2.

Thanks to a measurement of the recoil velocity of the ^{87}Rb atom when it absorbs a photon, it has been possible to evaluate the fine structure constant with a precision of an order of magnitude better than the previous value. This allowed a very precise measurement of the anomalous magnetic moment of the electron, which results to be compatible with the theoretical calculations. Consequently this sets strong limits on the DP parameters: $\epsilon^2 < 10^{-7}$ for $m_{A'} = 1 \text{ MeV}$ and $\epsilon^2 < 10^{-4}$ for $m_{A'} = 100 \text{ MeV}$ as shown by the brown diagonal in the Fig. 2.2.

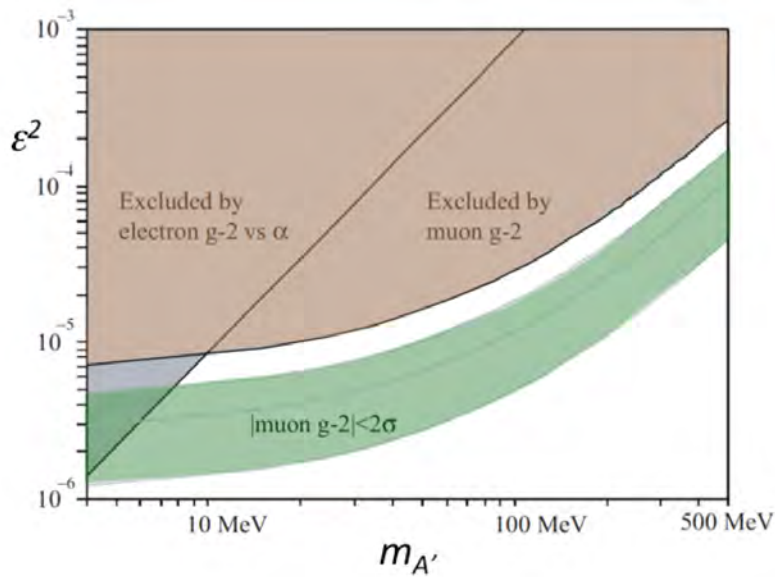


Figure 2.2. Limits on DP parameters from the electron and muon anomalous magnetic moment. The brown area is excluded while the green area is allowed by the current value of g_μ .

2.4 Dark Photon kinetic mixing model

The most commonly used model of DP is the *Kinetic Mixing*. It introduces a new symmetry group, called $U_D(1)$, responsible for the interactions between particles in the DS. In this model, the DP, also called U-boson, dark boson or secluded photon, is able to mix with the ordinary photon [57][58][59]. The corresponding Lagrangian term is:

$$\mathcal{L}_{mix} = -\frac{\epsilon}{2} F_{\mu\nu}^{QED} F'_{\mu\nu} \quad (2.10)$$

When the electroweak symmetry breaks, an effective interaction between the fermions and the DP is introduced in the following form:

$$\mathcal{L} \sim \epsilon e \bar{\psi} \gamma^\mu \psi A'_\mu \quad (2.11)$$

where ϵ is the mixing parameter, which determines all possible processes, and the fermion charges coincide with the electromagnetic ones. In this case, the DP could be either massive or massless as in [58]. The latter leads to the appearance of electrically milli-charged particles [60] which are represented by all the particles in the DS that couple to A' .

2.5 Dark Photon mass generation

The DP's mass term breaks the gauge invariance of the dark interactions and can be produced by various mechanisms [61]. One of these is *Stückelberg mechanism*. In

this way, the mass term of the gauge vector field A' could be introduced through an interaction term of A' with a scalar of the form:

$$\mathcal{L}_{mass} \sim \frac{1}{2}(\partial^\mu \alpha + mA'^\mu)(\partial_\mu \alpha + mA'_\mu) \quad (2.12)$$

In unitary gauge, this leads precisely to the well-known spin-1 mass term. These terms in the Lagrangian appear in string theories [62], for example, where the Abelian open-string gauge boson couples to a Ramond- Ramond (RR) closed-string axion. The Stückelberg mechanism could also be seen as a special case of the Higgs mechanism when the field mass of the Higgs (or more specifically the predicted vacuum value) approaches infinity. There are no extra particles required to have a massive DP in this case, and the process phenomenology does not alter with regard to the simplest effective model.

Another possible mechanism involve the *Dark Higgs*. A possible mechanism for realising such a scenario is through an additional scalar field charged under $U(1)_D$ which restores the vector boson's longitudinal polarisation. The masses of the DH and the DP arising through spontaneous symmetry breaking of the $U(1)_D$ would be of similar order. Then the additional terms to the dark Lagrangian would be:

$$\mathcal{L} \sim \frac{1}{2}m_{A'}A'_\mu A'^\mu + g'm_{A'}h'A'_\mu A'^\mu + \frac{1}{2}g'^2h'^2A'^2 \quad (2.13)$$

where h' is the DH field and g' is the $U(1)_D$ coupling constant. Thus the interactions and the parameters of the dark photon could also be probed through the searches of hidden Higgs fields.

Another way of generating masses in the dark sector, is via the *interaction of the DP with the Standard Model Higgs*. This method is theoretically possible, however the exclusion obtained by LHC disfavour the possibility of obtaining these events experimentally.

2.6 Dark Photon production

Thanks to its mixing with the ordinary photon, the Dark Photon has a very rich phenomenology and can be produced in many ways and through different experiments in which SM photon production is involved. Some common cases are shown in Fig. 2.3.

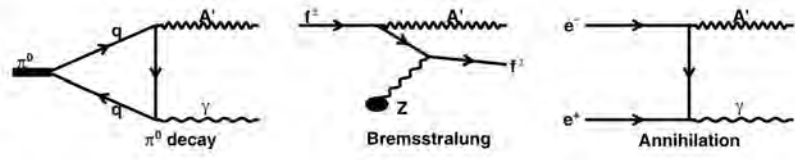


Figure 2.3. Illustration of the different DP production mechanisms. Starting from the left Dark Photon production in meson decays, in lepton-on-target experiments, and in annihilation experiments. These scenarios are derived from experiments [63].

In *meson decays* (Fig. 2.3 left) the DP can be produced in the decays of the charged and neutral pseudoscalar (P) and vector (V) mesons in the processes where a photon is emitted:

$$\begin{cases} \pi^0, \eta \rightarrow \gamma A' \\ V^\pm \rightarrow \pi^\pm A' \\ P^\pm \rightarrow \pi^\pm A' \end{cases} \quad (2.14)$$

The last process is possible only if the DP is massive and the decay rate is proportional to $m_{A'}^2$. The BR of the vector mesons can be extracted from the corresponding SM decay mode with a photon in the final state.

Another production mechanism is through *A' - strahlung* in *lepton-on-target experiments* (Fig. 2.3 middle). This process is very similar to SM Bremsstrahlung with the ordinary photon mixing to an A' . Using the Weizsäcker-Williams approximation [64], it is possible to calculate the production rate of this mechanism. Calling E_0 the energy of an incident electron and $E_{A'} = xE_0$ the energy of an emitted DP, the differential cross section can be calculated as follows:

$$\frac{d\sigma}{dx d\cos\theta_{A'}} \approx \frac{8Z^2\alpha_{QED}^3\epsilon^2 E_0^2 x}{U^2} \frac{\chi}{Z^2} \times \left[(1-x+x^2/2) - \frac{x(1-x)m_{A'}^2 E_0^2 x \theta_{A'}^2}{U^2} \right] \quad (2.15)$$

where $\theta_{A'}$ is the emission angle of A' with respect to the beam electron, Z is the atomic number of the target material,

$$U = U(x, \theta_{A'}) = E_0^2 x \theta_{A'}^2 + m_{A'}^2 \frac{(1-x)}{x} + m_e^2 x \quad (2.16)$$

and for given nuclei

$$\chi = \chi(E_0, m_{A'}) = \int_{t_{min}}^{t_{max}} dt \frac{t - t_{min}}{t^2} G_2(t) \quad (2.17)$$

where $t_{min} = (m_{A'}^2/2E_0)^2$, $t_{max} = m_{A'}^2$ and $G_2(t)$ is a general electric form factor [64]. This widely used approximate formula may lead to an overestimation of up to 30% of the cross-section for low beam energies of $O(1\text{GeV})$ [65].

The DP could also be produced through the *annihilation process* with a positron beam (Fig. 2.3 right) both at fixed target or at colliders. In the limit $m_{A'} \rightarrow 0$ and $\epsilon = 1$ the cross-section is two times the ordinary two-photon annihilation:

$$\sigma(e^+e^- \rightarrow \gamma A') = 2\epsilon^2 \sigma(e^+e^- \rightarrow \gamma\gamma) \quad (2.18)$$

If $m_{A'}$ cannot be neglected with respect to the center of mass energy \sqrt{s} , the differential cross-section can be obtained, neglecting the electron mass m_e , using the following formula from [66]

$$\frac{d\sigma(e^+e^- \rightarrow \gamma A')}{d\cos\theta} = \frac{\alpha\epsilon^2}{2s^2(s - m_{A'}^2)} \left(\frac{s^2 + m_{A'}^4}{\sin^2\theta} - \frac{(s - m_{A'}^2)^2}{2} \right) \quad (2.19)$$

which reduces to the equation 2.18 for $s \gg m_{A'}^2$, as visible in Fig. 2.4 [67].

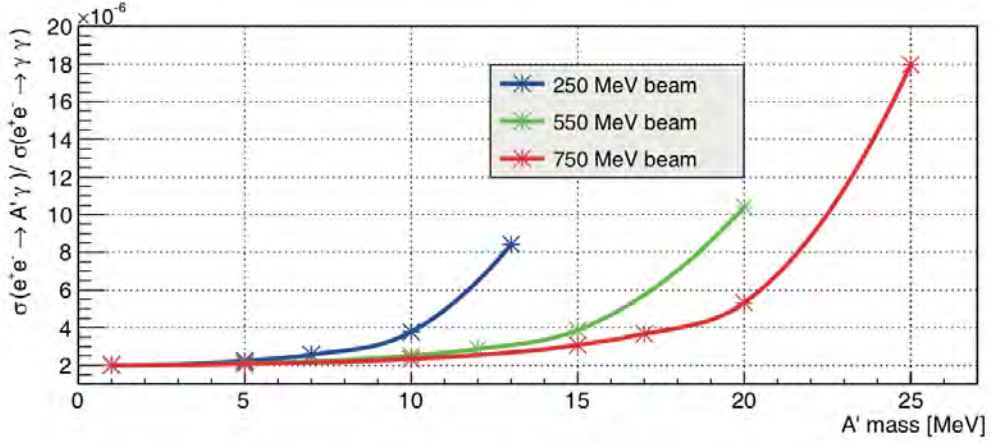


Figure 2.4. Ratio of the cross-sections of the processes $e^+e^- \rightarrow \gamma A'$ and $e^+e^- \rightarrow \gamma\gamma$ in positron-on-target annihilation, for $\epsilon = 10^{-3}$ and different e^+ beam energies.

This method could be an important processing tool for low-mass DPs as it allows the reconstruction of the complete event kinematics, providing a way to check long-living or invisibly decaying DPs.

A completely different way of producing the DP is through *hadron beams*. The differential cross-section for A' production through proton bremsstrahlung has been calculated in the Weizsächer-Williams approximation [68]. Translating this into differential event rate per proton interaction with nucleus A , the following formula is obtained:

$$\frac{dN}{dz dp_{\perp}^2} = \frac{\sigma_{pA}(s')}{\sigma_{pA}(s)} \omega(z, p_{\perp}^2) \quad (2.20)$$

where z is the fraction of the proton momentum carried by A' , p_{\perp} is the transverse component of the A' momentum, $s' = 2M(E_p - E_{A'})$ is the reduced centre-of-mass energy after A' emission, and $s = 2ME_p$, and

$$\begin{aligned} \omega(z, p_{\perp}^2) = \frac{\epsilon^2 \alpha}{2\pi} \left\{ \frac{1 + (1-z)^2}{z} - 2z(1-z) \left[\frac{2M^2 + m_{A'}^2}{H} - z^2 \frac{2M^4}{H^2} \right] \right. \\ \left. + 2z(1-z)[1 + (1-z)^2] \frac{M^2 m_{A'}^2}{H^2} + 2z(1-z)^2 \frac{m_{A'}^4}{H^2} \right\} \frac{1}{H} \quad (2.21) \end{aligned}$$

where

$$H(p_{\perp}^2, z) = p_{\perp}^2 + (1-z)m_{A'}^2 + z^2 M^2 \quad (2.22)$$

The hadron cross-section σ_{pA} is dependent on atomic number. The Eq. 2.22 is valid under certain approximations, one of which is that the proton is a structureless particle. In high momentum transfer interactions the quark content becomes important and there is also the possibility for quark bremsstrahlung. If a proton form

factor is included, the quark contribution is underestimated but such approximation is often used to obtain conservative limits on the DP production rate.

2.7 Dark Photon decays

Depending its mass and on the hypothesis on the structure of the Dark Sector the decay modes of the Dark Photon may change significantly. If the scenario considered doesn't include particles in the Dark Sector with masses smaller than the Dark Photon mass, the A' is forced to decay in "visible" particles. For this reason its width is suppressed by the ϵ^2 factor, and the A' it's generally a long lived particle for small value of the mixing parameter. The BRs of A' decaying in SM particles as a function of its mass, are shown in Fig. 2.5.

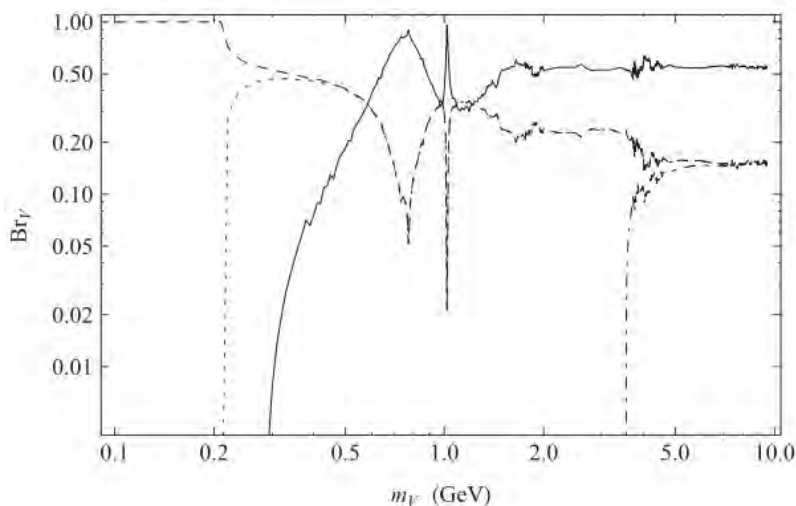


Figure 2.5. Dark photons visible decay BRs for different masses: $A' \rightarrow e^+e^-$ (dashed), $A' \rightarrow \mu^+\mu^-$ (dotted), $A' \rightarrow \tau^+\tau^-$ (dotted-dashed) and $A' \rightarrow hadrons$.

If the mass of the DP is greater than twice the mass of a pair of leptons, $m_{A'} > 2m_l$, it will decay into a pair of l^+l^- with the following width:

$$\Gamma_{A' \rightarrow l^+l^-} = \frac{1}{3} \alpha \epsilon^2 m_{A'} \sqrt{1 - \frac{4m_l^2}{m_{A'}^2}} \left(1 + \frac{2m_l^2}{m_{A'}^2} \right) \quad (2.23)$$

while if the DP mass is large enough and a coupling between the A' and quarks exists, the A' would also have hadronic decays with the following width:

$$\Gamma_{A' \rightarrow had} = \frac{1}{3} \alpha \epsilon^2 m_{A'} \sqrt{1 - \frac{4m_\mu^2}{m_{A'}^2}} \left(1 + \frac{2m_\mu^2}{m_{A'}^2} \right) \times \frac{\Gamma(e^+e^- \rightarrow hadrons)}{\Gamma(e^+e^- \rightarrow \mu^+\mu^-)} (E = m_{A'}) \quad (2.24)$$

An extension of Kinetic Mixing model is the *Non-Minimal Kinetic Mixing*. Here the DP can couple with charged particles under the $U_D(1)$ gauge group. Since nothing prohibits the dark particles to be light, they can populate an extended mass

region down to zero. In its simplest form, the interaction term of a dark fermion, χ , with A' would be similar to QED and have the following form:

$$\mathcal{L}_D \sim \sqrt{4\pi\alpha_D}\bar{\chi}\gamma^\mu\chi A'_\mu \quad (2.25)$$

where α_D is the coupling constant associated with the $U_D(1)$ gauge group in the dark sector. If the mass of the dark fermions is less than half the mass of the DP, $m_\chi < 1/2m_{A'}$, then the A' will decay dominantly into a pair $\chi\bar{\chi}$ with the following width of decay:

$$\Gamma_{A' \rightarrow \chi\bar{\chi}} = \frac{1}{3}\alpha_D m_{A'} \sqrt{1 - \frac{4m_\chi^2}{m_{A'}^2}} \left(1 + \frac{2m_\chi^2}{m_{A'}^2}\right) \quad (2.26)$$

In this scenario the A' has a prompt decay, being its width not suppressed by the ϵ^2 factor, and its decay product are undetectable by most of the experiments. For this reason decays to dark fermions are commonly referred as DP “invisible” decays.

Summarising, depending on the existing mass hierarchy in the invisible sector, all the physics of the model can be divided into the following scenarios: if $m_\chi > m_{A'}/2$ the DP decays into SM particles with a decay rate directly proportional to ϵ^2 . In particular, if $m_{A'} < 2m_\mu$, the only possible final state is a pair of e^+e^- . An interesting possibility appears when $\alpha_D \gg \alpha\epsilon^2$. The dominant decay, which is not suppressed by the factor ϵ , will be $A' \rightarrow \chi\bar{\chi}$.

2.8 Dark Photon experimental searches

The massive DP models are very predictive and are therefore very rich in the related phenomenology. This characteristic trigger a large number of experimental studies using very different techniques in combination with the analysis of data samples from last decade’s flavour physics experiments (BABAR, NA48, KLOE). The main activity in the search for the DP is currently focused in the United States, in particular at the Jefferson Laboratory, but Europe is also populated by new initiatives. Generally, the biggest uncertainty in the interpretation of the experimental results is related to the existence or not of new light states χ , charged under $U_D(1)$. These would open additional channels of dark decay that would alter the panorama of exclusions. For this purpose, exclusion limits must be carefully interpreted comparing the underlying hypotheses in order to avoid ambiguity. In this section the available experimental constraints will be briefly examined, explaining the different approaches. A subdivision into two major categories is possible: “visible” or “invisible” decay search, based on the decay modes of the DP that indicate whether a light dark matter states χ is present or not. Visible modes of decay are less general, even if more studied, because there is no a priori reason to assume that the DP is the lightest state in the DS.

2.8.1 Visible decay search techniques

The studies devoted to visible decay searches are based on the assumption that the DP is the DS’s lightest state and therefore can only decay into SM particles. For DP mass $M_{A'} < 2m_\mu$ the only allowed decay mode is the electron-positron pair. For DP

mass above the two muon threshold ($M_{A'} > 2m_\mu$) the decay into muon pairs is also allowed, while for $M_{A'} > 2m_\pi$ the DP can decay into hadrons as well. Regardless of its mass the dark photon always has a significant decay fraction into lepton pairs.

Recently there has been a lot of experimental activity. The data mining technique in data samples already collected in the past and the results from dedicated experiments allowed to exclude the $g_\mu - 2$ favoured parameter region completely in the hypothesis that DP decays into SM particles. All of the measurements shown in Fig. 2.6 can be categorised into different groups of experiment according to the methodology used: dump experiments, fixed-target experiments, meson decay experiments, collider experiments.

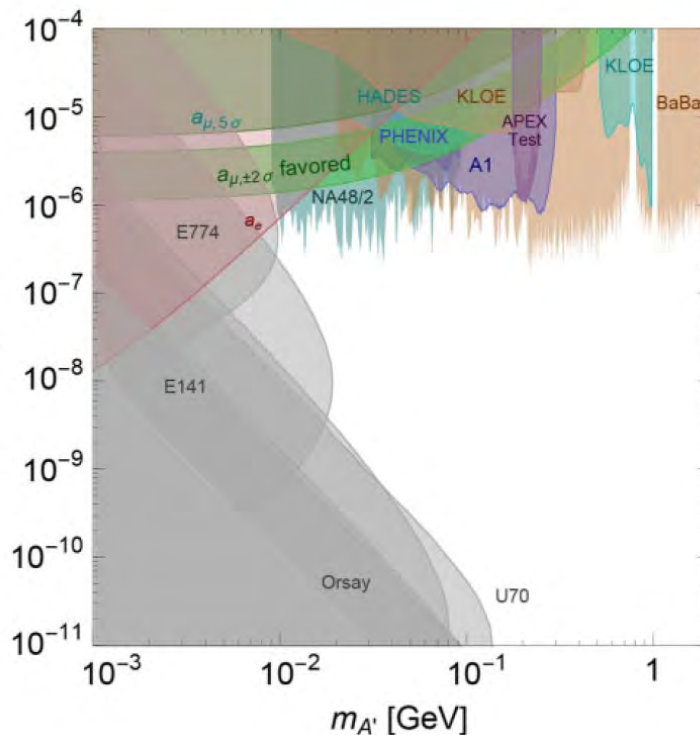


Figure 2.6. Constraints in ϵ^2 versus $M_{A'}$ plane for DPs that decay directly to SM particles. Figure adapted from [69].

A high-intensity beam dumped on a thick fixed target in beam dump experiments provides the high luminosity needed to test the DP's weak couplings. Incoming electron or proton beam of energy E_0 scatters on the target and produces dark photons A' with energy $E_{A'}$, usually through $A' - \text{strahlung}$. If the DP decays to e^+e^- or $\mu^+\mu^-$ they can be detected behind a sufficiently long shield. All SM particles are absorbed by a combination of a target and a shield that only allows the survival of neutral long living and weakly interacting states. Any sign of a di-lepton decay behind the shield, which is not consistent with the predicted background, suggests NP particles are present.

Fixed-target experiments using high-current electron beams are an excellent place to search for A' 's with masses in the GeV range. In JLab and MAMI, already existing spectrometers were used to look for resonance in the invariant-mass spectrum of pairs

formed by electron-on-target collisions of e^+e^- . Examples of early dedicated efforts to limit the DP parameter space are test runs on the APEX and HPS at JLab and A1 at MAMI. The observed physical process is the scattering of an electron beam on a fixed target that causes a DP's bremsstrahlung emission, subsequently decaying into a pair of SM leptons. The decay particles are observed and their invariant mass is measured, allowing to look for a bump in the invariant mass spectrum due to the hidden gauge boson. The A' will manifest itself by a very sharp peak, while the radiative background resulting from the corresponding QED process is described by a smooth distribution. Recently HPS experiment tried to detect DP by using displaced vertex technique but the sensitivity is currently not very good.

The DP can be produced in the kinetic mixing scenario in most of meson decays where photons are emitted. For this reason, by using the huge data samples collected by the flavour factories (KLOE, NA48), strong limits can be set in the DP parameter space. Many meson decay results populate the $\epsilon > 10^{-4}$ area for a wide range of masses in Fig. 2.6. Due to the lack of statistics and the increased DP lifetime, it is difficult to access the region below 10^{-4} with this technique.

Using the annihilation production DP accessible also at e^+e^- colliders and fixed target positron based experiments. Colliders experiments, BaBar KLOE and BESIII, performed searches for A' in the process $e^+e^- \rightarrow \gamma A' A' \rightarrow e^+e^-, \mu^+\mu^-$. This searches produced constraints in the region $\epsilon > 10^{-4}$ and are limited by background QED background arising from radiative Bhabha scattering and two gamma annihilation process.

2.8.2 Invisible decay search techniques

Searches for invisible decays are based on the hypothesis that in the dark sector there is at least one new particle χ of mass below $m_{A'}/2$. The dark photon will mainly decay to non-SM states under this very general assumption, escaping from detection in past experiments. Therefore, all branching ratios of A' into standard model particles are suppressed by a factor ϵ^2 , which significantly reduces the effectiveness of visible decay searches. As a result, as shown in Fig. 2.7 and Fig. 2.8, the parameter space for invisible decays is much less constrained by direct searches.

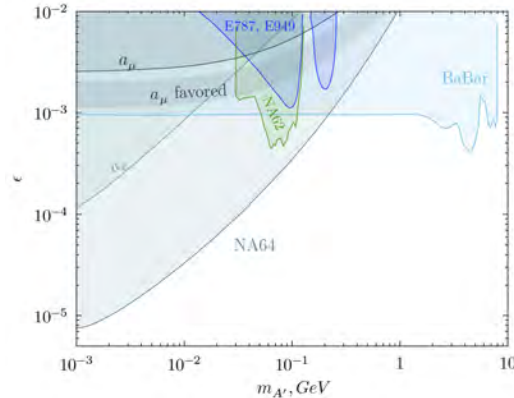


Figure 2.7. Exclusion limits for $A' \rightarrow \chi\bar{\chi}$ from DP invisible decay searches.

To detect the dark photon in this case, there are several experimental methods

suggested so far. One possibility in use both at colliders by BaBar and Belle II and at fixed target by the PADME experiment is to use the process $e^+e^- \rightarrow \gamma A'$ $A' \rightarrow \chi\bar{\chi}$. Measuring the 4-Momentum of the recoil SM single photon the missing mass can be calculated. If the partner particle emitted with the measured photon is a dark photon, the missing mass spectrum should show a peak corresponding to the A' mass. This is the unique technique sensitive to the mass of the A' .

Another possibility is to advocate energy conservation principle. If an invisible particle is produced in the interaction of the beam with a thin or thick target the conservation of visible energy will be strongly violated. Two different possibilities have been explored so far. Missing energy experiments, like NA64 at CERN, use the measurement of the energy of the beam by means of an electromagnetic calorimeter. If the measured energy is $<50\%$ of the beam energy a new particle should have been produced. Similar approach with better sensitivity proposed to measure the momentum of a particle before and after its interaction with a thin target. If an A' is radiated during the interaction the momentum should be strongly reduced. This approach is currently investigated by the LDMX collaboration at SLAC.

A direct way of searching for invisible A' is to detect the χ DM particles, obtained in the decay of the DP, produced in the dump by $A' - \text{strahlung}$, by their scattering in a large detector downstream. The dark states could scatter on the ordinary matter electrons or nuclei through the mixing, with a cross-section given by the following formula:

$$\frac{d\sigma(e\chi \rightarrow e\chi)}{dE_f} = \frac{\alpha_D \epsilon^2}{\alpha} \times \frac{8\pi \alpha^2 m_e (1 - E_f/E)}{(m_{A'}^2 + 2m_e E_f)^2} \quad (2.27)$$

where E_f is the electron recoil energy. In this regime, the χ production is proportional to $\epsilon^2/m_{A'}^2$. The χ -nucleon scattering in the detector occurs with a rate proportional to $\alpha_D \epsilon^2/2m_{A'}^2$ over most of the mass range. The combination of the two steps lead to a suppression factor $\epsilon^4 \alpha_D/m_{A'}^4$ for, and therefore a very large number of primary particles are necessary.

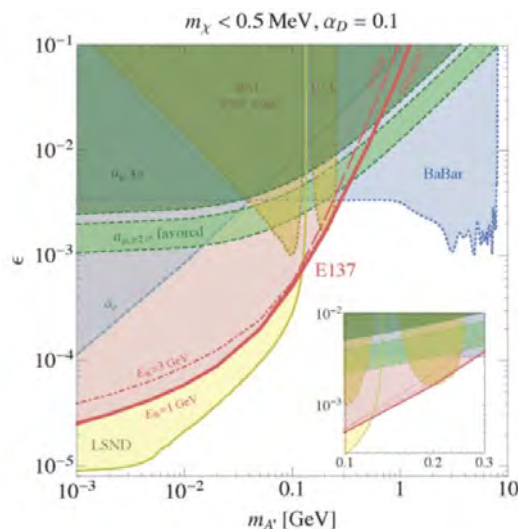


Figure 2.8. Exclusion limits for $A' \rightarrow \chi\bar{\chi}$ through DM scattering process.

Being described by different models involving different numbers of free param-

ters, the exclusions obtained with the two different techniques can not be directly compared. For this reason they are represented in two different diagrams in Fig. 2.7 and Fig. 2.8. Indirect limits coming from $(g_\mu - 2)$, $(g_e - 2)$, and kaon decays are common to the two scenarios.

2.9 Dark Higgs

In this section, we will investigate the signatures of an extension of the SM where the A' mass is not generated by the Stüeckelberg mechanism. This minimal model assumes the existence of the elementary boson which spontaneously breaks the $U_D(1)$ symmetry, referred as Dark Higgs (DH), indicated with h' [70]. In models where the DP mass is generated through spontaneous symmetry breaking, an associate production of the DH and DP is possible. Naturalness requires that the two particles have masses of the same order $m_{h'} \sim m_{A'}$. This new sector is not charged under the SM and vice versa, and all interactions with the SM proceed through kinetic mixing of $U_D(1)$ with the photon. The Lagrangian then take the form:

$$\mathcal{L} = -\frac{1}{4}A'_{\mu\nu}{}^2 - \frac{\kappa}{2}A'_{\mu\nu}F^{\mu\nu} + |D_{mu}\phi|^2 - V(\phi) \quad (2.28)$$

where $F_{\mu\nu}$ is the photon field strength, and the covariant derivative is $D_\mu = \partial_\mu + ie'A'_\mu$ with $U_D(1)$ charge e' . The Higgs potential is assumed to be of a form that spontaneously breaks the $U_D(1)$ symmetry.

If the SM is extended to include a hidden real scalar field h' , the most general scalar Lagrangian become:

$$\mathcal{L} = \mu_H^2|H|^2 - \frac{1}{4}\lambda_H|H|^4 + \mu'^2h'^2 - \mu_3h'^3 - \frac{1}{4}\lambda'h'^4 - \mu'_{12}h'|H|^2 - \epsilon h'^2|H|^2 \quad (2.29)$$

where H is the SM electroweak Higgs doublet and the last term is the Higgs portal quartic scalar interaction. From this theory, to get particles with properties it is necessary to minimise the scalar potential and diagonalise the mass terms. As a result SM-like Higgs particle h and a DH boson h' are obtained.

The Lagrangian written above can be parameterised and rewritten as follows:

$$\mathcal{L} = -m_{h'}^2h'^2 - \sin\theta\frac{m_f}{v}h'\bar{f}f - \lambda vhh'h' + \dots \quad (2.30)$$

where m_ϕ is the DH boson mass, θ the mixing angle and λ the trilinear coupling. These independent parameters determine all of the phenomenological properties of the DH. The omitted terms include additional cubic and quartic scalar interactions involving h' and h .

2.10 Dark Higgs production

The h' – *strahlung* process is one of the few h' production processes with an amplitude that is suppressed by a single power of the kinetic mixing angle and can therefore easily occur in $\epsilon \sim O(10^{-2} - 10^{-3})$. This process of creation is similar

to traditional Higgs-strahlung in the SM, but in this case the h' is produced in association with a A' instead of a SM photon. While the vector A' will typically have a large branching ratio to lepton pairs, the decays of the h' will depend on its mass relative to that of the vector. If the Dark Higgs is heavy it will decay in two vectors A' , eventually leading to a six lepton final state. On the contrary, if the DH is light, it will decay via loop processes to leptons and possibly hadrons. In this case DH is long-lived and will most likely become an undetected particle. The h' – *strahlung*, $e^+e^- \rightarrow A'h'$, just like the pair annihilation $e^+e^- \rightarrow A'\gamma$, is minimally suppressed by the factor ϵ^2 . The total cross section for this process is:

$$\begin{aligned} \sigma_{e^+e^- \rightarrow A'h'} &= \frac{\pi\alpha\alpha'\epsilon^2}{3s} \left(1 - \frac{m_V^2}{s}\right)^{-2} \sqrt{\lambda\left(1, \frac{m_{h'}^2}{s}, \frac{m_V^2}{s}\right)} \\ &\quad \times \left[\lambda\left(1, \frac{m_{h'}^2}{s}, \frac{m_V^2}{s}\right) + \frac{12m_V^2}{s} \right] \\ &\approx 20 \text{ fb} \times \left(\frac{\alpha'}{\alpha}\right) \left(\frac{\epsilon^2}{10^{-4}}\right) \frac{(10 \text{ GeV})^2}{s} \quad (2.31) \end{aligned}$$

where in the last line has assumed the scaling regime $m_{h'} + m_{A'} < \sqrt{s}$ GeV, which is appropriate for WIMP models with a GeV-scale mediator. For reasonable values of the kinetic mixing parameter, the cross section is quite large. Note that there is the chance of an s-channel enhancement in the cross section if $m_{A'} \sim \sqrt{s}$. The Higgs'–strahlung production process can produce qualitatively distinct signals depending on the relative mass of A' and h' , as can be inferred from the branching fractions shown in Figs. 2.5 and 2.9.

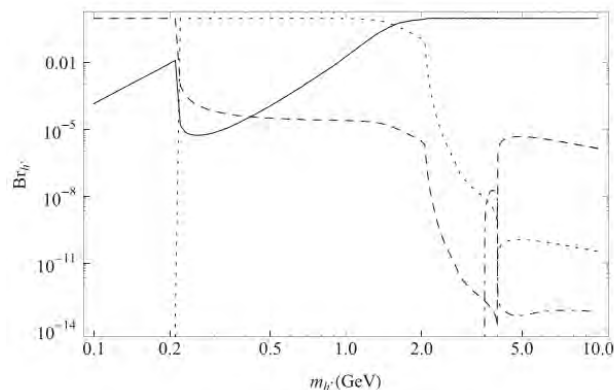


Figure 2.9. Branching Ratios for h' for the case $m_{A'} = 2$ GeV: $h' \rightarrow e^+e^-$ (dashed), $h' \rightarrow \mu^+\mu^-$ (dotted), $h' \rightarrow \tau^+\tau^-$ (dotted-dashed) and $A' \rightarrow A'A'$ (solid) for the choice of $\epsilon = 10^{-2}$ and $\alpha' = \alpha$.

2.11 Dark Higgs decays

For the case $m_{h'} > m_{A'}$ the h' decays almost exclusively to two A' as illustrated by the continuous line in Fig. 2.9 where a mass of 2 GeV is assumed for the A' .

Since at small masses the vectors A' have a sizeable branching fraction to leptons, this will lead to a signature of six leptons. For $m_{h'} > 2m_{A'}$ three pairs of leptons will have an invariant mass peaked very narrowly around the mass of the vector, $m_{l+l-} \approx m_{A'}$, reflecting an underlying decay $h' \rightarrow A'A'$ to on-shell vectors. For $2m_{A'} > m_{h'} > m_{A'}$, the underlying decay is $h' \rightarrow A'A'^*$ and therefore two lepton pairs will have $m_{l+l-} \approx m_{A'}$. In addition, the four leptons will have a combined invariant mass of $m_{2(l+l-)} \approx m_{h'}$. If the vector is light, $m_{A'} < 2m_\mu$, it can only decay to an e^+e^- pair, and thus every final state will consist of 3 e^+e^- pairs.

The h' decay characteristics depend on whether it's heavier or lighter than the A' vector. Let's consider $m_{h'} > 2m_{A'}$ first, in which case the h' mainly decays to a pair of real vectors, with partial width

$$\Gamma_{h' \rightarrow A'A'} = \frac{\alpha' m_{h'}^3}{8m_{A'}^2} \sqrt{1 - \frac{4m_{A'}^2}{m_{h'}^2}} \left(1 - \frac{4m_{A'}^2}{m_{h'}^2} + \frac{12m_{A'}^4}{m_{h'}^4} \right) \quad (2.32)$$

where $\alpha' = e'^2/4\pi$.

If h' is lighter than the A' , loop-induced decays become important. For example, the DH will decay through a triangle graph into a pair of leptons

$$\Gamma_{h' \rightarrow f\bar{f}} = \frac{\alpha' \alpha^2 \epsilon^4 m_{h'}}{2\pi^2} \frac{m_f^2}{m_{A'}^2} \left(1 - \frac{4m_f^2}{m_{h'}^2} \right)^{3/2} |I(m_{h'}, m_{A'}, m_f)|^2 \quad (2.33)$$

Heavy DH bosons are expected to decay exclusively to vectors, as this is the only direct decay mode, with no ϵ factor suppression. In turn, these vectors will decay to leptons or hadrons. However, light Higgs bosons with $m_{h'} < m_{A'}$ will decay primarily through a loop-induced process, with a rate proportional to $\epsilon^4 \times (\text{loopfactor})^2$. Although this is quite small, it still generally overwhelms the suppression given by the four-body phase space in the process $h' \rightarrow A'^*A'^* \rightarrow 4l$. Thus, when h' is light, it is also extremely narrow and long-lived.

2.12 Dark Higgs experimental searches

The BaBar collaboration performed a search for DH boson in the Higgs'-strahlung process. The measurement was performed in the range $0.8 \text{ GeV} < m_{h'} < 10 \text{ GeV}$ and $0.25 \text{ GeV} < m_{A'} < 3 \text{ GeV}$. This research was done by reconstructing the exclusive final states $3(l^+l^-)$, $2(l^+l^-)\pi^+\pi^-$ and $l^+l^-2(\pi^+\pi^-)$ or the inclusive processes $2(\mu^+\mu^-) + X$ and $\mu^+\mu^-e^+e^- + X$, where X was any final state different from pions or leptons. The analysis for the inclusive processes was limited to $m_{A'} > 1.2 \text{ GeV}$. The lack of extra signal provided limits to the $e^+ + e^- \rightarrow A'h' \rightarrow h' \rightarrow A'A'$ cross-section which was translated into 90% C.L. upper limit on the product of the dark coupling constant and the mixing parameter $\alpha_D \epsilon^2$. The excluded region for different values of the DH boson mass is shown in Fig. 2.10.

Other searches for DH were performed by the Belle experiment where ten exclusive final states with $A' \rightarrow e^+e^-$, $\mu^+\mu^-$ or $\pi^+\pi^-$ and three inclusive final states $2e^+e^-X$, $2\mu^+\mu^-X$, and $e^+e^-\mu^+\mu^-X$ were investigated, where X is a DP detected through the missing-mass technique.

The data analysis was performed in the interval $0.1 \text{ GeV} < m_{A'} < 3.5 \text{ GeV}$ and

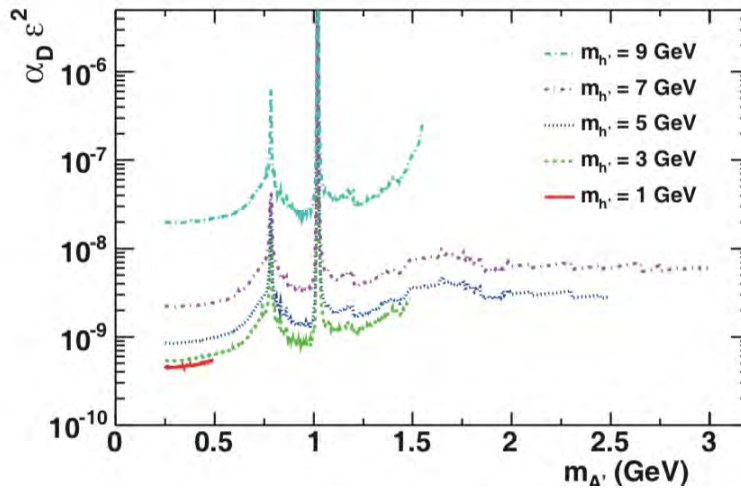


Figure 2.10. Limits on the DP parameters for different masses of the DH boson obtained from the searches for DH performed by the BaBar collaboration [72].

$0.2 \text{ GeV} < m_{h'} < 10.5 \text{ GeV}$ in the exclusive searches and $1.1 \text{ GeV} < m_{A'} < 3.5 \text{ GeV}$ and $2.2 \text{ GeV} < m_{h'} < 10.5 \text{ GeV}$ in the inclusive scenario. No significant signal above the expected SM background was observed allowing to set limits in the parameters of the DS, as shown in Fig. 2.11.

Lastly, also KLOE-2 collaboration searched for h' -strahlung process in the $e^+e^- \rightarrow A'h'$ process. The assumption that h' is lighter than A' was made, leading to a final state where only the A' decay products are seen and the events have missing energy signature, since the lifetime of the DH boson would be so large that it would escape detection. This is the invisible DH scenario.

This study was performed with two samples of the $e^+ + e^-$ energy: 1.65 fb^{-1} , at the ϕ peak at 1019 MeV (on-peak data) and 0.206 fb^{-1} at energy of 1000 MeV (off-peak sample). The $\mu^+\mu^-$ decay channel of the DP was studied limiting the sensitivity to $m_{A'} > 210 \text{ MeV}$ with an absolute missing value of the momentum more than 40 MeV .

No excess of events providing evidence for the DH-strahlung process was found. The results were converted in terms of $\alpha_D \epsilon^2$ and are shown in Figs. 2.12.

At present none of the previous exclusion has ever probed the region of mass of the h' lower than 1 GeV using decays to leptons. This justify the attempt of understanding the PADME sensitivity to Dark Higgs decays to 6 leptons.

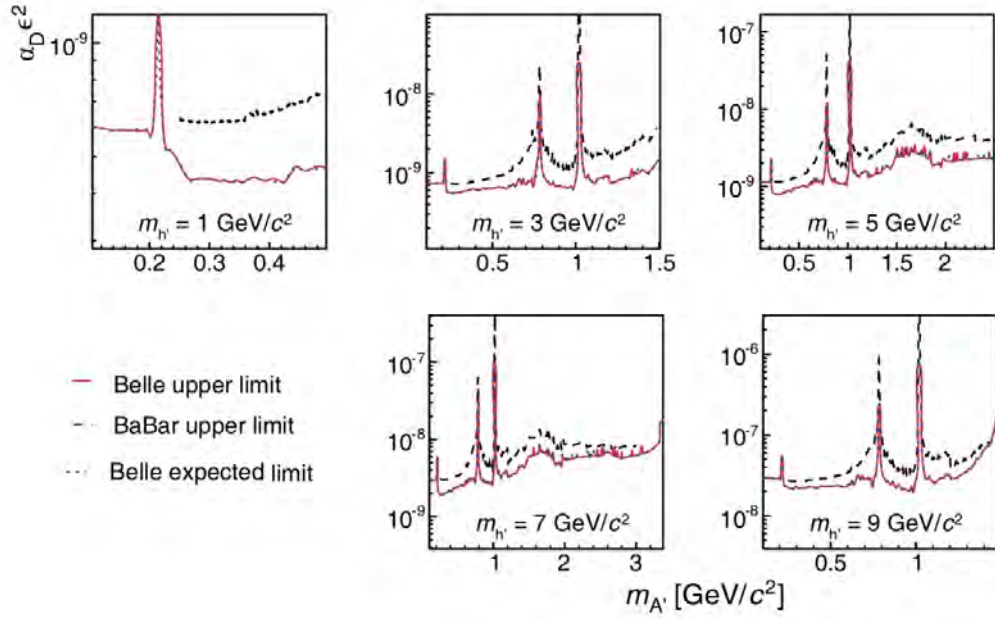


Figure 2.11. Excluded regions in the $\alpha_D - m_{A'}$ parameter space for different masses of the DH boson [73].

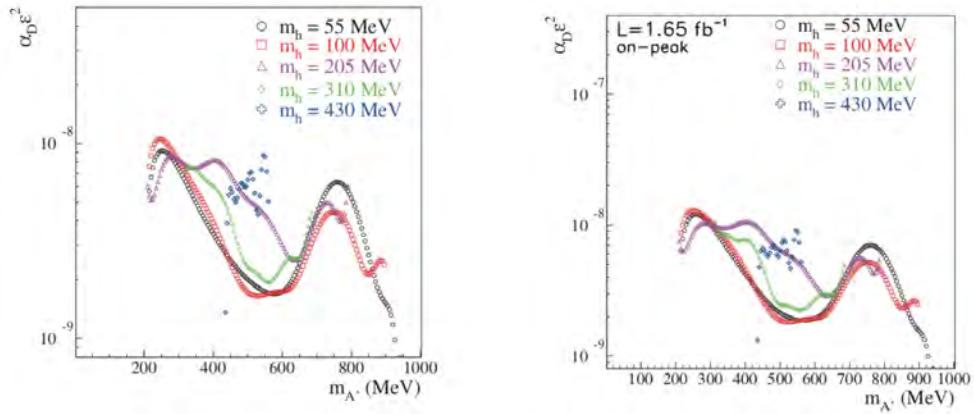


Figure 2.12. On the left excluded region at 90% C.L. with the KLOE-2, coming from the on-peak data sample (C.M. energy is 1019 MeV) [74] while on the right KLOE-2 exclusion limits at 90% C.L., coming from the off-peak sample (C. M. energy is 1000 MeV) [74].

Chapter 3

The PADME experiment at the Laboratori Nazionali di Frascati

As explained in the previous chapter, the searches for the Dark Photon are based on different techniques: experiments with beam dumps, fixed-target experiments, search in meson decays, and searches at colliders. Based on the final state that the experiment set out to probe, the study can be divided into “visible” and “invisible” searches. The two types of research are complementary and equally important. Towards the end of 2015, INFN formally approved a new experiment searching for the dark photon in the invisible channel, PADME (Positron Annihilation into Dark Matter Experiment) at the DAΦNE Linac in Frascati. The experiment aims to produce dark photons through annihilation of the positrons of the incident beam with the electrons of a thin target. The PADME collaboration performed the first data taking in 2018 - 2019. The experiment goal is to collect around 10^{13} positrons on the target, thus reaching a sensitivity on the constant of coupling $\epsilon \sim 10^{-3}$ and on the mass of $m_{A'} \sim 23.7\text{MeV}/c$. In this chapter, after a brief introduction of the DAΦNE Beam-Test Facility and the ways to search DM with Linac, the PADME detectors, trigger, DAQ and its Geant4 simulation will be presented.

3.1 Frascati linac test facility

The INFN Frascati Laboratory’s DAΦNE complex (LNF) was constructed in the early 1990s with the main purpose of carrying on high statistical experiments with Kaons, created abundantly by the decay of the Φ meson [75]. The cross-section of e^+e^- has a narrow peak at the meson mass of $1020\text{MeV}/c^2$, so the collider is often called a “ Φ -factory”. The complex has been completed in 1996 and has been running with stable collisions for experiments since 1999, mainly with KLOE (and its upgraded version KLOE2) [76].

The high current LINAC accelerates up to 510 MeV of electrons and positrons, which are then stacked and collected in a damping ring before being pumped into the two separate main rings for emission reduction. One of the two collision points is typically used for experiments (the KLOE since 2007), whereas the beams are divided in the opposite. The general layout of the complex is schematically shown in 3.1.

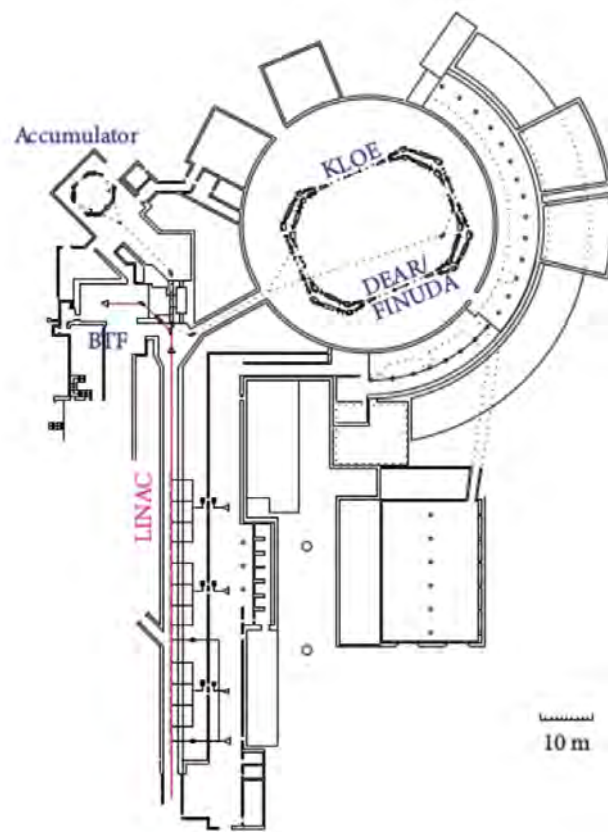


Figure 3.1. DAΦNE complex at the national laboratories of Frascati of the INFN.

Until injection into the damping ring, the electron or positron beam can be transferred to a dedicated transfer line where a device consisting of a target plus a dipole and collimating slits will attenuate and select the momentum of narrow ($< 1\%$) secondary particles. Therefore, the secondary beam is guided to a different experimental hall for beam-testing activities (Beam-Testing Facility, BTF) [77]. The BTF was constructed as part of the DAΦNE complex [78] it consists of a transfer line powered by a dipole magnet that enables electrons or positrons, normally injected into the damping ring, to be redirected from the high-intensity LINAC to a dedicated experimental area. Based on the option of one of the following two key operating modes, the facility can provide runtime tuneable electron and positron beams in a given range of different parameters:

- *Single particle regime:* in this operation mode a Copper target step allowing the selection of three different radiation lengths (1.7, 2 or $2.3 X_0$) is inserted into the initial portion of the BTF line to redirect the beam. It creates a secondary beam with a continuous full-span energy (from LINAC energy to a few MeV) and strength, down to a regime where the multiplicity of particles per bunch follows a Poisson distribution;
- *High-intensity beam extraction:* the LINAC beam is directly controlled in the BTF hall with a fixed energy (i.e. the final LINAC) and a reduced multiplicity selection range (typically from 10^{10} down to 10^4 particles per bunch) is obtained by collimating tungsten slits.

The dipole magnet, which steers the beam away from the main transfer line from the LINAC end to the accumulator ring, also has the task of reselecting secondary particles from the BTF target in single particle mode, with the momentum band identified by a downstream horizontal collimator (made of a pair of tungsten slits). The collimator before the beam attenuating target, the target itself and the second collimator, limiting the angular acceptance at the entrance of the bending magnet, were sitting on the same transfer line used for the injections for DAΦNE, so that this configuration had an impact on both the DAΦNE injection efficiency and BTF duty factor, due to at least two important limiting factors:

- the time needed for switching on and off, at the beginning and at the end of each injection, the large, static dipole DHSTB01;
- the time needed for the insertion and removal from the beam line of the attenuating Copper target.

In addition to the not negligible dead-time introduced by those operations at each injection, another very important point was that with this operation sequence none among the target, collimators and magnetic configurations was kept from one BTF beam period (of a few minutes) to the following one, thus making the reproducibility very poor.

Fig. 3.2 shows the original layout of the transfer lines, with the two 45° bending magnets: the first, static, towards the BTF, the second, pulsed, towards the damping ring.



Figure 3.2. Layout of the transfer-lines from the end of the LINAC to the damping ring, with the original configuration of the line towards the Beam-Test Facility.

3.2 PADME experiment at LNF

The PADME experiment is located in the BTF experimental hall as shown in Fig. 3.3:

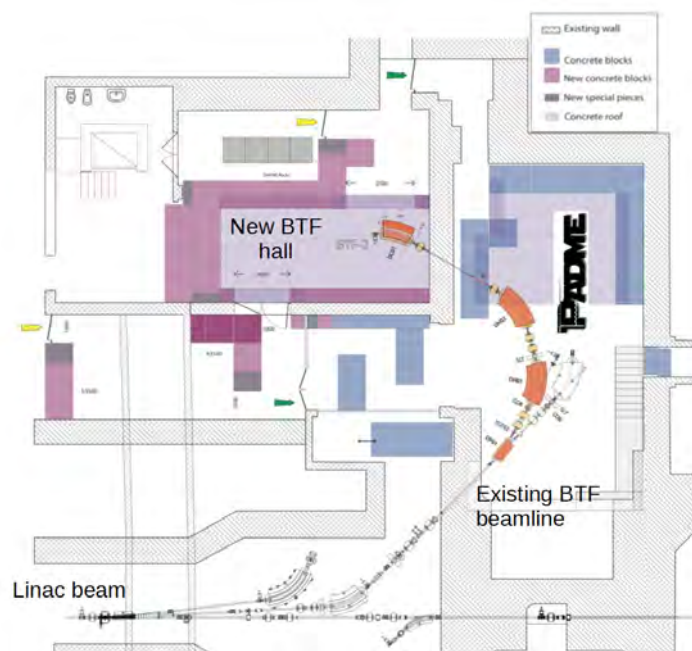


Figure 3.3. Location PADME experiment in the experimental hall of the BTF.

The accelerator for PADME must be operated to the highest possible energy. With secondary beam configuration BTF has been able to provide a 550MeV beam energy[79]. The energy spread of the positrons needs to be less than 1% and the beam divergence of the order of the milliradian for a spot of the beam of the order of the millimetre long for both axes, X and Y.

The sensitivity of PADME to the coupling parameter of the dark photon depends

crucially on the average beam bunch multiplicity and on the operating efficiency of Linac. Since the rate of the bunches cannot be increased beyond 50Hz, an attempt was made to understand how to increase the duration of the packets and the possible effects on the temporal pile-up. Up to now, it has been possible to achieve the production of a stable beam with a duration up to ~ 200 ns, to be compared with the original 40 ns[79].

3.3 Production of A' at PADME

There are two ways of producing the dark photon in the interaction of the beam of positrons and the electrons of the target: the annihilation with the electrons of the target, of the type $e^+e^- \rightarrow A'\gamma$, and the A' - *strahlung* process with the field of the atoms of the target, $e^+N \rightarrow e^+NA'$. Feynman diagrams for both of these processes are shown in 3.4 and 3.5 respectively.

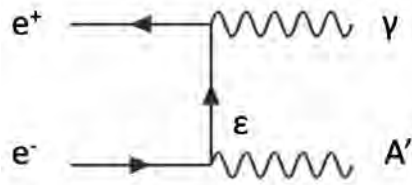


Figure 3.4. Feynman diagram of the production of A' in annihilation e^+e^- .

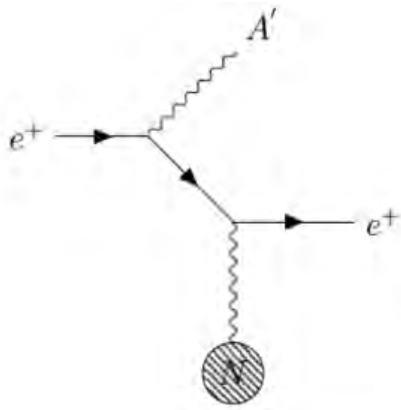


Figure 3.5. Feynman diagram of the production of A' for A' - *strahlung* of a positron with a nucleus.

Both processes are similar to those related to photon production in standard electromagnetic processes, but with a cross section scaled by ϵ^2 . For the annihilation a corrective factor due to the mass of A' has also to be introduced. The maximum energy for the Linac positron beam currently of 550 MeV allows the production of a A' boson through annihilation with a mass lower to the center of mass energy of 23.7 MeV [80]. The kinematical constraints of the initial state, are used to better reject the background events, that are dominated by the SM bremsstrahlung. The cross section of annihilation and emission of bremsstrahlung of an ordinary photon

of energy > 1 MeV, for a positron incident on a carbon target is represented in Fig. 3.6. The annihilation cross section is calculated directly with the numerical calculation by the program called CalcHEP [81] and is compared with that of the Heitler formula implemented in the program called GEANT4 [82]. It is observed that the two methods are in agreement in within 2%. The bremsstrahlung process is also shown in figure 3.6 using the cross section parameterisation implemented by GEANT4.

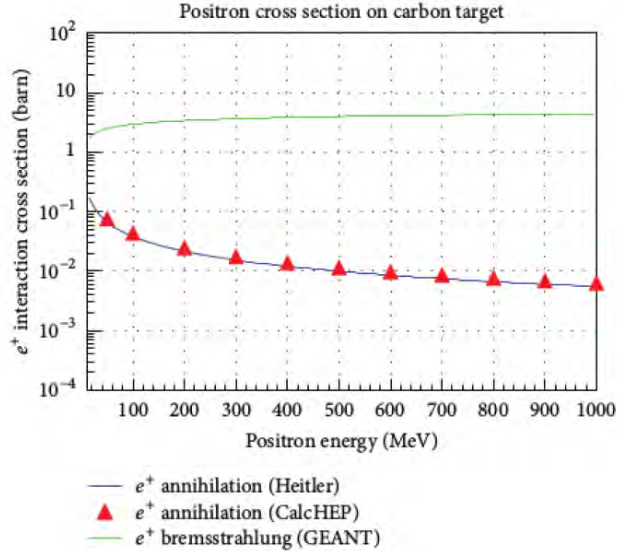


Figure 3.6. Cross section of the positron in a carbon target.

Since the ratio between annihilation and bremsstrahlung is proportional to $1/Z$, it is preferable to use a material with a low Z value in order to increase annihilation with respect to bremsstrahlung emissions. Carbon has been chosen as the material being the solid non toxic material lower Z . The annihilation/bremsstrahlung fraction for this material is $2.3 \cdot 10^{-3}$ for a positron energy of 550 MeV. For this energy the annihilation cross section with free electrons at rest is 1.5 mb and the probability that this process takes place on a carbon target with a thickness of $100 \mu m$ is equal to $1.2 \cdot 10^{-5}$. Operationally with a beam line having multiplicity equal to $10^4 - 10^5 e^+$ per bunch with a frequency of 50 bunch/s and in a year of data collection with an efficiency of 60% [80], about $10^{13} - 10^{14}$ positrons on target (POT Positron On Target) can be collected, which corresponds to about $6 \cdot 10^7 - 10^8$ annihilations per year. In an ideal 0 background experiment, an upper exclusion limit of ϵ^2 equal to $10^7 - 10^8$ can be evaluated.

An advantage of the A' production process through annihilation is the increase in the cross section as function of the A' mass, compared to the SM annihilation in two photons. This effect is shown in Fig. 3.7 for different energies of the positron beam. In Fig. 3.8 the ratio of this cross section with the one of annihilations two photons is represented. There is a clear increase of the cross section when the mass of A' approaches energy in the center of mass.

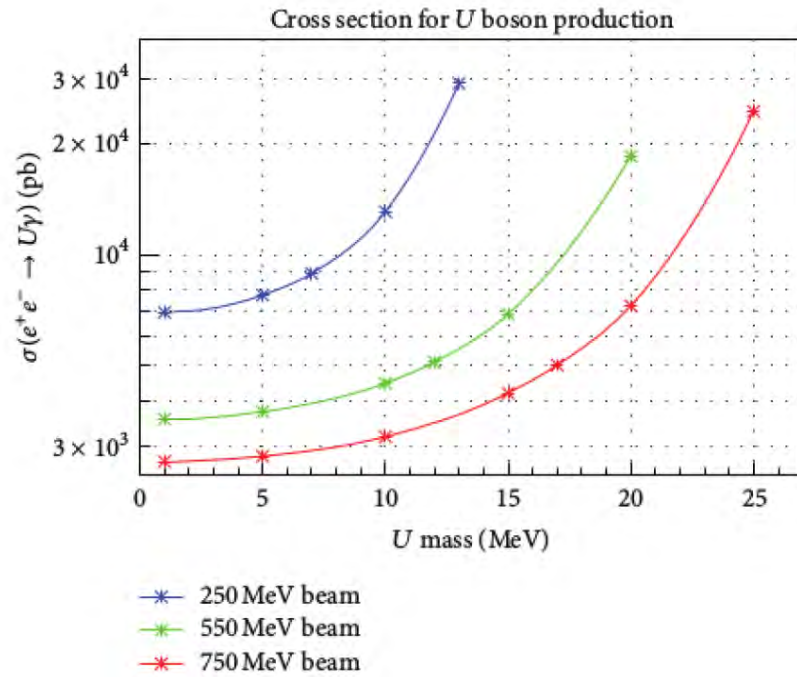


Figure 3.7. A' production cross section, for a value of $\epsilon^2 = 10^{-3}$, as a function of the mass of the boson and for different energies of the positron beam.

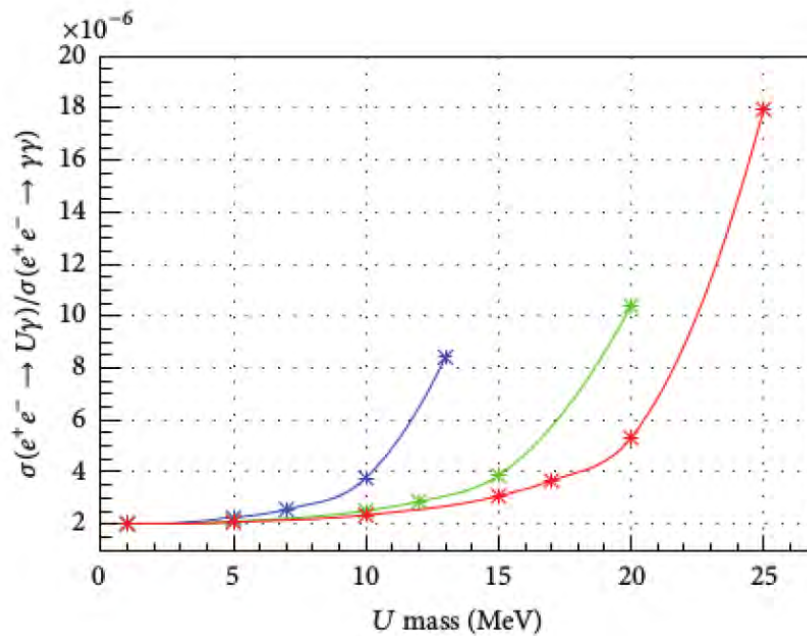


Figure 3.8. Ratio of $e^+e^- \rightarrow \gamma A'$ over $e^+e^- \rightarrow \gamma\gamma$ cross sections, for a value of $\epsilon^2 = 10^{-3}$, as a function of the mass of the boson and for different energies of the beam.

3.4 PADME physics case and general layout

The purpose of the experiment is to search for the A' boson produced by the process [83][84][85]

$$e^+e^- \rightarrow A'\gamma \quad (3.1)$$

where the positrons are interacting with the electrons of the target.

From the kinematics of the problem, a characteristic variable of the process is easily obtained:

$$M_{miss}^2 = (P_{e^-} + P_{beam} - P_\gamma)^2 \quad (3.2)$$

which can be calculated if the 4-momenta on the right are known or measurable. This distribution has a peak centred on the mass value $m_{A'}$, for the decays of the A' , and at zero, for the processes of the type $e^+e^- \rightarrow \gamma\gamma$. The described approach can be applied for both “visible” and “invisible” searches, described in the previous chapter. The detector can be divided into the following parts [80][83]:

- *active diamond target*: the active target of the experiment, also able to measure the average number of positions of the beam when it passes through the experiment;
- *charged particle Veto system*: detects and measure the momentum of the charged particles with energy lower than the beam;
- *electromagnetic calorimeter*: measures the energy and direction of photons, and acts as a veto for multi-photon final states;
- *Small Angle Calorimeter*: detects photons at a small angle to improves the rejection of bremsstrahlung events.
- *dipole magnet*: deflects the primary positrons outside the calorimeter and the charged particles with energy lower than the beam into the veto system;
- *vacuum system*: it minimises the interactions of primary and secondary particles with the air in the area between target and calorimeter;

In Fig. 3.9 the schematic layout of the experiment is shown. Starting from right the beam crosses the active target, the particles that do not interact are deflected by the magnetic field and directed towards the end of the spectrometer outside the acceptance of the calorimeter. If the beam positron is subjected to any type of interaction and loses more than 50 MeV of energy, the magnet bends it in the acceptance of the Veto system, allowing their detection. If A' is produced and decayed into e^+e^- , charged tracks would always be detected by the Veto system, which can also be used to study visible decays. Due to the very small target thickness, only 100 μm , most of the positrons in the beam do not interact. These are transported through the vacuum chamber until the end of the experiment setup and dumped of a concrete block.

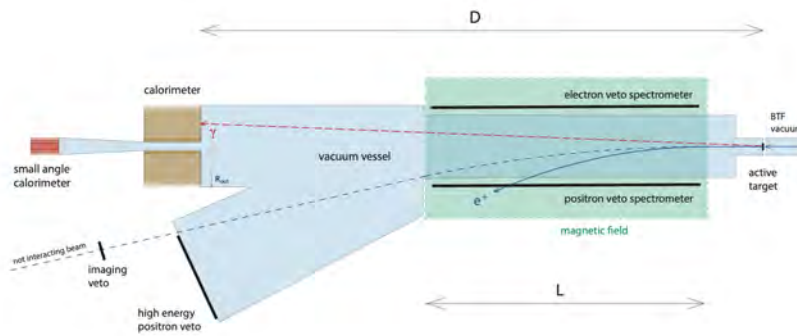


Figure 3.9. Schematic layout of PADME experiment, showing all the baseline elements

All detectors transmit their data to the data acquisition system (DAQ), whenever requested by the trigger system. The trigger and Data acquisition system (TDAQ) take care of recording the acquired data on the disks of the online PC farm. The following steps of permanently storing, reconstructing, filtering and analysing the data are performed by the computing system.

In the following subsections, the general experiment layout and the TDAQ system will be described in details.

3.4.1 The active diamond target

The multiple coulomb scattering inside the target worsens the knowledge of the momentum and direction of the primary beam and spoils the missing mass resolution. In fact the missing mass cannot be calculated without determining the decay vertex and the direction of the beam. In the visible search the determination of the decay vertex helps to clean up the signal from the background. For this reason a $100\mu\text{m}$ target thickness is used. The simulation shows that for such a thickness the relationship

$$E_{\gamma, Brems} + E_{e^+} = E_{Beam} \quad (3.3)$$

is satisfied with a resolution better than the initial uncertainty of the beam energy ($\sim 1\%$). The probability of annihilation is 5% for a bunch of $10^4 e^+$ [80]. The study of the impact of spatial resolution of beam positioning is shown in Fig. 3.10, where the resolution of the square of the missing mass is reported for a mass A' of 15 MeV, assuming a perfect determination of the position of the incident photon on the calorimeter, and a realistic one, with 3mm resolution.

To obtain a resolution on the square of the missing mass lower than $30\text{MeV}^2/c^4$ it is necessary to determine the average position of the beam on the target with spatial resolutions better than the 2mm, position to be used then in the calculation of the angle with which the photon was emitted. A particle beam bunch at the BTF is characterised by a very small spot whose position is difficult to maintain permanently over time due to the instability of the current that feeds the bending magnet. The active target consists of a $2\text{cm} \times 2\text{cm} \times 100\mu\text{m}$ polycrystalline diamond positioned in the vacuum. On the edges of the sensor, 19 ohmic electrodes orthogonal

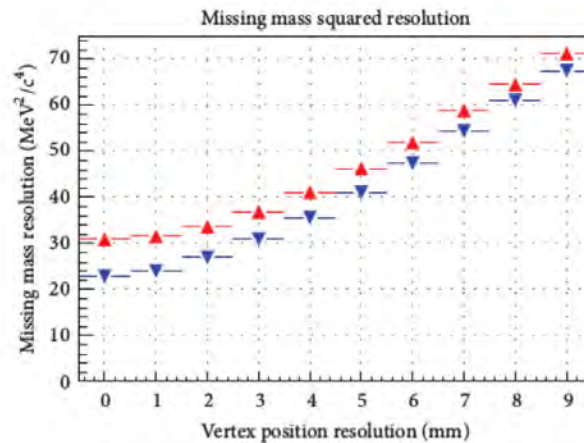


Figure 3.10. Dependence on the resolution of the square of the missing mass from the resolution on the determination of the interaction vertex for a A' of mass 15 MeV.

to each other have been made in order to detect the ionisation signal of the positron beam and determine its transverse profile.

In Fig. 3.11, two different types of active target, built for the experiment are shown, one with metal electrodes and one with nano-graphite electrical contacts. The nano-graphite has been chosen by PADME as more suitable for the experiment since the target is entirely made of carbon.

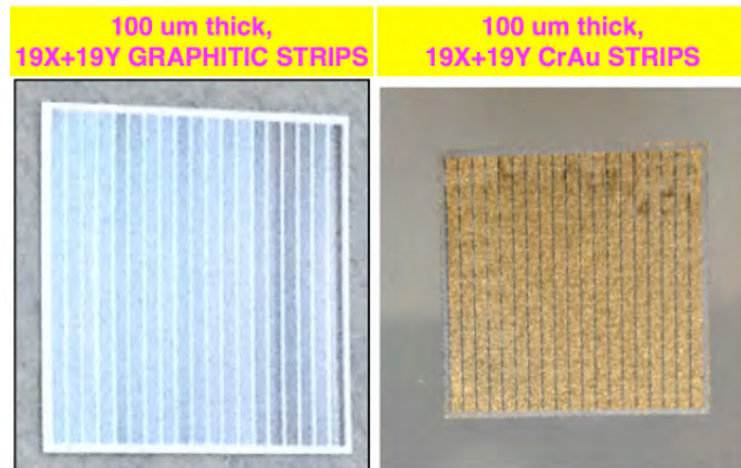


Figure 3.11. Picture of two types of diamond target.

The average beam profile measured in a BTF test is shown in Fig. 3.12. The resolution obtained for the beam positioning is $200\mu\text{m}$, much better than the 2mm required by the experiment.

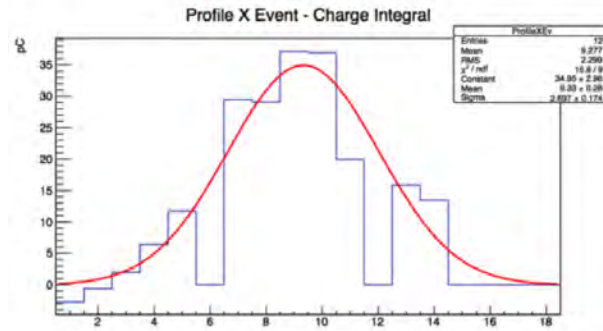


Figure 3.12. Profile along the horizontal axis of the BTF beam as measured by the prototype PADME diamond detector.

3.4.2 The dipole magnet

After the interaction with the target, the charged particles enter the magnet region. Due to the small thickness of the target, most of the particles remain in the beam, losing a negligible fraction of their energy.

The PADME magnet is a H-shaped dipole magnet, with a length of 1 m, with a $50 \text{ cm} \times 26 \text{ cm}$ gap and a maximum magnetic field of 1.4 T, reachable for 675 A current, and a total weight of 15 tonnes (see Fig. 3.13).

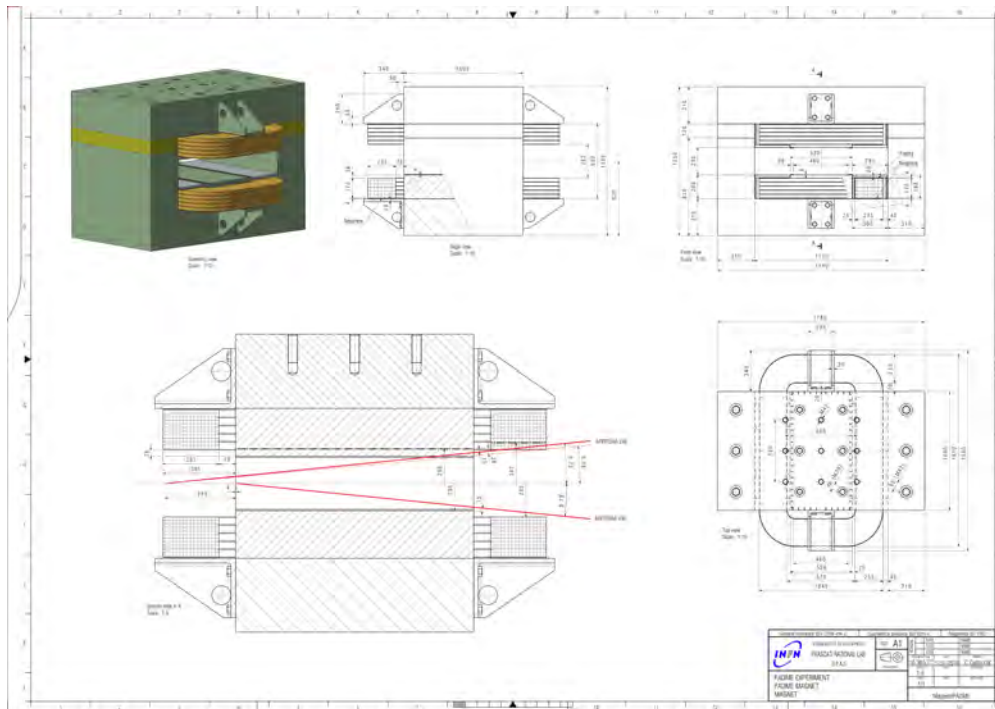


Figure 3.13. Picture of the PADME dipole magnet.

The simulation with the GEANT4 program shows that a magnetic field of $\sim 0.45 \text{ T}$ is sufficient to deflect the primary particles of the 550 MeV outside

the acceptance of the electromagnetic calorimeter. The deflection varies with the intensity of the magnetic field B applied following the function:

$$\phi = \arcsin\left(\frac{0.3 \cdot L \cdot B}{p}\right) \quad (3.4)$$

Due to the magnet action it is also possible to identify charged particles produced by interactions with the diamond target (positrons radiating a γ , or particles produced by inelastic collisions). In fact these particles, of energy lower than the beam one, are diverted inside the magnet, leaving a signal on the veto of charged particles built inside the vacuum chamber which is located in the gap of the magnet. Before being installed in the experiment, the dipole magnet underwent detailed magnetic field measurements at LNF. Precise measurements of magnetic field strength by using a Hall probes has been made along X,Y and Z directions have been made. The results of X and Z scans are shown in Figs. 3.14 and 3.15.

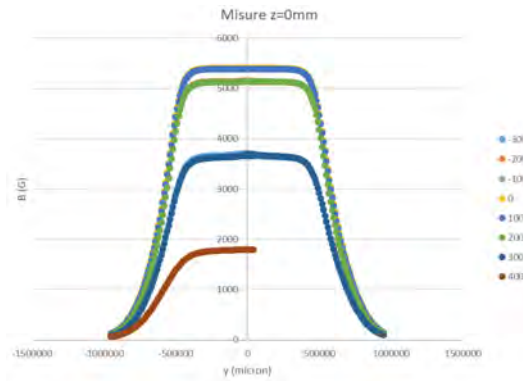


Figure 3.14. Detailed scan along Z (from -95cm to +95cm, steps of 1cm).

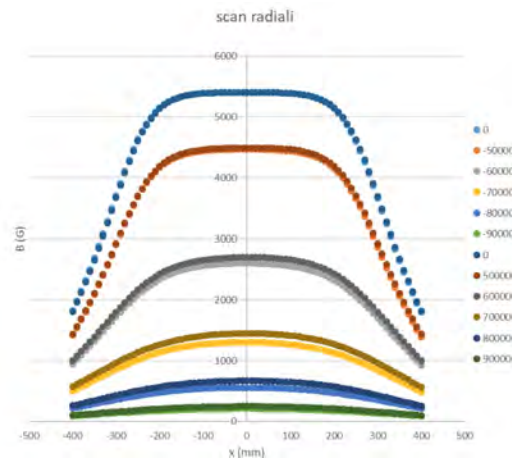


Figure 3.15. Detailed scan along X (from -40cm to +40cm, steps of 1cm).

These measurements are crucial to calibrate the spectrometer response using MonteCarlo simulations.

3.4.3 The vacuum system

Due to the high intensity of the beam and the extreme small target thickness of around $0.04\% X_0$ of radiation length, the positrons that interact with the air can produce a strong contribution to the background events. In fact, since the air radiation length is 285 m at a pressure of 1 mbar and the distance of the calorimeter from the target is about ~ 4 m, the air thickness is $\sim 1\% X_0$, much larger than the thickness of the target itself [86]. A MonteCarlo simulation made at a pressure of 1 mbar shows a significant increase of the background compared to an experiment in vacuum. When there are interactions with the residual air, the kinematic constraints (for example the missing mass) cannot be correctly reconstructed since the position of the interaction vertex is not known. The PADME vacuum system was designed to keep the experiment at a pressure of 10^{-6} mbar. At this vacuum level a negligible number of background events due to beam-air interactions are produced. The vacuum vessel is integrated with the magnet gap and with the positron and electron vetoes. The presence of the magnetic field coupled to the positron beam introduces a strong left right asymmetry in the distribution of tracks after the target. This reflects in an asymmetric design of the vacuum chamber which follows as much as possible the positron path in the magnetic field. A sketch of the vacuum system in the magnet region is presented in Fig. 3.16.

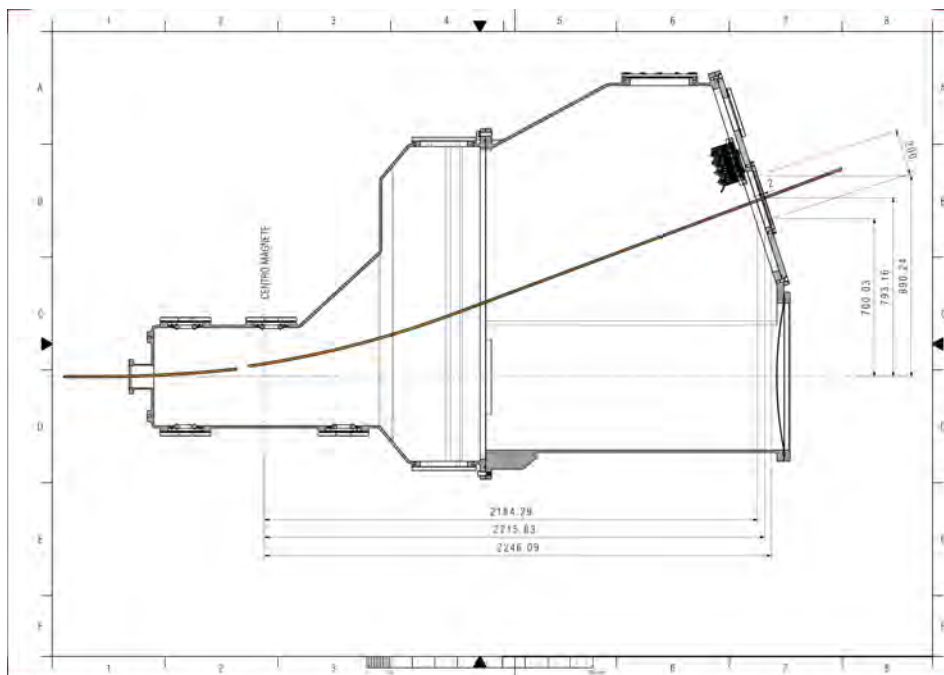


Figure 3.16. Layout of the PADME vacuum system magnet region

3.4.4 The charged particles Veto detectors

One of the dominant backgrounds of the experiment is the positron Bremsstrahlung. Whenever a positron of the beam interacts with the target radiating a photon of energy E in the calorimeter, simulating a single photon event similar to $e^+e^- \rightarrow \gamma A'$,

it will be deflected inside the magnetic field region and guided in to the Veto system. One handle for reducing this background is the central hole in the calorimeter, removing from the acceptance a large fraction of bremsstrahlung photons, due to their very peaked angular distribution. The use of the fast small angle calorimeter will also allow detection of this missing photons. However, detecting the positrons that have lost a significant amount of energy, would allow more stringent cuts and further background suppression. Depending on the energy of the photon, the emitted positron can be inside the veto acceptance or, for softer photons, stay closer to the E_0 trajectory and escape detection.

In order to cover both regions, two different veto detectors are placed both inside and outside the magnetic field:

- The first one is placed along the side of the gap of the PADME magnet. By suitably segmenting this detector, it is possible to have a measurement of the momentum of the positron from its impact position. This detector is called Positron Veto (PVeto). Since a dark photon can also decay into an e^+e^- pair, the magnet gap lateral surface is also instrumented on the opposite side with respect to the positron curvature. This symmetric detector is called Electron Veto (EVeto). The two systems are shown in Fig. 3.17.



Figure 3.17. Picture during the installation of the PVeto and EVeto inside the vacuum chamber.

- For the higher energy positrons, escaping the acceptance of the PVeto, an additional detector is placed outside the magnet, covering larger curvature radii (i.e. smaller deflection angles). This detector is called “High Energy Positron Veto” (HEPVeto). A picture of the HEPVeto is visible in Fig. 3.18.

All the three detectors are made of plastics scintillator bars (96 for the PVeto, 96 for the EVeto and 16 for the HEPVeto) with approximate dimensions $1 \times 1 \times 18.6\text{cm}^3$. The scintillators are grooved longitudinally and the light is collected by a 1.2mm diameter BCF-92 wave-length shifter fibre, glued in the groove with BC-600 optical cement. The readout is performed with a $3 \times 3\text{mm}^2$ Hamamatsu S13360 silicon photomultiplier (SiPM), whose contact with the fibre is obtained with a Momentive RTV615 silicone rubber compound. The SiPMs are mounted on a custom designed

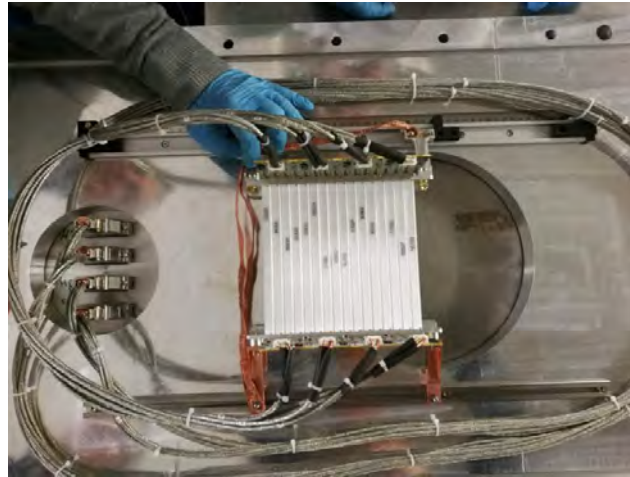


Figure 3.18. A picture of the HEPVeto taken during its installation.

PCB housing the front-end electronics and a control circuit, which allows to adjust and measure the bias voltage for each SiPM.

All the veto systems are presented in Fig. 3.19.

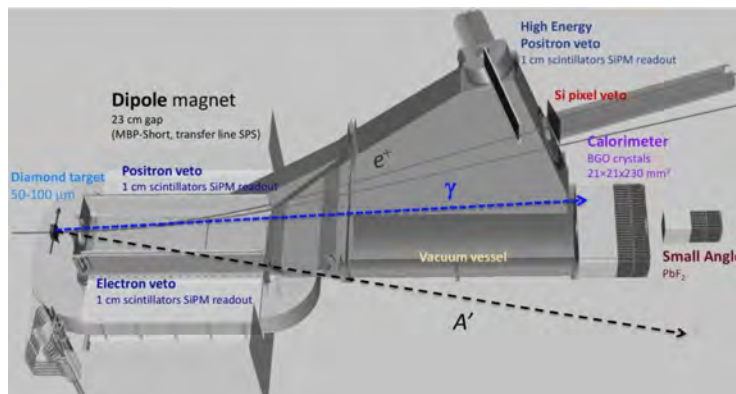


Figure 3.19. Charged particles veto system layout and vacuum vessel.

3.4.5 The electromagnetic calorimeter

The electromagnetic calorimeter plays a fundamental role in this experiment, which consists in the reconstruction of the four-momentum of the photon and therefore in the measurement of the missing mass of the new vector boson. The main requests on the calorimeter are that the energy and the position of the reconstructed photon are measured with few % and few mm resolution respectively, and that the time of the particle is measured with better than 1 ns resolution to reduce the pileup. The choice of the active material used determines the *Molière* radius of the produced electromagnetic cluster, which in turn imposes limits on the minimum granularity of the calorimeter. The spatial resolution request, together with the good angular resolution, determines the distance between the calorimeter and the target. The PADME calorimeter is a homogeneous crystal calorimeter with an approximately cylindrical

shape, a ~ 600 mm diameter, a depth of 230 mm, and a central $100 \times 100 \text{ mm}^2$ square hole. The active volume consists of 616 $21 \times 21 \times 230 \text{ mm}^3$ BGO crystals, obtained by machining the crystals retrieved from one of the end-caps of the dismantled L3 experiment at LEP[87] electromagnetic calorimeter. This material is characterised by a high density, equal to 7.13 g/cm^3 , with a small radiation length X_0 , equal to 1.12 cm, a small *Molier* radius, equal to 2.23 cm, and a scintillation decay time of 300 ns. According to the tests performed by the L3 collaboration [88], the expected energy resolution lies in the interval $(1 - 2)\% \sqrt{E}$ for electrons and photons of energy $< 1 \text{ GeV}$. The calorimeter is shown in Fig. 3.20.

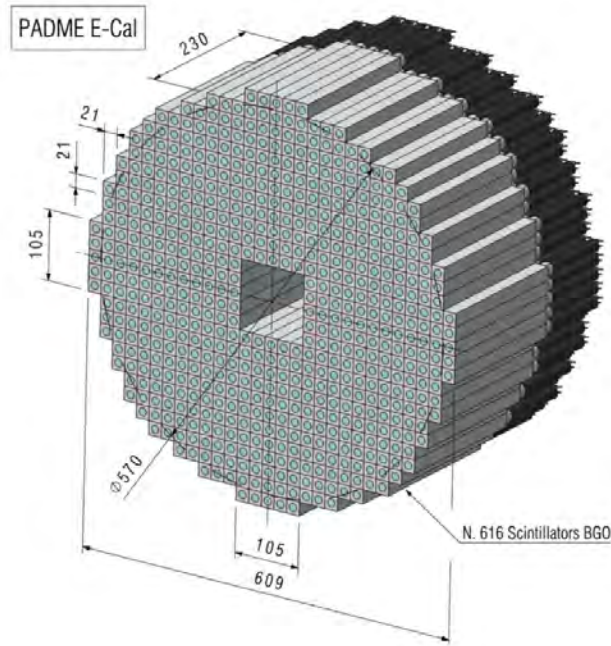


Figure 3.20. The PADME BGO crystal calorimeter.

Early tests aimed at determining the best readout technology showed that avalanche photodiodes (APDs), even with a relatively large active region of $10 \times 10 \text{ mm}^2$, have a gain and therefore a total collected charge, which is insufficient to obtain a high energy resolution in the PADME-related energy range, from a few to a few hundred MeV. The readout system is therefore based on 19 mm diameter photo-multiplier tubes provided by HZC Photonics.

The measured and expected energy resolution is shown in Fig. 3.21.

This resolution is well described by the formula:

$$\frac{\sigma_E}{E} = \frac{a}{\sqrt{E}} \oplus \frac{b}{E} \oplus c \text{ [GeV]} \quad (3.5)$$

where $a = 2.0\%$, $b = 0.003\%$, $c = 1.15\%$ are the three free parameters determined by the result of the fit, shown in Fig. 3.21. The agreement in between resolutions extracted from samples with different electron energies points to a very good quality

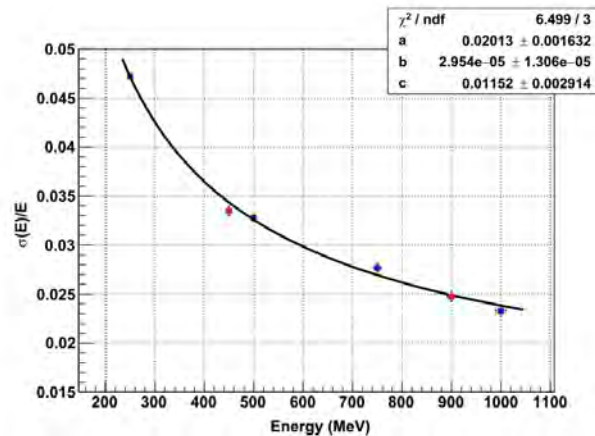


Figure 3.21. Energy resolution of the PADME calorimeter as a function of the deposited energy (250 MeV e^- blue points and 450 MeV e^- red points). Figure from [89].

of the beam and reproducibility of the detector conditions. The measurement of the calorimeter energy resolution includes so far the effect of the beam energy spread. In order to check the beam contribution to the calorimeter resolution an unfolding on the 1% beam spread from the data points was performed. After repeating the fit a reduction of the a term of just 0.1 (~ 5) was obtained.

3.4.6 Small Angle Calorimeter

Excellent background rejection capability is needed for the PADME experiment. Among the main background sources are 2-gamma ($e^+e^- \rightarrow \gamma\gamma$) and 3-gamma ($e^+e^- \rightarrow \gamma\gamma\gamma$) cases, where 1 or 2 photons escape detection through the ECAL central hole. A very fast Small-Angle Calorimeter (SAC) is mounted behind the main ECAL in order to mitigate these backgrounds [90]. The SAC consists of 25 PbF_2 crystals, each with $30 \times 30\text{mm}^2$ in transverse dimensions, and 140 mm in length. Therefore, the total transverse area is $150 \times 150\text{mm}^2$, which is slightly larger than the ECAL central square hole. The non-interacting beam is redirected through a 0.45 T magnet to an off-axis beam dump. Depending on the intensity of the beam, the photon rate in the central crystal due to Bremsstrahlung is expected to reach several hundred MHz.

The front face and each crystal's lateral surfaces are covered with 50 μm thick black Tedlar foil to reduce optical cross-talk, while the back face is coupled with Hamamatsu R13478UV PMTs using UV transparent optical grease, matching the refractive index of the crystal for optimal light transmission. The SAC just after its assembly is shown in Fig. 3.22.

3.5 PADME trigger and data acquisition system

Due to the moderate amount of channels and the relatively low trigger rate provided by the beam bunches, the trigger and DAQ of the PADME experiment is relatively simple. Nevertheless, the flash analogue to digital converter (FADC) boards used in

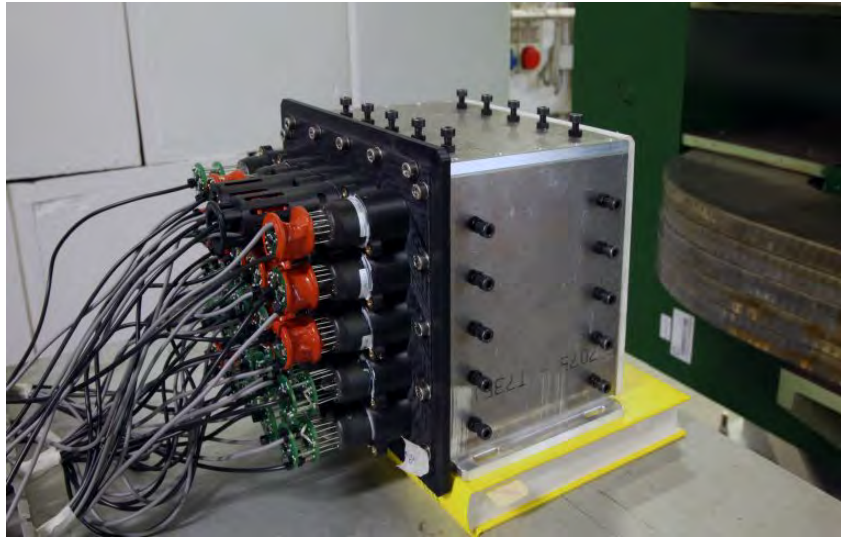


Figure 3.22. View of the Small Angle Calorimeter before its installation.

the PADME readout need some early data reduction to prevent large quantities of useless FADC samples being recorded on disks. The PADME DAQ system reads data from 921 channels, outlined in the following table, with an estimated transmission rate of 50 Hz, specified by the Linac duty cycle of DAΦNE [91].

Detector	Channels
Diamond Target	32
Electromagnetic Calorimeter	616
Small Angle Calorimeter	25
Charged Particles Veto System	218
Total	921

Due to the extremely thin target, a calorimeter cluster is observed just in 10% of the bunch, and even in this case only a few crystals will have a significant energy deposit. In order to reduce the raw data size by a factor 50 or more, the PADME trigger system must perform channels zero suppression and event selection at different levels.

FADC data from V1742 boards mounted on the active diamond target, the veto and both calorimeters. While the calorimeter and the active target are operated at a digitisation frequency of 1GS/s due to their very slow signals, veto detectors and SAC are operated at 2.5GS/s to improve time resolution. The trigger system of the PADME experiment is based on a trigger-less decision at level 0. After receiving the 50 Hz NIM digital trigger signal from the DAΦNE linac (LINAC-SYS), which is related with the time of arrival of particles in the BTF line (with an adjustable delay), all the FADC readout boards start to digitise 1 μ s or 0.4 μ s depending on

the digitisation frequency and to send their data to the front end PC through direct optical links. The timing of the distributed trigger signal is crucial to allow all readout boards to synchronise better than 0.2 ns, providing all detectors with the appropriate timing.

BTF beam trigger

The electronics of the linac gun pulser drives the square waveform supplied to the gun for the emission of primary electrons, and also generates the master clock of the DAΦNE accelerator complex to which the DAΦNE accelerator device and all timing references are attached. The BTF receives a reference signal via a digital delay generator, which enables the proof of an adjustable width and standard trigger signal (TTL or NIM) with an arbitrary delay in the arrival of electrons in the BTF hall in steps of 1 ns, from $-14\mu\text{s}$ (in advance with respect to the particles). The jitter of the digital delay generators used in the system is of 50 ps, so that a very precise and stable reference is provided with respect to the time of arrival of electrons.

3.5.1 L0 trigger

Two parts make up the level 0 trigger the L0 Trigger Distribution boards and the L0 trigger algorithm program. The L0 Trigger Distributor board receives from the beam and calibration systems the trigger signals, then constructs the logical OR and generates multiple synchronous copies of this signal in output.

When a trigger is received from the L0 Trigger Distribution system, the L0 DAQ system will read all available information stored in the DAQ boards internal buffers. The L0 DAQ system software consists in several independent processes, one per readout board, running on the front-end servers and coordinated by a Central DAQ Manager.

Data from the CAEN V1742 ADC boards will be processed by the L0 DAQ system. The system will apply the correction procedures provided by the manufacturer, followed by a zero-suppression algorithm, aiming to reduce the event data size by suppressing any digitized stream from the calorimeter not containing real energy deposits. At this stage further data reduction algorithms (delta compression, Huffman, etc.) can be applied if required and if compatible with the time constraints. Data from each individual board will then be written to a temporary disk buffer as independent files.

3.5.2 L1 trigger

The trigger PADME L1 is fully implemented in software and runs on the same machines that are used for the software portion of L0. The L1 trigger's aim is to further reduce data and select an event-based collection.

A series of L1 processes will read data from the files corresponding to the same set of events and perform an initial reconstruction and filtering of the events.

Upon zero suppression, a significant fraction of the calorimeter data (10% to 50%) will come from the digitized trigger signal. The L1 must suit the trigger signal to generate a fine time 32 bit trigger to be used in the board-to-board synchronisation process in order to further minimise the data size.

An initial reconstruction will then be performed on the full event and a set of physics oriented filters will be applied to the data. After that, the data will be merged in the so-called RAW data structure which will then be written to ROOT-based [92]. In the initial phase of the experiment, the L1 trigger will function in flagging mode and all events will be written to the output files, irrespective of the result of the physics-oriented filters. In a second phase, if data storage considerations require it, L1 can be switched to rejection mode so that only events passing one or more of the filters will be written to the output files.

Fig. 3.23 shows the DAQ data processing model scheme.

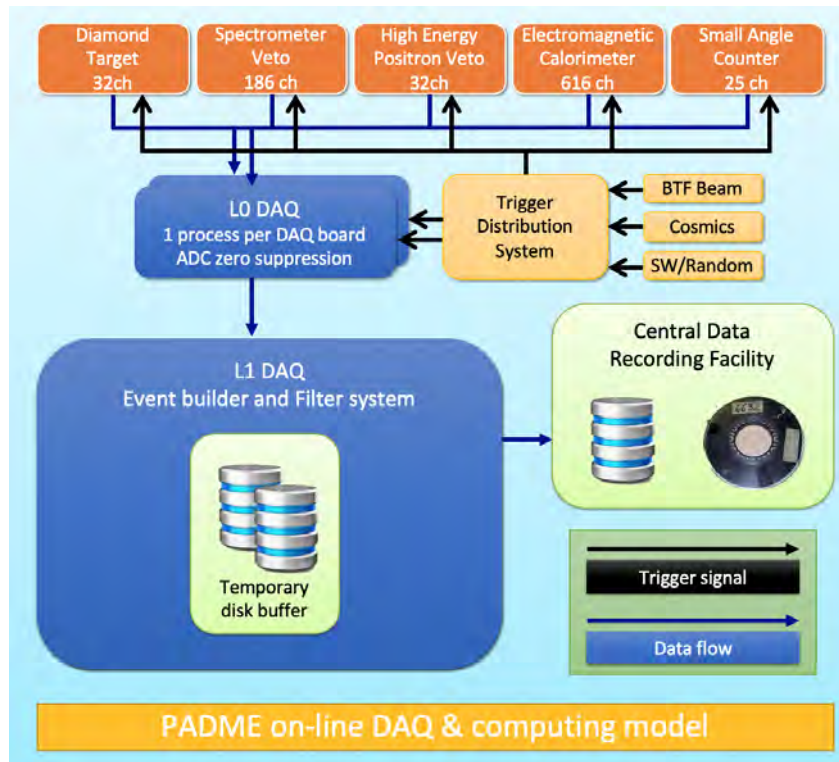


Figure 3.23. Logical schema of the PADME DAQ system.

3.6 GEANT4 simulation

A full experiment simulation based on GEANT4, called PadmeMC, was developed during the project's early stages in 2014. It has since followed closely the evolution of the experiment design and has been used to verify the effect of the proposed technical choices on the resolution of the A' mass measurement recoil and to optimize the parameters of the construction.

3.6.1 Kinematics and beam simulation

Using standard GEANT4 physics libraries, the interaction of the beam particles with the active target and the resulting event kinematics are modelled. The PADME physics list is extracted from the GEANT4 package's standard QGSP BERT physics list. It includes multiple scattering, Coulomb scattering, ionisation, Bremsstrahlung emission, two photon annihilation, synchrotron radiation emission, and optionally optical photons tracking. Specific datacards allow the inclusion of photonuclear interactions and the selection of the high precision neutron transport library.

The simulation of the annihilation process with the output of dark photons, $e^+e^- \rightarrow \gamma\gamma$, is done by a custom generator that can be triggered and configured via data cards, while the kinematics of three photons final state events, $e^+e^- \rightarrow \gamma\gamma\gamma$, was generated externally to GEANT4 using the generator CalcHEP [93].

A good description of the incoming positron beam characteristics is crucial in the calculation of the A' recoil mass and to correctly determine its the resolution. The simulation is based on BTF beam line experimental studies and allows all related beam parameters to be adjusted:

- total duration and internal time structure of the particle bunch;
- energy spread, spatial distribution and emittance of the beam spot at the target.

The beam simulation package also includes methods to produce special events for the calibration of the electromagnetic calorimeter where fixed energy photons are directed to specific areas of the detector.

3.6.2 Detector simulation

As stated before, all detectors composing the PADME experiment were fully modelled and simulated with GEANT4 since their inception. The inclusion of datacards to control the relevant construction parameters allowed a straightforward way to study the effect of engineering choices and physical constraints on the physics results.

The set of adjustable parameters includes major construction choices, such as the relative positions of each detector in relation to the target, together with the dimensions of the components of each detector, e.g. the length of the plastic scintillator fingers in the veto system, down to small details, such as the thickness of the paint coating around each BGO crystal and the width of the air gap between the crystals in the electromagnetic calorimeter. A layout of the simulated experiment setup is shown in Fig. 3.24.

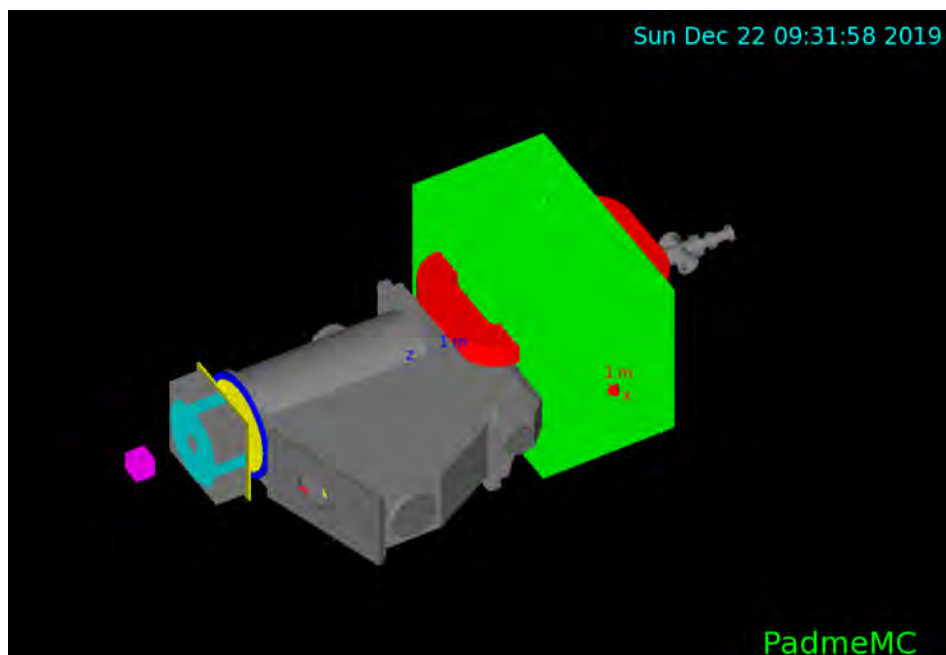


Figure 3.24. Simulation of the PADME experiment with GEANT4.

Chapter 4

Positron momentum reconstruction

The aim of this thesis is to search background events for Dark Higgs decaying in a final states with six charged leptons, respectively three positrons and three electrons. For this research, the characteristics of the Veto systems and the dipole magnet were exploited. To reconstruct DH background events, the momentum of the charged particles detected by the Vetos needs to be reconstructed first. In order to do so, a theoretical treatment of the Veto physics is required, which must be verified on the data generated by the GEANT4 simulation of the experiment.

In this chapter we will describe the construction of a theoretical model for the Veto physics, proofs of its validity based on the data generated by the GEANT4 simulation with different characteristics and its skills in the reconstruction of the charged particles momentum.

4.1 Analytical model for the momentum reconstruction

From the interaction between the incident beam and the active diamond target, positrons and electrons with different energies are generated, which enter the vacuum chamber and are immediately affected by the presence of the magnetic field. According to the Lorentz's law, these particles will begin to follow a circular trajectory until they impact on the Veto systems (the electrons will arrive on the EVeto system while the positrons on the PVeto system). Since the structure of both EVeto and PVeto systems is the same, in this chapter we will discuss only the PVeto system, made of 90 scintillating fingers.

In order to construct a theoretical model of the problem, Lorentz's law and its effects must be taken into consideration. Knowing that the positrons entry point into the vacuum chamber does not coincide with the center of the circumference they travel, the following system of equations can be used to describe the particle trajectory:

$$\begin{cases} x = R - D \\ x^2 + z^2 = R^2 \end{cases} \quad (4.1)$$

where x represents the center of the circumference, R the radius of the circumference and $D = 18.25\text{cm}$ the horizontal distance from the entry point of the positrons

to the PVeto system. Using the Lorentz's law the following equation connecting radius and momentum of the particle can be obtained:

$$R[\text{mm}] = \frac{P[\text{MeV}]}{0.3 \cdot B[\text{T}]} \quad (4.2)$$

where P is the positron momentum and $B = 0.45\text{T}$ is the magnitude of the dipolar magnetic field. Finally it is possible to obtain a relation between the position of impact on the PVeto and the positrons momentum

$$z(P) = \sqrt{D(2R - D)} \quad (4.3)$$

Once the following analytic function has been obtained, two aspects related to the physics of the PADME experiment must be considered. The PVeto system has a distance from the vacuum chamber of $a = 2.6\text{cm}$. The second aspect concerns the physics of the magnetic field. As explained in chapter 3, the dipolar magnetic field of the PADME magnet is not constant in the region of the vetos. Measurements show that at the borders its values has a Gaussian like fall down. This Gaussian tails includes the zone where the target is placed and cannot be reproduced using an analytic function but can be parameterised using measured values and a linear interpolation. To account for the complicated shape of the magnetic field in the analytic function, it is necessary to replace the fringe field area of the dipolar magnetic field with a rectangular one with constant field, replacing the real distance between the target and the beginning of the vacuum chamber with an effective distance $b = 16\text{cm}$. In conclusion, the analytic function for the reconstruction of charged particles momentum takes the following form:

$$z(P) = \sqrt{D(2R - D)} + a + b \quad (4.4)$$

This function can also be written in the following way, including the expression of the radius in Eqn. 4.2:

$$P(z) = \left(\frac{D^2 + (z - a - b)^2}{2D} \right) \times 0.3 \cdot B \quad (4.5)$$

Diagram modelling the analytic treatment proposed, with all the quantities measured, is visible in Fig. 4.1. The trend of the momentum of the positrons as a function of the PVeto scintillating finger hit by the particle obtained with the Eq. 4.5 is shown in Fig. 4.2.

The analytic function correctly describes the behavior of the positrons momentum detected by the PVeto system. From this function it is possible to obtain the momentum relative resolution for the PVeto system. In order to obtain such resolution the minimum and maximum momentum that can be found on a scintillating finger must considered. These quantities can be obtained using the inverse of the Eq. 4.4, knowing that a scintillating finger is 1.1cm long in the beam direction.

$$P_{max/min} = \left(\frac{D^2 + z(P)_{max/min}^2}{2D} \right) \times 0.3 \cdot B \quad (4.6)$$

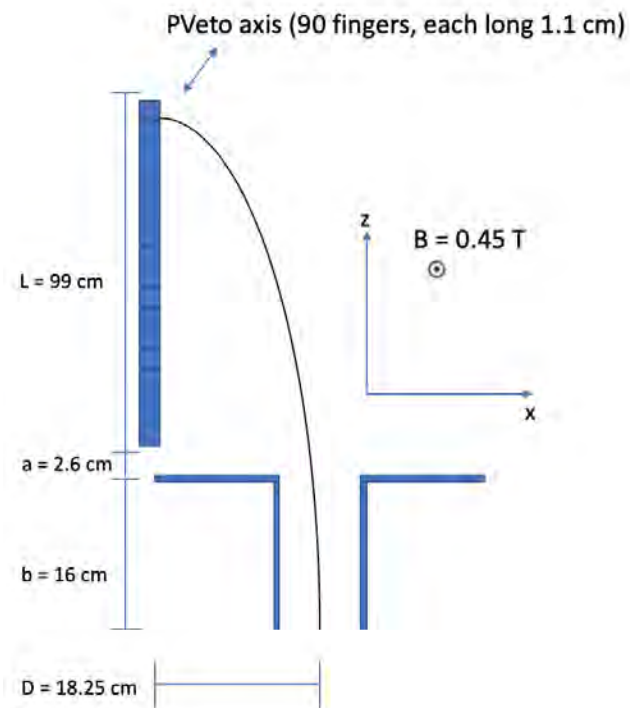


Figure 4.1. Graphical representation of the physics of the PVeto system with all the quantities used for the construction of the analytical function.

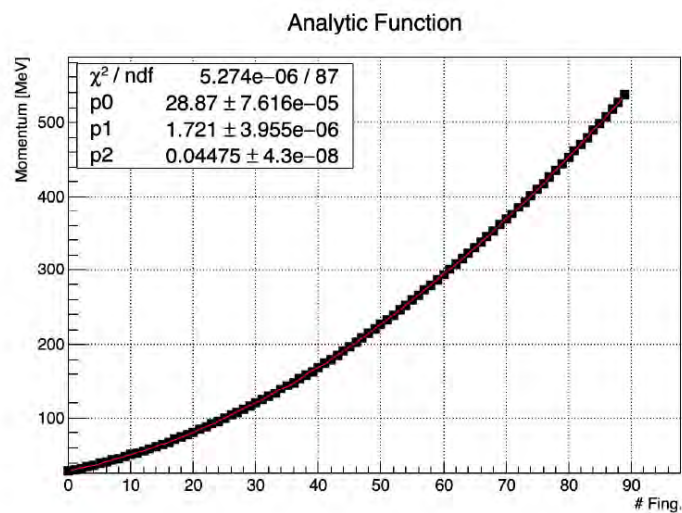


Figure 4.2. Positrons momentum as a function of the hit finger on the PVeto system.

Calling ΔP the difference between the maximum and minimum momentum and P_{mean} the average momentum value found on every scintillating finger, by plotting $\frac{\Delta P}{P_{mean}\sqrt{12}}$, that is the variance root of an uniform continuous distribution, as a function of the momentum, it is possible to obtain the relative resolution of the PVeto system predicted by the analytic function. Such resolution is shown in Fig. 4.3.

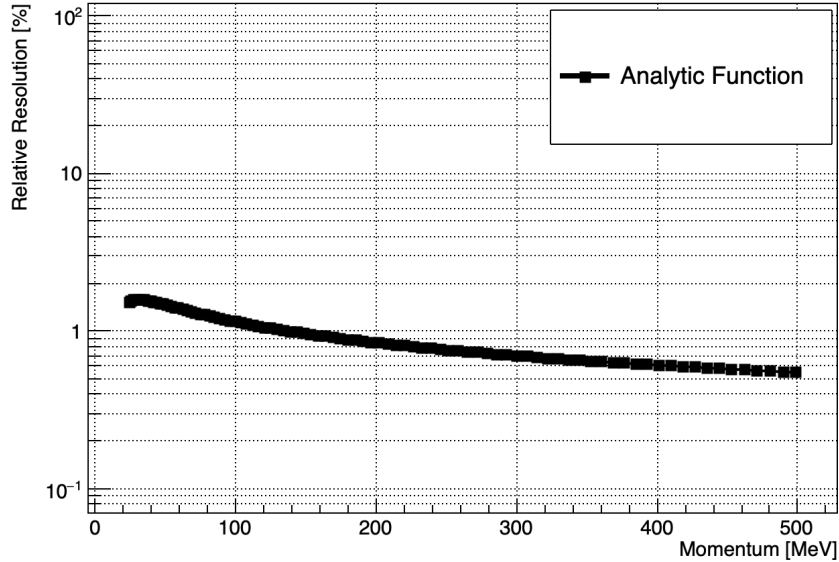


Figure 4.3. PVeto system relative resolution as a function of the positron momentum, according to the analytic function.

The analytic function leads to a relative momentum resolution around 1%. This is a very interesting result since, if actually confirmed, it would indicate a very high accuracy for the PADME spectrometer momentum measurements. In order to verify such result, data from the GEANT4 MonteCarlo simulation must be generated and compared with the analytic function.

4.2 MonteCarlo simulation

The MonteCarlo simulation of the PADME experiment can produce data in two different modes: Single Particle and Full Bunch Structure mode. In Single Particle mode, particles of different energies are sent to the active diamond target, up to a maximum chosen by the user, with initial direction parallel to the beam axis. In Full Bunch Structure mode, bunch of particles are sent in the experimental hall with the same energy and with a spread in the incoming directions. While the latter mode best represents the best realistic case of the PADME experiment, the Single Particle mode is an ideal approach but useful to understand the behaviour of the spectrometer.

In the following subsections, after showing the approach used to study the data obtained with the GEANT4 simulation of the experiment, the analytic function will be tested in order to understand if it is good enough for the DH background events

reconstruction. It will be first used on data generated in Single Particle mode with different configurations of the experimental setup, and then on data produced in Full Bunch Structure mode, to evaluate how much this theoretical model satisfies the reality of the experiment.

4.2.1 Momentum reconstruction technique

In this subsection the technique used to convert the information available from the PADME detector, the number of finger hit by a particle, into a value of the incident particle momentum is described. In order to validate the analytic function, the simulation of the PADME experiment has been used to obtain complete treatment of the magnetic field map inside the PADME magnet.

The simulated data in Single Particle and Full Bunch Structure mode were generated with different conditions. For Single Particle mode particles of defined energy ranging from 10 MeV to 510 MeV in steps of one MeV, while in Full Bunch Structure mode only particles of 550 MeV with 1% energy spread were generated. In the last case all the energies lower than 550 MeV were obtained through radiation emitted by the positron in the target. The first information that can be extracted from the simulation is the correlation between the particle momentum and the impact point in the Veto measured in terms of number of finger. Examples of such correlation for Single Particle and Full Bunch Structure modes are shown in Fig. 4.4

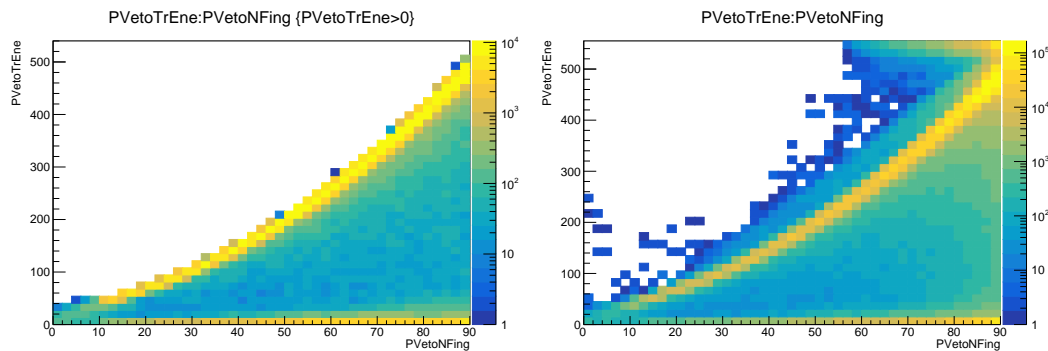


Figure 4.4. Example of energy deposited as a function of the scintillating bar for both the the Single Particle mode (left side) and Full Bunch Structure mode (right side).

The next step is to obtain a relative resolution to be compared with the one obtained from the analytic function. Histograms of all the scintillating fingers of the PVeto system containing information on which energies were revealed during the simulation were prepared. An example of these histograms is shown in Fig. 4.5.

To associate an energy value to the finger in the considered histogram, two different technique were used. For Single Particle mode mean and standard deviation of the distribution were used while for Full Bunch Structure mode histograms a Gaussian fit function was used. The difference in the standard deviation on the two distributions is due to the presence of the target in the Full Bunch Structure mode simulation only. In fact, due to the interaction with the target, positrons can reach a selected bar, not only if they have the exact momentum required, but also due the angle with respect to the beam axis induced by the interaction.

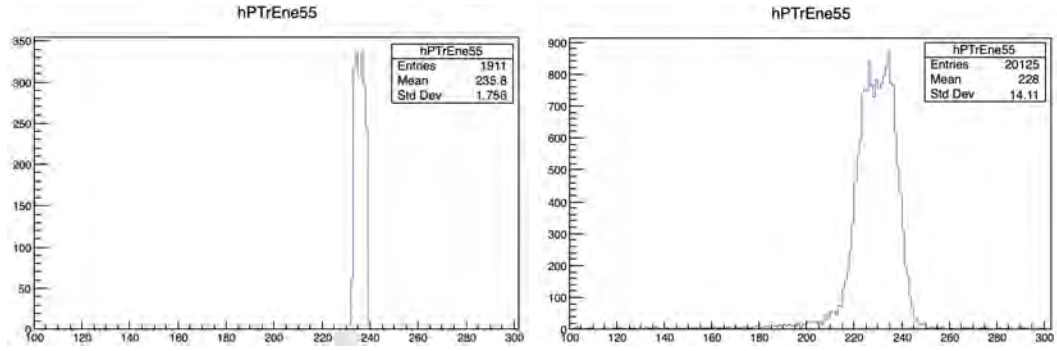


Figure 4.5. Example of energy deposited in the scintillating finger n. 55 of the PVeto system for both Single Particle (left side) and Full Bunch Structure mode (right side).

Using this technique a positron momentum graph as a function of the hit finger was obtained, as illustrated for both modes in Fig. 4.6.

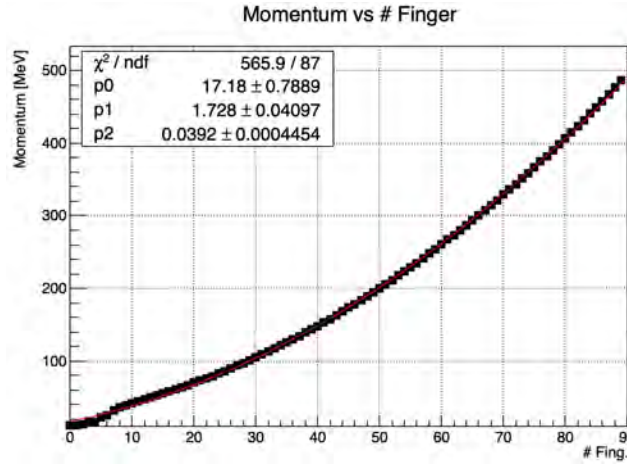


Figure 4.6. Positron momentum as a function of the hit scintillating finger.

Such type of graph has been parametrized with a second degree polynomial function

$$P_{rec} = p_0 + p_1x + p_2x^2 = 17.2 + 1.73x + 0.039x^2 \quad (4.7)$$

and it is very similar to the one in Fig 4.2 obtained using the analytic formula. Such function is then used to reconstruct the momentum in the experiment once the impinging finger has been identified. To test the reliability of the obtained function, the difference in between the reconstructed momentum P_{rec} and the original MonteCarlo momentum P_{true} was calculated. The distribution of such difference is shown, for both Single Particle and Full Bunch Structure mode, in Fig. 4.7.

In Fig. 4.8 the average value of $P_{rec} - P_{true}$ divided by P_{true} as a function of the scintillating finger is presented. The figure shows some systematic effect for the first fingers, discussed in the following sections, and a very good agreement after finger number 30.

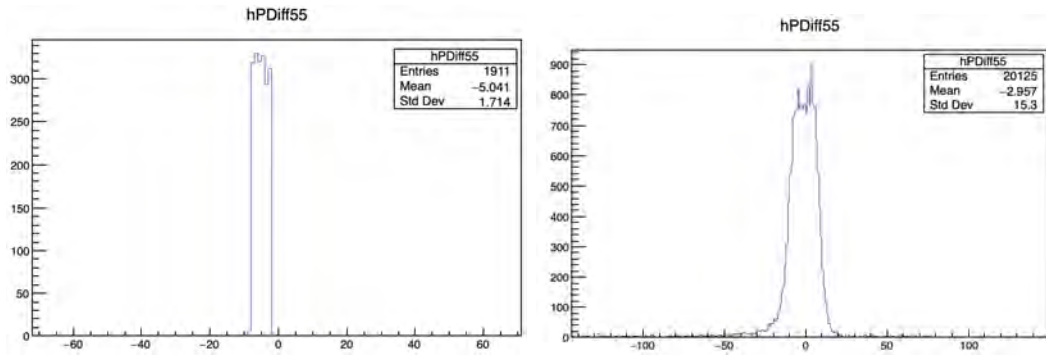


Figure 4.7. Example of $P_{rec} - P_{true}$ in the finger n. 55 of the PVeto system for both the the Single Particle mode (left side) and Full Bunch Structure mode (right side).

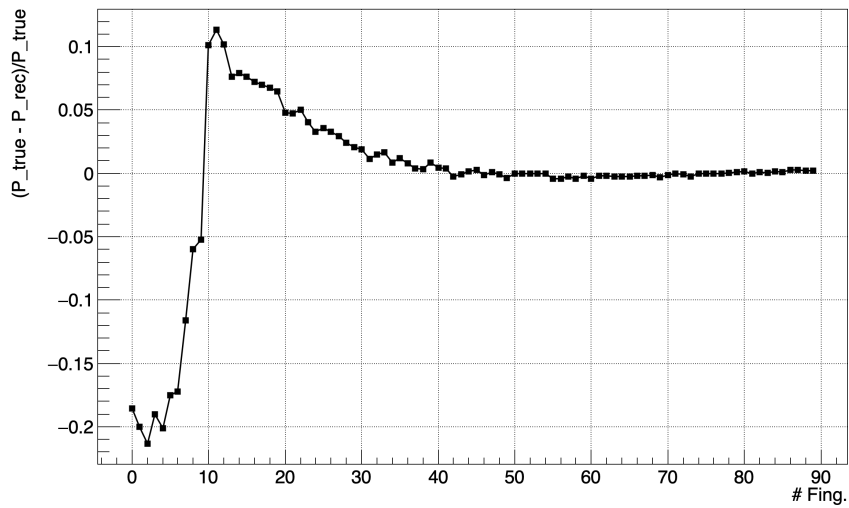


Figure 4.8. $(P_{rec} - P_{true})/P_{true}$ as a function of the scintillating finger.

The RMS of the distributions divided by the momentum of the particle entering the finger were used to obtain the relative resolution.

In the following subsections results of this analysis technique just presented will be shown together with a comparison between them and the analytic function one.

4.2.2 Single Particle

The first data simulated in Single Particle mode were in the absence of both target and vacuum chamber.

This sample was intended to simulate the momentum measurement in ideal conditions, to compare the MC results with the analytic function. The relative resolution as a function of the momentum, illustrated in Fig. 4.9, was obtained by applying the reconstruction explained in the previous section.

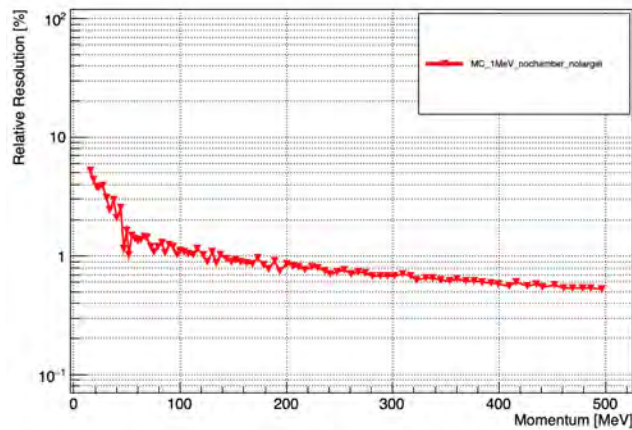


Figure 4.9. Relative resolution as a function of the momentum without the vacuum chamber and the target.

The MC resolution starts with a value of 4%, corresponding to 20MeV momentum and drops down below 1% for higher energies. In Fig. 4.10 MC resolution has been compared with the analytic function one.

The figure shows that the analytical function describes almost perfectly the simulated data without vacuum chamber except for the region below 40 MeV. The GEANT4 data deviation with respect to the analytic function in the low momentum region is due to the physics of the experiment.

To test the reconstruction in a more realistic environment, the studies described above were performed on a new dataset. The new set was generated with no target but adding the PADME vacuum chamber, to observe if the material of the chamber affects the detection of charged particles.

The relative resolution obtained from these new data is shown in Fig. 4.11

It is immediately evident that the low energy region is affected by the presence of the vacuum chamber.

The resolution got worse compared both to the no chamber simulation, and to the analytic function as presented in Fig. 4.12.

Through the GEANT4 simulation, it is possible to explain this bad performance at low energy. As shown in Fig. 4.13, obtained from the simulation of the experiment,

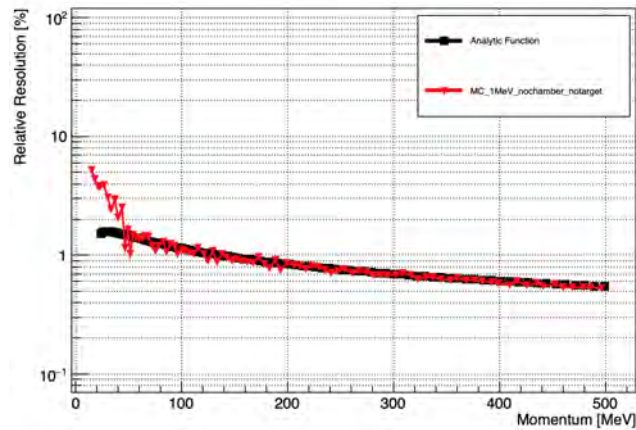


Figure 4.10. Comparison between the relative resolution of the theoretical method and that obtained from the Single Particle data without vacuum chamber and without target.

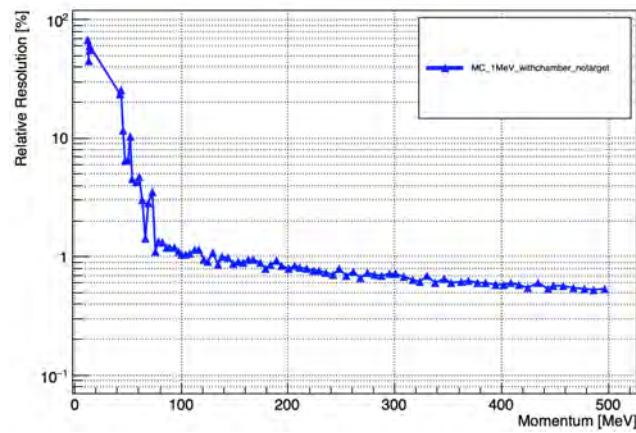


Figure 4.11. Relative resolution as a function of the momentum with the vacuum chamber and without the target.

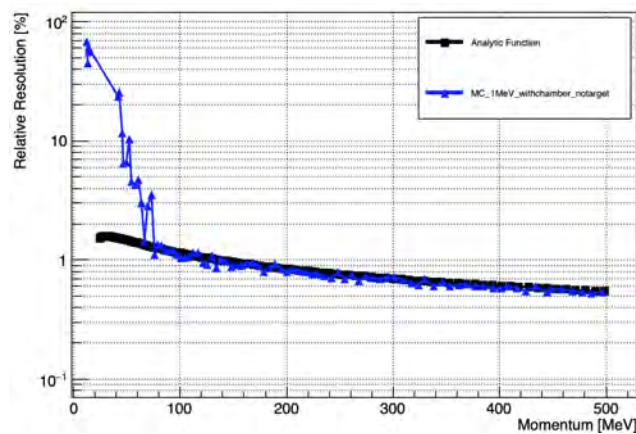


Figure 4.12. Comparison between the relative resolution of the analytical function and that obtained from the Single Particle data with no target and vacuum chamber.

the particles trajectory crosses the vacuum chamber before reaching the PVeto system. Because of this problem, the positrons can either disappear or their trajectory can be completely changed. According to simulation, this effect is important for particles up to $\sim 40\text{-}45$ MeV momentum, being the one represented in Fig. 4.13 crossing the narrowest region of the chamber entrance.

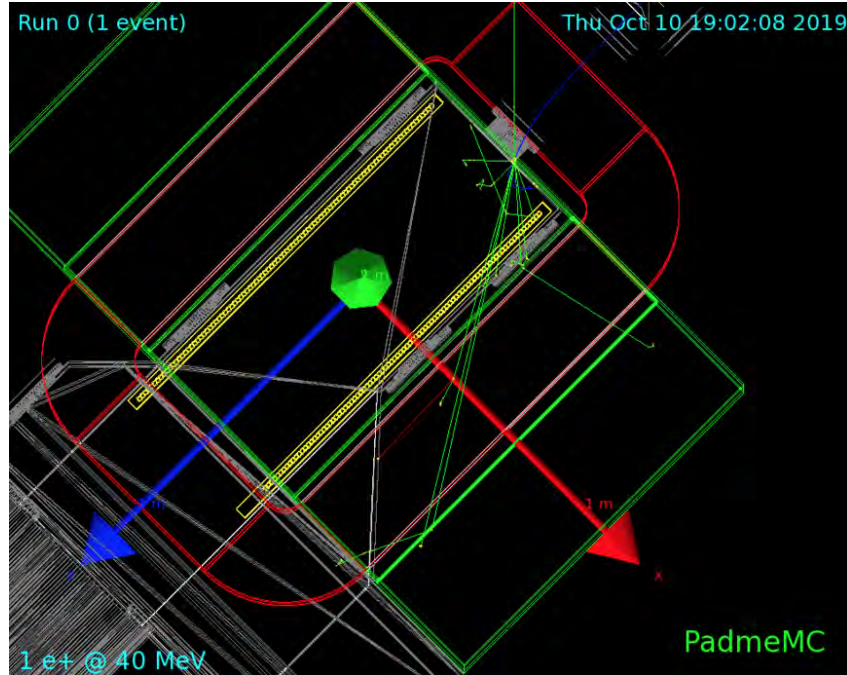


Figure 4.13. GEANT4 simulation of the Single Particle data generated with the vacuum chamber and without the target. The blue line represents a single positron entering the experiment while the green ones represent photons produced as a consequence of the interaction of the positron with the vacuum chamber.

For energies greater than $\sim 50\text{MeV}$ the analytic function provide again a good description of the reconstructed particle momentum. A final check on the analytic function validity was made with simulated data obtained with both the vacuum chamber and the active diamond target again scanning the energy range in single particle mode. In this case the monochromatic energy of the particle together with their direction on the beam axis can be modified by the interaction with the target before entering the spectrometer region. Using the standard reconstruction of the particle momentum the relative resolution shown in Fig. 4.14 was obtained.

Comparing the relative resolution obtained by the theoretical model with that obtained from this new simulation (see Fig. 4.15), it can be observed that the presence of the vacuum chamber together with the active diamond target induces a different trend to the resolution with respect to the analytical predictions.

The high energy behaviour follows the one of the analytic function showing just a little offset in the absolute value of the resolution. This is most probably due to multiple scattering induced from the interaction of the positrons with the $100\ \mu\text{m}$ of carbon in the target. As a consequence of the interaction, the particle enters the

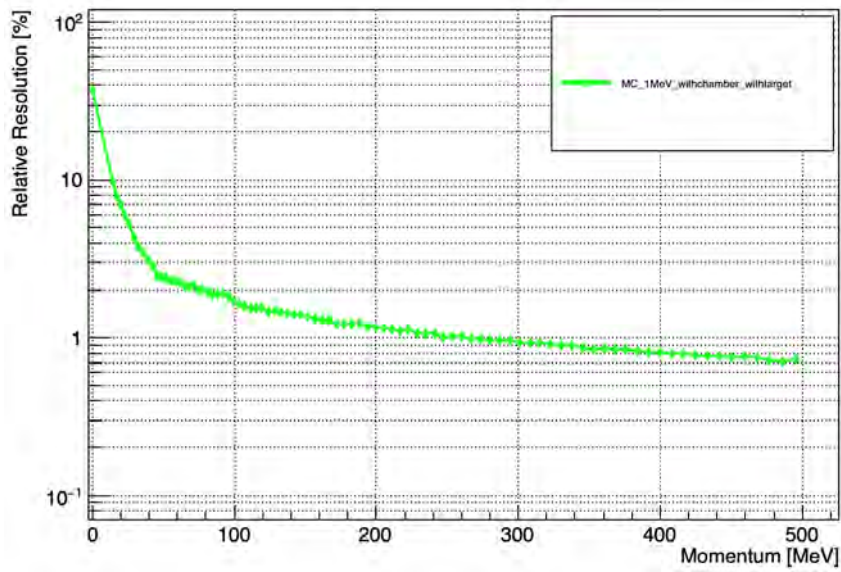


Figure 4.14. Relative resolution as a function of the momentum with both the vacuum chamber and the target on.

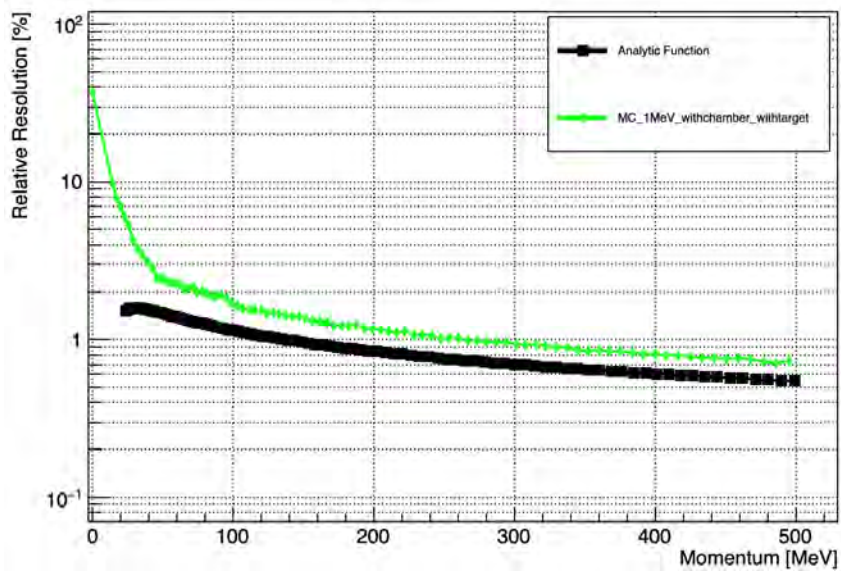


Figure 4.15. Comparison between the relative resolution of the theoretical method and that obtained from the Single Particle data with vacuum chamber and target.

spectrometer region with a trajectory which is not necessary parallel to the beam axis. For this reason his impact point might differ a bit with respect to the one predicted using the beam direction assumption.

To better understand the low energy region, < 50 MeV, a comparison of all the single particle modes samples is presented in Fig.4.16.

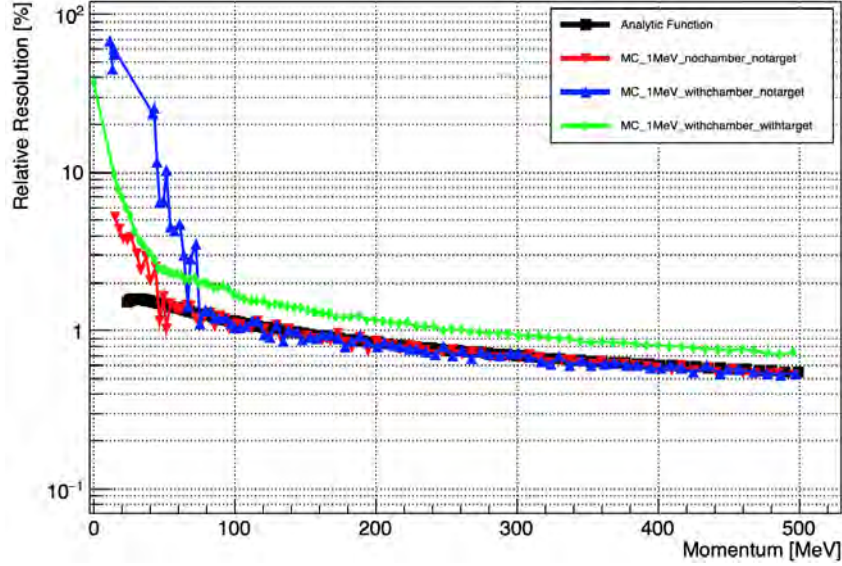


Figure 4.16. Comparison between the relative resolution of the theoretical method and the relative resolution obtained from all the datasets generated in Single Particle mode.

When particles are generated with a precise direction and energy, and no interaction is allowed before entering the spectrometer due to the absence of the target, the chamber induces a minimum acceptance of ~ 50 MeV and no particle below that energy can be properly measured (blue curve). In case the target is present, some of these particles are able to enter the chamber inner hole just because by chance their original trajectory has been modified accordingly by the target interaction. Nevertheless the measured momentum is wrong because their trajectory doesn't follow the predicted one (green curve).

In conclusion, the data generated in the Single Particle mode using the GEANT4 simulation of the experiment indicate that the resolution of the PADME spectrometer is very good, below 2%, for energies greater than ~ 50 MeV, while for lower energies it tends to be no longer satisfactory due to the presence of the PADME vacuum chamber structure.

Since the aim of the PVeto system in the PADME experiment was to reject positrons producing a radiated gamma in the interval, 50-400 MeV, this kind of performance has to be considered very satisfactory for the dark photon searches. In fact in the interesting case, energy of the positrons in the interval $E_{beam} - E_{\gamma}^{max} = 150$ MeV $< E_{e^+} < E_{beam} - E_{\gamma}^{min} = 500$ MeV, the resolution is well below 2%.

Finally we need to consider that in the search for six leptons final state the efficiency in 4.16 can be critical since the average track energy in 6 leptons final state is ~ 90 MeV. Possible optimisation of this parameter will be discussed in chapter 5.

4.2.3 Full Bunch Structure

Due to the 50Hz bunch structure of the DAΦNE beam test facility, to achieve the desired luminosity of 1 million positrons per second, the PADME experiments run routinely with 25000 particle per single bunch. This cause an extremely high instantaneous luminosity and consequently a very high rate in the spectrometer, which might affect its ideal resolution in single particle mode. For this reasons a data set in Full Bunch Structure mode has been generated, including the whole experimental setup and beam characteristics. All effects like particle original direction, interaction with the diamond target (multiple scattering and energy loss by bremsstrahlung), and pile up are now present.

Moreover in this case only the beam original positron energy 550 MeV is generated with the BTF energy resolution of 1%, and all the lower energies are obtained only when the positron emits a strong enough radiative photon to loose the necessary energy. For example a positron can enter in the energy bin 250 MeV only if it emits a 300 MeV radiative photon.

As a consequence the assumption of having a positron flying in the beam direction after the target is strongly violated in this case. The relative resolution of the PVeto system obtained from the Full Bunch Structure mode data is that shown in Fig. 4.17

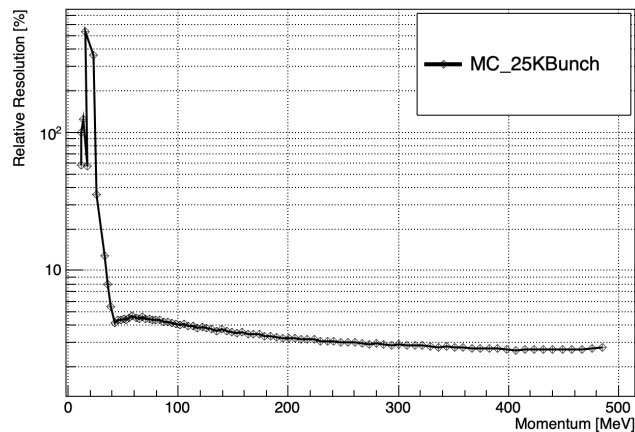


Figure 4.17. Relative resolution as a function of the momentum with all the experimental apparatus in Full Bunch Structure mode.

Comparing this resolution with the analytic function, shown in Fig. 4.18, one immediately notices the strong disagreement between the two resolutions. This difference is due to the nature of the bunch: the high statistics of the Full Bunch Structure together with the bremsstrahlung reduction of the positron energy significantly reduces the resolution of the spectrometer. This is not an unexpected result as the analytic function does not take into account the interaction with the target and assumes that particles are entering the spectrometer region in the beam direction.

To conclude this chapter, a graph is shown in Fig. 4.19 with all the relative resolutions, treated in this thesis work, compared with each other.

Even if, in the 25000 positrons per bunch mode the ideal resolution is worsened by factor ~ 2 , it is still lower than 5% in the whole measurable region.

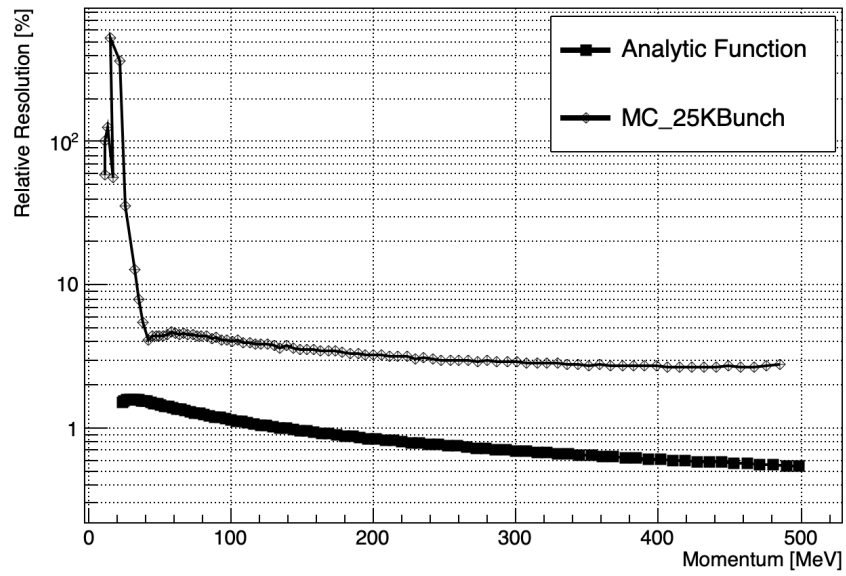


Figure 4.18. Comparison between the relative resolution of the theoretical method and the relative resolution obtained from the Full Bunch Structure mode dataset.

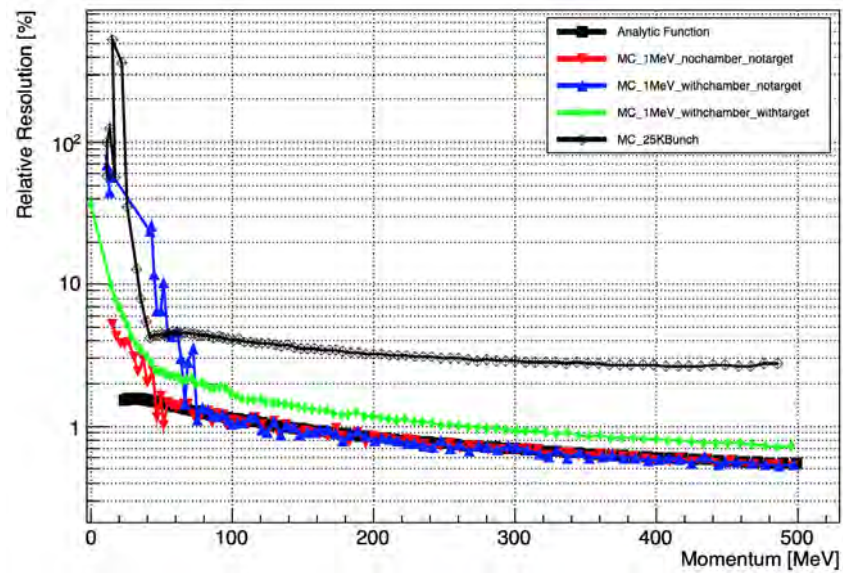


Figure 4.19. Comparison between all relative resolution treated in this chapter.

Chapter 5

Dark Higgs-like event selection

Since the analytic function, derived from the theoretical treatment in chapter 4, is suitable for the momentum reconstruction of charged particles in PADME, it can be used in the identification of positrons and electrons, which could have been generated in a DH-like background event. As described in chapter 2, in the Higgs'-strahlung process a DH h' is generated in the reaction $e^+e^- \rightarrow A'h'$. If the Dark Higgs mass is greater than twice the A' mass it will decay into two DP, generating an intermediate state of $3A'$. In the scenario in which the A' is lighter with respect to the dark matter, each A' decays into a pair e^+e^- .

$$e^+e^- \rightarrow h'A' \rightarrow A'A'A' \rightarrow 3(e^+e^-) \quad (5.1)$$

The final state of the Higgs'-strahlung process will be composed by six charged leptons, respectively three positrons and three electrons.

In the following chapter the identification procedure for DH-like multitrack events, applied on the data generated by the GEANT4 simulation, will be illustrated together with the background estimates.

5.1 QED background processes

Possible background final states at the PADME experiment can derive from QED e^+e^- scattering processes. One of the most common background source is the Bhabha scattering ($e^+e^- \rightarrow e^+e^-$). In the Standard Model the process can be mediated by both γ or Z and has two leading contribution represented by the scattering and annihilation Feynman diagrams. The relevant diagrams are shown in Figs. 5.1 and 5.2.

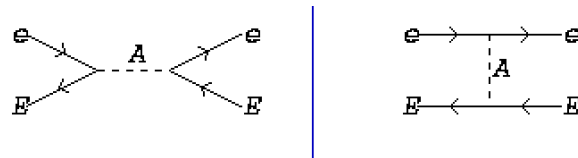


Figure 5.1. S-channel and t-channel Feynman diagrams for the Bhabha scattering process at low energy. E and e represent respectively positron and electron while A is the photon mediator.

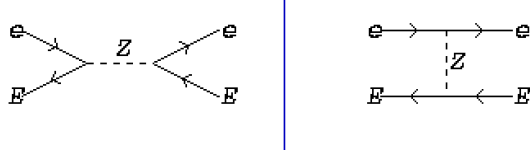


Figure 5.2. S-channel and t-channel Feynman diagrams for the Bhabha scattering process at high energy. E and e represent respectively positron and electron while Z is the mediator boson.

Since the Z boson is only dominant when the center-of-mass energy is near to its mass, ($\sqrt{s} \sim M_Z = 90\text{GeV}$), and the PADME experiment operates at a center-of-mass energy of $<25\text{MeV}$, the contribution due to Feynman diagrams with the Z -boson as mediator are negligible.

Due to the fact that the PADME experiment is operated with 25000 particle per single bunch of 200 ns, there is a non negligible probability that 3 simultaneous $e^+e^- \rightarrow e^+e^-$ interactions, produced by three different positrons, may occur in the same bunch generating a 6 leptons final state mimic the DH decay.

In order to produce 6 leptons out a single e^+e^- pair, 3 photon mediators must be produced at the same time. This type of process, $e^+e^- \rightarrow 3(e^+e^-)$, exists in SM and can be produced by 48 different Feynman diagrams. Some of these are shown as an example in Fig. 5.3.

However, since this process is always characterised by Feynman diagrams containing six electromagnetic vertices, it is expected that they will be strongly suppressed (order α^6). Consequently, this source of background can be considered negligible, at low energies, in the search for DH-like events decaying into three positrons and three electrons, for large values of the coupling constant. Moreover if the mass of the e^+e^- pairs can be measured, the constraint on the mass of the pairs being equal, will completely kill any contribution from SM. At least for the PADME case, this background can be excluded from the estimates. For this reason in the following sections, we will concentrate our attention on the BhaBha pile up background, and will use the GEANT4 MC to simulate such events.

5.2 Event reconstruction

The first step for searching for DH background events is the reconstruction of charged particles in the generated GEANT4 events. The MonteCarlo simulation does not directly return to the user the detected particles but a digital information called $\text{Hit}_{\text{GEANT4}}$, which indicates the energy deposit of a particle while crossing an area of a detector. The hit contains the following informations: charge, arrival time, spatial position and energy deposited on that point.

This type of digital information is very different from the one obtained by the experiment. To reconstruct a charged particle that has been detected, it is necessary to aggregate different information from multiple $\text{Hit}_{\text{GEANT4}}$. During the reconstruction of charged particles, several factors must be considered: the maximum number of scintillating fingers that a charged particle can cross, and the time it takes to cross one of them. In the next subsections the analysis techniques that have

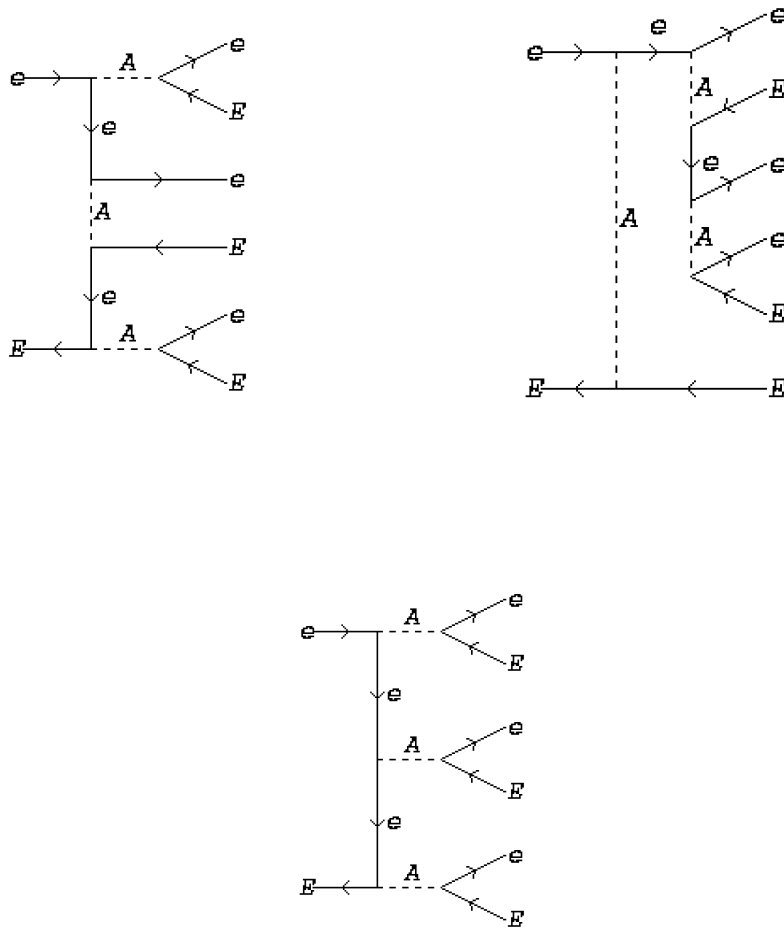


Figure 5.3. Examples of Feynman diagrams for the $e^+e^- \rightarrow 3(e^+e^-)$ process.

been used for the reconstruction of charged particles in GEANT4 events starting from $\text{Hits}_{\text{GEANT4}}$ is explained.

5.2.1 Photon collection simulation

Since, as explained in chapter 4, the essential detectors for this thesis research are the PVeto and EVeto systems, only the $\text{Hits}_{\text{GEANT4}}$ relating to these two detectors have been extracted from the generated data.

Information from the $\text{Hits}_{\text{GEANT4}}$ relating to the PVeto and EVeto systems, extracted from the generated data are: the detection channel, the arrival time, the three spatial coordinates of impact and the released energy by the charged particles. The first analysis performed on these data consists in parameterising the transport of the light from the energy release position, to the readout SiPM. To do this, for each $\text{Hit}_{\text{GEANT4}}$, the arrival times and the distances traveled from the local position of a $\text{Hit}_{\text{GEANT4}}$ to a SiPM are calculated, according to the equations reported in Eq. 5.2

$$\begin{cases} d[\text{cm}] = \sqrt{x^2 + (y - 8.9)^2 + z^2} \\ t[\text{ns}] = t_{\text{GEANT4}} + \frac{d}{v_\gamma} = t_{\text{GEANT4}} + \frac{dn}{c} \end{cases} \quad (5.2)$$

d represents the distance that the optical photon needs to travel from the position of a $\text{Hit}_{\text{GEANT4}}$ to the SiPM position, which is 8.9 cm distant from the center of the scintillating finger, center of the local coordinate system. t represents the time that the photon needs to reach a SiPM from a scintillating finger and it is expressed as the sum of the $\text{Hit}_{\text{GEANT4}}$ arrival time and the time the photon takes to cross d with a velocity v_γ equal to the speed of light $c = 30\text{cm/ns}$ divided by n index of refraction of the medium.

Another extracted quantity that is fundamental for this analysis is the average number of optical photons generated by the interaction of a charged particle with a scintillating finger. Knowing that in a scintillating fingers of PADME's Veto systems a charged particle generates about 50 photons per MeV, from the calculated average value of the deposited GEANT4 energy

$$\text{mean}_\gamma = 50 \cdot \text{energy}_{\text{GEANT4}} \quad (5.3)$$

through a Poissonian distribution it is possible to obtain, for each $\text{Hit}_{\text{GEANT4}}$, an average number of photons produced.

This information is necessary for the next step in the analysis of simulated data. To simulate signal produced by the SiPM the number of photon per hit have been represented in histograms having 1000 bins with a width equal to the readout digitiser digitisation interval (i.e. 0.4 ns). Each group of photon is positioned in the bin corresponding to its time. The peak in this distribution having more than 10 photons are considered has detected by the SiPM, and a time equal to the bin position is associated to the reconstructed hit. At the end of this process every finger has a list of reconstructed hits, one per each particle crossing it, containing time and energy deposit in units of photons collected.

5.2.2 Particle reconstruction

After digitising the signal of each finger it is possible to reconstruct the charged particles that have been detected.

A charged particle that enters the vacuum chamber is bended by the magnetic field and, depending on its energy, can cross multiple scintillating bars and therefore generating several digitised hits in consecutive bars. From simulation we know, that highly energetic charged particles, with momentum around 500 MeV, are able to cross a maximum of four scintillating bars. Furthermore it is known that a charged particle takes about 0.05 ns to cross a scintillating finger.

These two parameters were used to obtain the list of the charged particles detected from the experiment by clustering digitised hits. With the term clustering we indicate the grouping of several digitised hit together, which satisfy the spatial and temporal conditions listed above. The following requirements must be met by digitised Hits to form a particle:

- hits must have the same electrical charge;
- hits must be in close fingers (no more than 4);
- the difference in between their times must be less than 0.05 ns

Once these conditions are satisfied, a charged particle has been found, which, depending on the charge sign, will be a positron or an electron.

However, at this point the reconstruction of the charged particles within the events simulated by GEANT4 is not yet complete. In order to identify DH background events, it is necessary to obtain the momentum of these newly identified charged particles. This quantity can be calculated using the analytic function, treated in chapter 4. As observed in the previous chapter, from the analytic function it is possible to obtain, starting from the position of impact on the Veto system, the momentum of the charged particle. To adapt simulation to the experimental data, the center of each bar has been assigned as the position to be inserted in the analytic function to obtain the momentum of the particle. Using this simple algorithm only 90(96) values of the momentum are allowed for the PVeto (EVeto). Better results can be obtained if some convolution of the different bar will be in the future used. The raw particle time assigned is to be the time of the hit of the selected bar.

5.2.3 Particle time correction

The times associated with the reconstructed particles are the detection times at the SiPM. This quantity suffers by different problems: the distance travelled by each particle depends on its momentum and therefore particles generate simultaneously in the target will reach the veto detector at different times. To determine if DH-like events were generated within the experiment, it is necessary to know if the selected particles were generated simultaneously at the active diamond target. To reconstruct the generation time at the target, a correction on the raw particle times is necessary. In order to estimate such correction, 500 events were generated simultaneously in the MC for each energy from 10-550 MeV in step of 1MeV. From this data set, the

distribution of the arrival times of the particles on the PVeto system is produced, as shown in Fig. 5.4

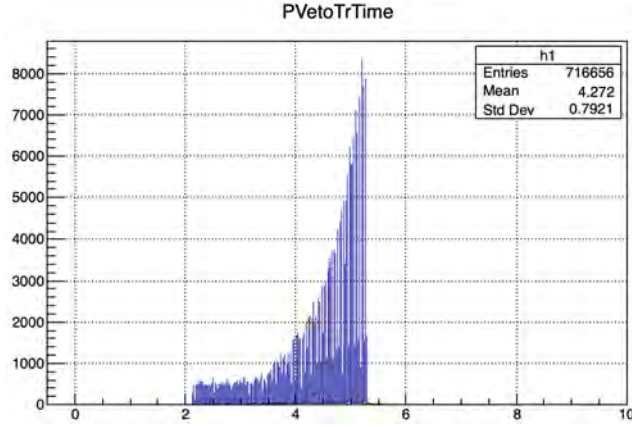


Figure 5.4. Distribution of the positrons arrival time at the PVeto system.

The distribution shows a minimum delay of ~ 2 ns corresponding to ~ 0.6 m and maximum delay of ~ 5 ns corresponding to ~ 1.5 m. The difference of 3 ns is much bigger than the P veto time resolution so that a correction is certainly needed. The average values were extracted from the distribution of the arrival times in each of the ninety fingers of the PVeto system. These values were used as time corrections as a function of the number of scintillating bar. These values are shown in Fig. 5.5

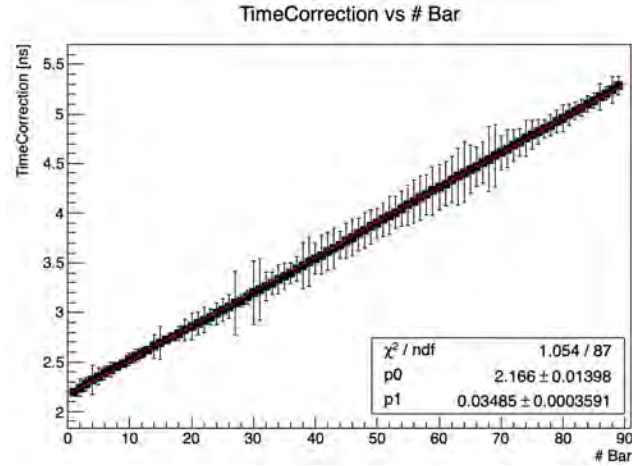


Figure 5.5. Average time delay vs finger distribution.

To check that the correction is actually working properly, the linear parameterisation of the distribution in Fig.5.5 was used to reconstruct the time at the target for tracks in the simulation. The formula used for the correction is the following:

$$y = p_0 + p_1 \cdot x \quad (5.4)$$

where p_0 and p_1 are the fit values, x represents the index of the scintillating bar, and y is the time correction to be applied. This correction was subtracted from the

actual generation times extracted from the simulated data for each bar. The results of this check are shown in Fig. 5.6

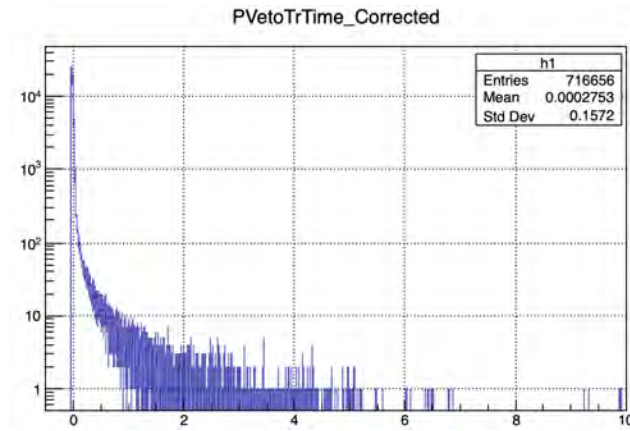


Figure 5.6. Checking on the Time Correction values.

The distribution shows a very good average, extremely close to 0, an RMS of just 150ps which is negligible with respect to the P veto intrinsic time resolution of ~ 500 ps. For this reason the correction can be considered satisfactory and can be applied to the raw SiPM times of the reconstructed particles to obtain the production times of the particle at the target.

At this point all the particles of the simulated events are reconstructed with all the parameters necessary for the selection of the DH background events.

5.3 Event selection and background estimates

After finding the charged particles and assigning them a value of momentum and production time at the target, it is possible to reconstruct background events to DH decaying in six charged leptons.

For this thesis work 500×10^3 bunch were simulated with Monte Carlo in Full Bunch Structure mode with 25×10^3 of particles per bunch for a total of 1.25×10^{10} positrons on target, corresponding to ~ 2.5 per mille of the PADME run1 data set. Before selecting the events, the first information that can be obtained from the generated data is the distributions of reconstructed momentum for both electrons and positrons. These distributions are shown in histograms of Fig. 5.7.

From the distribution of the positron momentum, it can be seen that most of the positrons are highly energetic. Since to determine a DH-like background event, the sum of the momentum of the six charged particles cannot exceed the energy of the beam, 550 MeV, it can be immediately noticed that most of the events generated cannot be considered in the reconstruction of DH events.

Time distribution of all charged particles is shown in Fig. 5.8.

As expected after digitizing the signal and applying time corrections, the bunch structure is well reproduced, with a width of around 250 ns as required at generation

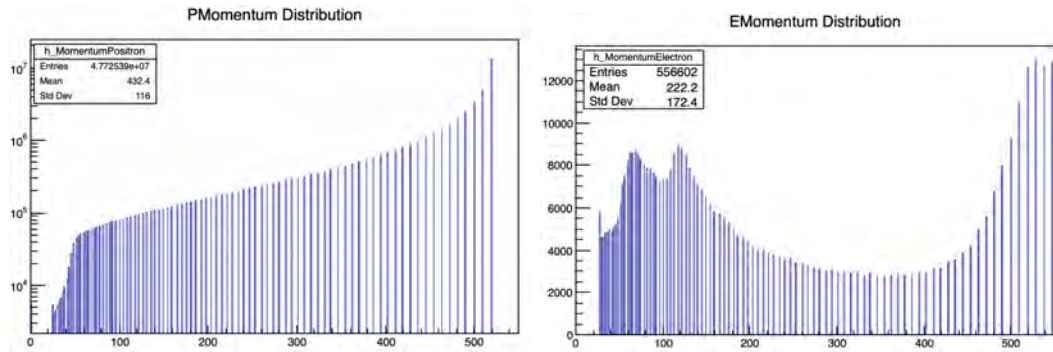


Figure 5.7. Positron and electron momenta distribution for 500×10^3 generated bunch reconstructed by using the analytical formula.

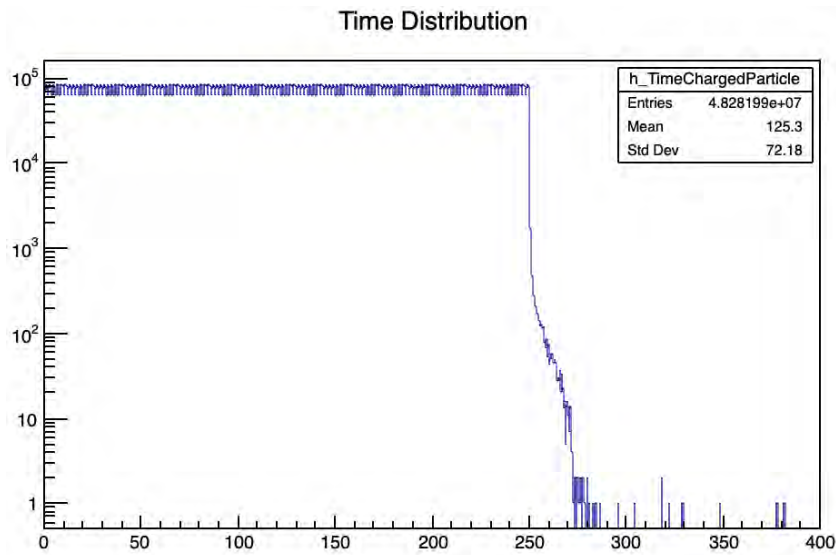


Figure 5.8. Time distribution for both positrons and electrons of the 500×10^3 generated events

level.

Tails of events outside the generation window, are most probably due to slow neutrons produced in the interaction of positrons with the target. The distributions of the number of positron and electron event by event are shown in Fig. 5.9.

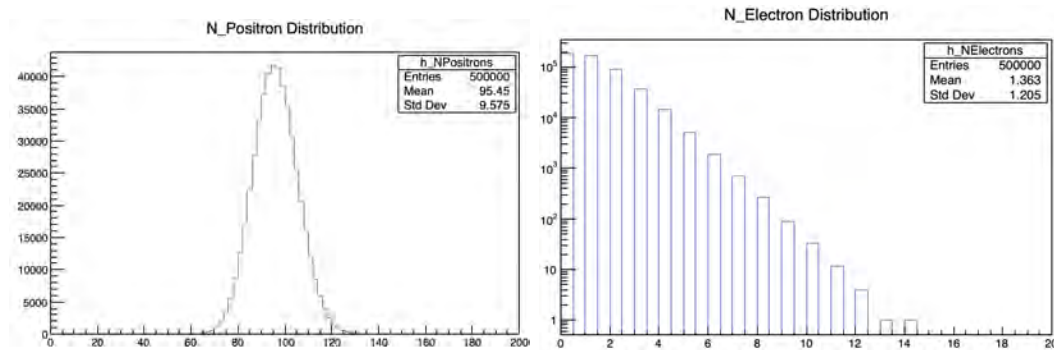


Figure 5.9. Number of positrons and electrons found for 500×10^3 generated events.

From these distributions we note the higher multiplicity of positrons with respect to the electrons that can be found in the event generated. This is of course due to the fact that we have a high intensity positron beam. Just looking at these graphs you can glimpse most of the events will be discarded in the selection of DH-like events, due to the absence of three electrons.

The first step in the search for DH events is to find triplets of positrons and electrons in time within each other, i.e. generated simultaneously at the target. The time difference required is less than 1 ns. In Fig. 5.10. The distributions of the number of in time positron and electron triplets are shown.

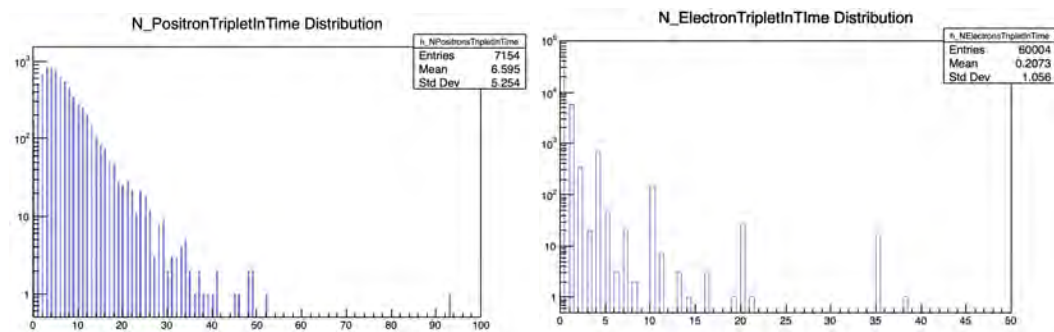


Figure 5.10. Triplets of positrons and electrons that respect the time condition.

As expected there are many positron triplets and very few electron triplets. To further select the DH-like events, an energy cut is applied to these triplets. If the energy of a triplet is higher than the beam energy is most probably produced by pile-up and needs to be rejected. The distributions of the number of positron and electron triplets that satisfy the time and momentum conditions are shown in Fig. 5.11.

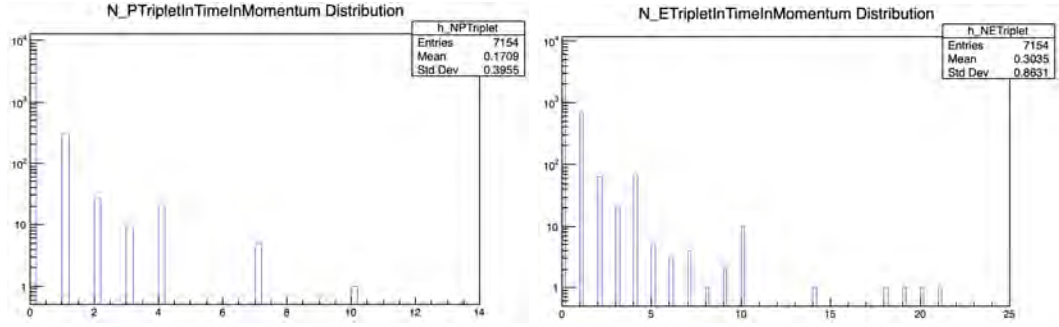


Figure 5.11. Triplets of positrons and electrons that respect the time and the energy conditions.

After finding these new triplets, the last selection for the search for DH events condition is applied. We assign as the production time of the triplets at the target the average time of the triplet, and as energy the sum of the energies of the particles of the triplet. Imposing the total momentum, sum of the six particles momenta, being lower than the beam momentum, and time difference in between the two triplets to be lower than 1 ns DH-like events are selected. As shown in Fig. 5.12 left, having a triplet of positrons with energy below 300 MeV, which is what you expect for events with 6 tracks and total energy of 550 MeV, is a very rare condition.

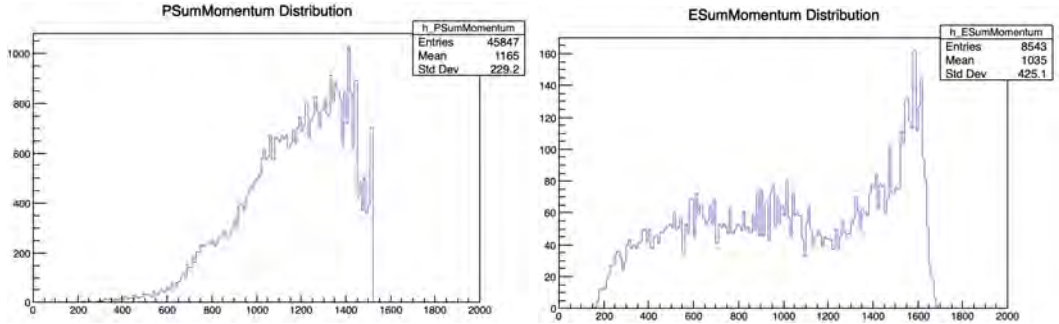


Figure 5.12. Distribution of total momentum for triplets of positrons and electrons that satisfy the time and the energy conditions.

In fact BhaBha scattering of positron on fixed target is expected to produce mostly high energy positron due to the elastic nature of the scattering. Having this in coincidence with the presence of a triplet of electrons, which also appears to be a very rare event, it is very unlikely to happen.

No pair of triplet out of the 1.25×10^{10} simulated particles has been found able to satisfy all the required conditions. In Fig. 5.13 a total momentum distribution is shown, before applying the beam energy condition.

As can be seen, no pairs of triplets can be found with total energy below 550 MeV. This margin indicates that even with an increase in the event statistics, it will unlikely to find DH-like events that satisfy the applied energy condition.

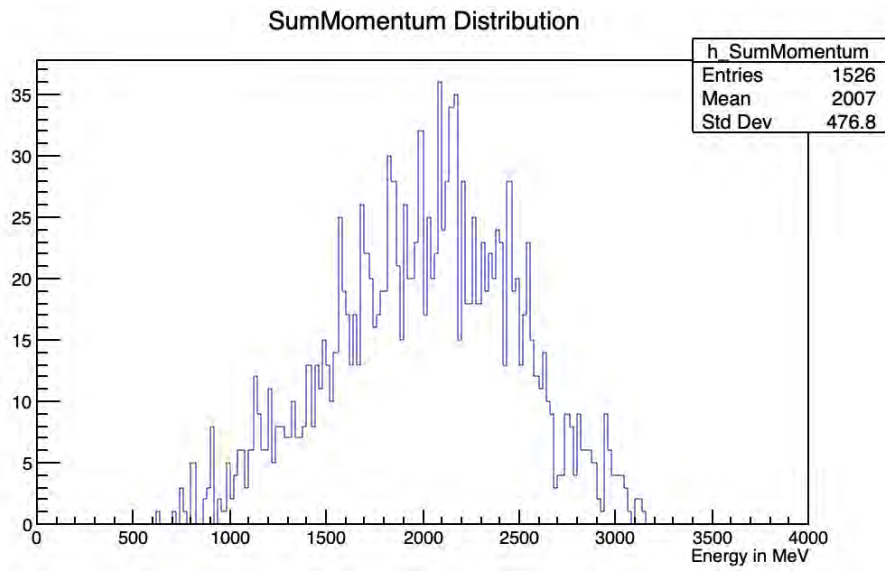


Figure 5.13. Distribution of total momentum for six charged leptons that satisfy only the time condition.

Chapter 6

Conclusions and future perspectives

The goal of this thesis is the search for Dark Higgs-like background events having three positrons and three electrons in the final state at the PADME experiment.

To reach this goal a theoretical model was created to reconstruct charged particles momentum using informations coming from the Veto systems of the experimental apparatus. This model has been tested on Monte Carlo samples, generated in different conditions, using the GEANT4 simulation of the PADME experiment. From these checks, the validity of the theoretical model was obtained, which was subsequently adopted to reconstruct the momentum of the positrons and electrons for the selection of Dark Higgs events.

A sample of 500000 bunch, each containing 25000 positrons, for a total of 1.25×10^{10} simulated particles were generated to search for these events. From this MC sample, events with triplets of positrons and electrons were selected. In order for three positrons and three electrons to be originated from a Dark Higgs event they must have a total energy equal to the energy of the positron beam, and very close to each other generation times. After identifying triplets of positrons and electrons according to the energy and time conditions just mentioned, six lepton events were searched. From this analysis no Dark Higgs background events were found in the sample considered.

Future perspectives and useful results for the PADME experiment can be derived from this thesis work. The reconstruction of the charged particles momentum, the first topic of this work, indicates a high efficiency of the PADME spectrometer for energies higher than 50 MeV. These values indicate that the PADME experiment as it is now has a low efficiency in reconstructing DH-like events. For this type of research it is necessary to apply some changes. To increase the detection efficiency of low energy particles, the active diamond target could be moved closer to the vacuum chamber entrance, or the intensity of the dipolar magnetic field could be lowered to reduce low energy particle bending. These changes would prevent charged particles from colliding with the vacuum chamber and increase the detection efficiency of the first scintillating fingers of Veto systems.

From the estimate of the background events present in the PADME experiment, some theoretical assumptions have been verified. Among these, it has been verified

that the SM $e^+e^- \rightarrow 6(\textit{leptons})$ interaction is highly suppressed at least in the region of large coupling constant that PADME is able to investigate. Concerning the probability that three Bhabha events, $e^+e^- \rightarrow e^+e^-$ occur simultaneously, it has been found to be very small.

In absence of a solid MonteCarlo generator for the Dark Higgs events it has been impossible to have a reliable evaluation of the signal acceptance. From phase space only simulations, this appears to be under the present condition $\sim 2\%$. If the zero background hypothesis will be confirmed, by higher statistic MC simulations and data analysis, incomplete final state like 5 leptons + missing energy will be explored to increase the experiment acceptance.

Bibliography

- [1] B. Ryden, Introduction to cosmology. Addison-Wesley (2003).
- [2] Planck 2018 results. VI. Cosmological parameters - Planck Collaboration (Aghanim, N. et al.) arXiv:1807.06209 [astro-ph.CO]
- [3] F. Zwicky, Republication of: The redshift of extragalactic nebulae. *Gen. Relat. Gravit.* 41, 207 (2009).
- [4] Detection of the Missing Baryons toward the Sightline of H1821+643 - Kovcs, Orsolya E. et al. *Astrophys. J.* 872 (2019) no.1, 83 arXiv:1812.04625 [astro-ph.CO]
- [5] V. C. Rubin, and W. K. Ford, Jr., Rotation of the Andromeda Nebula from a Spectroscopic Survey of Emission Regions. *Astrophys. J.* 159, 379 (1970).
- [6] K. G. Begeman, A. H. Broeils, and R. H. Sanders, Extended rotation curves of spiral galaxies. Dark haloes and modified dynamics. *MNRAS* 249, 523 (1991).
- [7] G. G. Raffelt, Dark matter: Motivation, candidates and searches. arXiv:hep-ph/9712538 (1997).
- [8] I. Smail et al., A comparison of direct and indirect mass estimates for distant clusters of galaxies. *Astrophys. J.* 479, 70 (1997).
- [9] <http://hubblesite.org/>
- [10] A High Stellar Velocity Dispersion and ~ 100 Globular Clusters for the Ultra-diffuse Galaxy Dragonfly 44 - van Dokkum, Pieter et al. *Astrophys. J.* 828 (2016) no.1, L6 arXiv:1606.06291 [astro-ph.GA]
- [11] M. C. Weisskopf et al., An Overview of the Performance and Scientific Results from the Chandra X-Ray Observatory. *PASP* 114, 1 (2002).
- [12] M. Johns, The Giant Magellan Telescope (GMT). *Proc. SPIE* 6267, 762 (2006).
- [13] G. Nurre, Hubble Space Telescope. Upper and Middle Atmospheric Density Modeling Requirements for Spacecraft Design and Operations, 73 (1987).
- [14] <http://chandra.harvard.edu/>

-
- [15] E. Komatsu et al. [WMAP Collaboration], *Astrophys. J. Suppl.* 180, 330 (2009) doi:10.1088/0067-0049/180/2/330 [arXiv:0803.0547 [astro-ph]]; E. Komatsu et al. [WMAP Collaboration], *Astrophys. J. Suppl.* 192, 18 (2011) [arXiv:1001.4538]; C. Bennett et al., *Astrophys. J. Suppl.* 148, 97 (2003).
- [16] Planck Collaboration, P. A. R. Ade et al., Planck 2015 results. XIII. Cosmological parameters, arXiv:1502.01589, *Astron. Astrophys.* 594, A13 (2016).
- [17] S. Perlmutter et al., *Astrophys. J.* 517, 565 (1999).
- [18] A. G. Riess et al., *Astrophys. J.* 118, 2675 (1999).
- [19] A. G. Riess et al., *Astrophys. J.* 607, 665 (2004).
- [20] K. Freese et al., *Nucl. Phys. B* 287, 797 (1987).
- [21] K. Freese and M. Lewis, *Phys. Lett. B* 540, 1 (2002).
- [22] C. Deffayet et al., *Phys. Rev. D* 65, 044023 (2002).
- [23] B. Paczynski, Gravitational microlensing by the galactic halo. *Astrophys. J.* 304, 1 (1986).
- [24] K. Griest, Galactic microlensing as a method of detecting massive compact halo objects. *Astrophys. J.* 366, 412 (1991).
- [25] R. Nemiroff, Probing galactic halo dark matter with microlensing. *A&A* 247, 73 (1991).
- [26] A. De Rjula, P. Jetzer, and E. Mazzo, On the nature of the dark halo of our galaxy. *A&A* 254, 99 (1992).
- [27] C. Afonso et al., Limits on Galactic dark matter with 5 years of EROS SMC data. *A&A* 400, 951 (2003).
- [28] M. Milgrom, A modification of the Newtonian dynamics as a possible alternative to the hidden mass hypothesis. *Astrophys. J.* 270, 365 (1983).
- [29] R. Peccei, and H. Quinn, Constraints imposed by CP conservation in the presence of pseudoparticles. *Phys. Rev. D* 16, 1791 (1977).
- [30] Baker, C. A et al., Improved Experimental Limit on the Electric Dipole Moment of the Neutron. *Phys. Rev. Lett.* 97, 131801 (2006).
- [31] M. S. Turner, Windows on the axion. *Phys. Rept.* 197, 67 (1990).
- [32] M. Dine, and W. Fischler, The not-so-harmless axion. *Phys. Lett. B* 120, 137 (1983).
- [33] J. Preskill, M. B. Wise, and F. Wilczek, Cosmology of the invisible axion. *Phys. Lett. B* 120, 127 (1983).
- [34] L. Abbott, and P. Sikivie, A cosmological bound on the invisible axion. *Phys. Lett. B* 120, 133 (1983).

- [35] J. E. Kim, and G. Carosi, Axions and the strong CP problem. *Rev. Mod. Phys.* 82, 557 (2010).
- [36] C. Hagmann, A Search for Cosmic Axion. Ph.D. thesis, University of Florida, Gainesville, FL 32611-8440 (1990).
- [37] E. Arik et al., Probing eV-scale axions with CAST. *JCAP* 02(2009)008.
- [38] Asztalos et al., High resolution search for dark-matter axions. *Phys. Rev. D* 74, 012006 (2006).
- [39] F. Della Valle et al., The PVLAS experiment for measuring the magnetic birefringence of vacuum. *Nuovo Cimento Soc. Ital. Fis. C* 36, 41 (2013).
- [40] E. W. Kolb, and M. S. Turner, *The Early Universe*. Addison-Wesley, Redwood City, (1989).
- [41] S. P. Martin, *A Supersymmetry Primer*. arXiv:hep-ph/9709356v6 (2011).
- [42] N. Craig, *The State of Supersymmetry after Run I of the LHC*. Lectures at the training week of the GGI workshop Beyond the Standard Model after the first run of the LHC, arXiv:1309.0528v2 (2014).
- [43] CMS Collaboration (Chatrchyan S. et al.), *Phys. Lett. B*, 716 (2012) 30.
- [44] ATLAS Collaboration (Aad G. et al.), *Phys. Lett. B*, 716 (2012) 1.
- [45] Planck Collaboration (Ade P. A. R. et al.), *Astron. Astrophys.*, 571 (2014) A22.
- [46] PAMELA Collaboration (Adriani O. et al.), *Nature*, 458 (2009) 607.
- [47] Fermi LAT Collaboration (Ackermann M. et al.), *Phys. Rev. Lett.*, 108 (2012) 011103.
- [48] AMS Collaboration (Aguilar M. et al.), *Phys. Rev. Lett.*, 110 (2013) 141102.
- [49] AMS-02 Collaboration, *Talks at the AMS Days at CERN, 15-17 April 2015*.
- [50] Blum T., Denig A., Logashenko I., de Rafael E., Lee Roberts B., Teubner T. and Venanzoni G., arXiv:1311.2198 [hep-ph].
- [51] The g-2 Collaboration (Benett G. W. et al.), *Phys. Rev. D*, 73 (2006) 072003.
- [52] Particle Data Group (Olive K. A. et al.), *Chin. Phys. C*, 38 (2014) 090001.
- [53] Essig R., Jaros J. A., Wester W., Adrian P. H. and Andreas S. et al., arXiv:1311.0029 [hep-ph].
- [54] Cherry J. F., Friedland A. and Shoemaker I. M., arXiv:1411.1071 [hep-ph].
- [55] Pospelov M., *Phys. Rev. D*, 80 (2009) 095002.
- [56] Endo M., Hamaguchi K. and Mishima G., *Phys. Rev. D*, 86 (2012) 095029.

- [57] Okun L. B., Sov. Phys. JETP, 56 (1982) 502 (Zh. Eksp. Teor. Fiz., 83 (1982) 892).
- [58] Holdom B., Phys. Lett. B, 166 (1986) 196.
- [59] Galison P. and Manohar A., Phys. Lett. B, 136 (1984) 279.
- [60] Izaguirre E. and Yavin I., arXiv:1506.04760 [hep-ph].
- [61] An H., Pospelov M. and Pradler J., arXiv:1401.8287 [hep-ph].
- [62] Feng W. Z., Shiu G., Soler P. and Ye F., JHEP, 1405 (2014) 065.
- [63] Gorbunov D., Makarov A. and Timiryasov I., Phys. Rev. D, 91 (2015) 035027.
- [64] Bjorken J. D., Essig R., Schuster P. and Toro N., Phys. Rev. D, 80 (2009) 075018.
- [65] Beranek T. and Vanderhaeghen M., Phys. Rev. D, 89 (2014) 055006.
- [66] Fayet P., Phys. Rev. D, 75 (2007) 115017 (hep-ph/0702176 [HEP-PH]).
- [67] Raggi M. and Kozhuharov V., Adv. High Energy Phys., 2014 (2014) 959802.
- [68] Blmlein J. and Brunner J., Phys. Lett. B, 731 (2014) 320.
- [69] Echenard B., Essig R. and Zhong Y. M., JHEP, 1501 (2015) 113.
- [70] B. Batell, M. Pospelov, and A. Ritz, Phys. Rev. D 79, 115008 (2009).
- [71] R. N. Cahn, Rep. Prog. Phys. 52, 389 (1989); A. Grau, G. Panchieri, and R. J. N. Phillips, Phys. Lett. B 251, 293 (1990); B. A. Kniehl, Phys. Lett. B 244, 537 (1990).
- [72] BaBar Collaboration (Lees J. P. et al.), Phys. Rev. Lett., 108 (2012) 211801.
- [73] Belle Collaboration (Jaegle I.), Phys. Rev. Lett., 114 (2015) 211801.
- [74] KLOE-2 Collaboration (Anastasi A. et al.), Phys. Lett. B, 747 (2015) 365.
- [75] G. Vignola et al., Frascati Phys. Ser. 4:19-30 (1996).
- [76] KLOE Coll., Nucl. Inst. Meth. A 482, 363-385 (2002).
- [77] B. Buonomo et al., EPAC08, THPC143 (2008).
- [78] F. Sannibale and G. Vignola, DAΦNE Technical Note LC-2 (1991).
- [79] V. Kozhuharov, PADME: Searching for Dark Mediator at the Frascati BTF.
- [80] M.Raggi and V. Kozhuharov, Proposal to Search for a Dark Photon in Positron on Target Collisions at DAΦNE Linac, Vol.2014, Article ID 959802.
- [81] TASI 2011: CalcHEP and PYTHIA Tutorials - Kong, Kyoungchul arXiv:1208.0035 [hep-ph]

- [82] W. Heitler, *The Quantum Theory of Radiation*, Clarendon Press, Oxford, UK
- [83] M. Raggi and V. Kozhuharov, *AdHEP* 2014, 959802 (2014).
- [84] M. Raggi, V. Kozhuharov and P. Valente, *EPJ Web Conf.*96, 01025 (2015).
- [85] M. Raggi and V. Kozhuharov, *NEWPROJECTS ON DARK PHOTON SEARCH*, Frascati Physics Series Vol. 64 (2016).
- [86] <http://www.lnf.infn.it/acceleratori/padme/Talks.html>.
- [87] B. Adeva, et al., *Nucl.Instrum.Methods*A289(1990)35, 102.
- [88] (a)Y. Karyotakis, In *Proceedings of Calorimetry, Beijing,1994*, pp.27-35.; (b) *AnnecyLab.Part.Phys.*, LAPP-EXP-95-002(95/02,rec.Apr.)9pp.(510187).
- [89] Performance of the PADME Calorimeter prototype at the DAΦNE BTf - Raggi, M. et al. *Nucl.Instrum.Meth.* A862 (2017) 31-35 arXiv:1611.05649 [physics.ins-det].
- [90] Characterization and performance of PADME Cherenkov-based small-angle calorimeter - Frankenthal, A. et al. *Nucl.Instrum.Meth.* A919 (2019) 89-97 arXiv:1809.10840 [physics.ins-det].
- [91] Development and test of a DRS4-based DAQ system for the PADME experiment at the DAΦNE BTf - Leonardi, E. et al. *J.Phys.Conf.Ser.* 898 (2017) no.3, 032024.
- [92] Antcheva I et al. 2009 ROOT A C++ framework for petabyte data storage, statistical analysis and visualization *Comput. Phys. Commun.* 180 (12) 2499-2512.
- [93] Belyaev A, Christensen ND and Pukhov A 2012 CalcHEP 3.4 for collider physics within and beyond the Standard Model arXiv:1207.6082 [hep-ph].